CRANFIELD UNIVERSITY

MENGJIA DING

DESIGN AND SIMULATION OF COMPRESSIVE SNAPSHOT MULTISPECTRAL IMAGING SYSTEMS

SCHOOL OF DEFENCE AND SECURITY
PhD in Electro-Optics

PhD
Academic Year: 2014–2018

Supervisor: Dr Peter Yuen
December 2018

CRANFIELD UNIVERSITY

SCHOOL OF DEFENCE AND SECURITY
PhD in Electro-Optics

PhD

Academic Year: 2014–2018

MENGJIA DING

Design and Simulation of Compressive Snapshot Multispectral Imaging Systems

Supervisor: Dr Peter Yuen
December 2018

This thesis is submitted in partial fulfilment of the requirements for the degree of PhD.

"*Learning without reasoning leads to confusion, thinking without learning is wasted effort.*" — *Confucius, 2.15, The Analects of Confucius.*

学而不思则罔，思而不学则殆.—孔子, 论语·为政

Abstract

Compressive Snapshot Spectral Imaging combines compressive sensing and snapshot spectral imaging (SSI) for restoring the image of the scene in both spatial and spectral contexts by using only a fewer number of sampling measurements of the captured image under the sparsity assumption. SSI is often realised through a coded aperture mask together with a single dispersive element as the main spatial modulator to implement compressive sampling. As one of the representative frameworks in this field, *Coded Aperture Snapshot Spectral Imagers (CASSI)* has prototyped a low-cost, compact platform to achieve compressive snapshot spectral imaging in the recent decade. Active research in the field includes advanced de-compressive recovery algorithms and also the employment of more sophisticated optical hardware for the design of more robust SSI system. This research addresses more of the latter direction and it focuses on how the CASSI framework can be further developed for various applications such as magnetic resonance imaging for medical diagnosis, enhancement of radar imaging system, facial expression detection and recognition, digital signal processing with sparse structure in terms of image denoising, image super-resolution and image classification.

This thesis presents a summary of the research conducted over the past 4 years about the basic property of the CASSI system, which leads to the development of the spectral tuneable SSI design proposed during the course of the PhD study. This new design utilises a Dual-Prism assembly to embed the capability of wavelength-tuning without physically changing its optical elements. This Dual-Prism CASSI (DP-CASSI) adapts to dynamic environments far better than all the CASSI types of imagers published in the open domain which only function for a fixed set of wavelengths. This piece of work has been

accepted by journal papers for publication. Other contributions of this research has been the enhancement of the Single-Prism (SP-CASSI) architecture and to produce a snapshot system with less aberration and better image quality than that published in the open domain.

Moreover, the thesis also provides information about optical design of four different types of CASSI with slightly in-depth analysis about their optical system constructions, optical evaluations of system structure and their dispersive capabilities as the background of this research. Then a more detailed description of the proposed DP-CASSI with respected to its design and performance evaluation particularly its dispersion characteristics and the effects of system resolutions, are given. System verifications were conducted through ray-tracing simulation in three-dimension visualisation environments and the spectral characteristics of the targets are compared with that of the ground truth. The spectral tuning of the proposed DP-CASSI is achieved by adjusting the air gap displacement of dual-prism assembly. Typical spectral shifts of about 5 nm at 450 mm and 10 nm at 650 nm wavelength have been achieved in the present design when the air gap of the dual-prism is changed from 3.44 mm to 5.04 mm. The thesis summaries the optical designs, the performance and the pros and cons of the DP-CASSI system.

Keywords

Snapshot Spectral Imaging; Compressive Sensing; Optical System Design; OSLO; TracePro; CASSI.

Contents

List of Figures

List of Tables

List of Abbreviations

AST	Astigmatism
CASSI	Coded Aperture Snapshot Spectral Imager
CMA	Coma
DA-CASSI	Double-Amici Coded Aperture Snapshot Spectral Imager
DIS	Distortion
DP-CASSI	Dula-Prism Coded Aperture Snapshot Spectral Imager
FoV	Field of View
FPA	Focal Plane Array
MTF	Modulation Transfer Function
OSLO	Optics Software for Layout and Optimization
PTZ	Petzval Filed Curvature
ROI	Region of Interest
SA	Spherical Aberration
SP-CASSI	Single-Prism Coded Aperture Snapshot Spectral Imager
TwIST	Two-step Iterative Shrinkage/Thresholding
UV-CASSI	Ultraviolet-Visible Coded Aperture Snapshot Spectral Imager

Acknowledgements

I would like to thank my dearest parents who are a thousand miles away from me, thank their endless love in support of my entire education in terms of finance and care. Thanks to Dr. Peter WT Yuen for his great support with extra endurance and promptness in responding all my research problems during supervision. Thanks to Suzy Chen, Jez Bate, Jef O'Riley and their families for offering me a great time around Oxfordshire. Thanks to my landlord family Dianne & Chris Allen for almost 3 years of hospitality, providing me a warm and sweet home where I could get refuelled and carry on my expedition. Thanks to Leon Kocjancic for organising wonderful hiking trips. Thanks to Dr. Umair Soori, Senthurran Selvagumar, Murat Gunes, Usman Zahidi, Ayan Chartterjee and Ruben Moya-Torres in MH03 for sharing invaluable advice, help and encouragement. Thanks to Prof. Ron Matthews and his lovely student Michelle Charles, previous research visitors Dr. Ling Li and Yue Zhao for many interesting discussions regarding social science which helps me open my mind so much. Thanks to my friends who I met here, Junhui Xia, Wentao Chen, Dr. Changfeng Yuan, Dr. Krasin Georgiev, Weng Tuck Kok, Xin Ang, Siao Chien Chew, Wanning Liang, Pooja Kadam, Zilly Janjua and the Highworth Defence Academy Badminton Club for sharing happy moments. Thank you Prof. Mark A Richardson and Dr. David James for support and guidance for this project. Thanks to the Centre for Electronic Warfare, Information & Cyber and scene simulation project (DSTLX-1000103251), DSTL for generous support for this project. Thanks to all the Cranfield stuff for their professional support. Additional thanks to Emerge energy drink for sustaining and inspiring me in the last few days to finish this thesis.

Chapter 1

INTRODUCTION

Light is an intermedia that enables human beings like us to perceive our natural world. The reflected light from the background, like a petal of a tulip, a piece of fallen leaf or a field of meadows, radiates into our eyes and forms a vivid image with full details of their geometrical shapes and surface colours. Thanks to our magical *Brain* and *Eyes* which let us visualise how beautiful and fascinating our world is! However, biological evolution cannot allow us to see far away stars like Neptune nor could we visualise tiny blood cell! We have to rely on science and technology to fabricate advanced equipment to allow us to perceive objects around us. Nothing but light can be so natural to provide us a straight and clear way to understand those unknowns.

Spectral Imaging is an imaging technique that senses information of scenes through the capture of spatial-spectral information in three dimensional (3D) datacube which includes two dimensional (2D) structure of spatial content and one dimension of (1D) spectral information across the electromagnetic spectrum in the visible region, near-infrared, shortwave and far infrared specral range [5]. The realisation of sensing 3D data by a 2D focal plane array sensor can be implemented through (1) scan along one spatial directions of the 2D scene using a narrow slit embedded at the optical entrance window of the system. This single line of scene information is then dispersed to project the spatial-spectral information onto 2D array sensor [6, 7]; (2) the utilisation of a set of filters [8, 9]

to acquire the band images of the scene one by one; (3) single-pixel detection based on programmable computational ghost imaging [10–12] capable to acquire additioanl spatial dimension (eg depth) to function as a 4D imaging application [12]. After appropriate processing of this 3D or 4D information, e.g. image registration [13] and synchronisation [14–16], the spatial and spectral content of the scene can be fully revealed [17].

Spectral imaging technique can be roughly categorised into three groups as according to the number of spectral bands that the spectral imaging system can be resolved: *Panchromatic Imaging*, *Multispectral Imaging* and *Hyperspectral Imaging*. The panchromatic imaging system presents the scene in greyscale and it collects one broadband image with high spatial resolution [5]. This system was initially implemented for spaceborne applications such as the High-Resolution Geometric (HRG) instruments employed by the Systeme Pour l'Observation de lat Terre (SPOT) 5 satellite, which provides 5 m spatial resolution [18]; the Russian SPIN-2 KVR-1000 for urban/suburban landscape survey with 2 m panchromatic spatial resolution [19]; a wide spectral range of panchromatic imaging in the thermal region has also been utilised for surveillance and detection applications [5, 20, 21]. Due to the broad band nature in the panchromatic image the *Multispectral Imaging* and *Hyperspectral Imaging* have been developed [22–24] for various discrimination tasks. *Multispectral Imaging* (MSI) collects a few number of narrow spectral bands with around 10 nm to 20 nm bandwidth [25–28]. Historically, MSI was initially implemented in spaceborne and airborne platforms for astronomical and earth observation science purposes [25, 29–32], which was then extended for other usages e.g. biological, medical [33] and food safety applications [34]. The small number of spectral bands in the MSI systems enable them to be developed in small footprints [35, 36] such as the hand-held devices [28] which have been deployed for UAV surveillance [26, 37]. It also features high flexibility to cater for various applications through customized combinations of spectral bands [38, 39], e.g. *in vivo* measurement of electro-optical characteristics of biological molecules in the health care research [40] and near real-time video spectral imaging [41]. *Hyperspectral Imaging* (HSI) presents the scene with very detailed spectral

information which may contain as many as hundreds of contiguous narrow bands [41,42]. This feature dramatically improves the depth of measurement and it suits well for applications which require accurate assessment of the scene such as in the astronomy and Earth science research [43, 44], food science [45, 46], biomedical [47–49] and military and defence applications [50]. However, the main drawback in HSI is the very long data acquisition time. Recent research and commercial exploitations tend to reduce the hardware cost [51–53] through physical miniaturization [54–56]. One emerging approach is the development of snap-shot multispectral imaging (SSI) which acquires spatial and spectral data in a snap-shot without the need of scene scanning and this subject has been the main topic of the present research.

1.1 Motivation of the Thesis

There are three motivations for this research project:

1. Detailed optical design considerations for coded aperture snapshot imaging (CASSI) system:

   CASSI has been regarded as a foundation in the snapshot imaging (SSI) system, however, despite of its importance and popularity the design methodology, configuration of optical parameters and their impacts on the performance of the system, are not available in the open domain. This makes researchers in this field difficult to pursue further work in CASSI. As a consequence, the CASSI approach has not been widespread adopted for commercial exploitation. This thesis provides useful information about optical designs and parameter considerations for the various versions of the CASSI system.

2. Background information about the use of optical software:

   Imaging system design includes evaluation, optimisation and simulations steps and tools such as the Optical Software for Layout and Optimization (OSLO®) and ray

tracing software like TracePro® have been frequently employed by researchers in the field. This thesis gives an overview of how to use these tools for the design of snapshot spectral system and it may be regarded as a user manual as an initial starting point for new researchers in the field.

3. Spectral tuning in the SSI system:

   Almost all SSI systems reported to-date only cater for fixed sets of spectral wavelengths which limit their practical usefulness. The objective of the present research is to study and to develop a wavelength-tuneable SSI using low cost optical components, and to document what are the impacts of this design to the research community and to comment how it can be further enhanced for practical applications.

1.2 Snapshot Spectral Imager

Conventional spectral imaging systems obtain spatial-spectral information by scanning the scene through either spatial pushbroom [57, 58], spatial whiskbroom [59] or spectral rolling filtering techniques [8]. These methods have been widely adopted in aforementioned areas for target/scene classification and detection purposes. One great drawback in these scanning techniques is the very long data acquisition time. *Snapshot Spectral Imaging* (SSI) is the technique enables the acquisition of the scene in both spectral and spatial domains through one single-shot measurement. Under this scheme, the spectral and spatial data are partially overlapped [60] or so called 'multiplexed'. One way to de-multiplex the convolved spatial and spectral data is to slice the 2D input image into strips and it is then dispersed to form a 2D spectral-spatial array [61]. Another method is to utilize a mapping mirror with facets such that it redirects different parts of the scene for spectral dispersion [62]; or alternatively to add spectral channels with multiple beam splitters with spectral filters and corresponding detectors to acquire monochromatic spatial frames individually [63]. SSI not only improves poor light collection efficiency [64, 65] in comparison to the slit-based conventional scanning imaging systems [66], it also capable to

produce good quality spectral imagery with better SNR [67] than that of the band filtering technique [68–70]. Over the last few decades of technological developments in the field, SSI technology has become mature enough for commercial exploitation [71, 72] due to its faster image acquisition ability which makes it more suitable for dynamic environment applications. As an introduction a few varieties of SSI techniques have been outlined in the next section.

Computed Tomographic Imaging Spectrometer (CTIS) [1,73,74] is a technique which collects series of spatial spectral diffracted data of the 3D scene through Computer Generated Holographic disperser [75] or 2D diffraction gratings to form computed-tomography images [76]. The early design of CTIS, as shown in Fig. 1.1, typically contains a field stop, a collimator, a grating set, a reimaging lens assembly and a focal plane array (FPA) detector. In this case the dispersive element exploits three transmissive sinusoidal-phase grating rotated in 60° increments to disperse incoming light in multiple directions (projection angles) and orders (azimuth angle of the rotated grating). The 2D projections at the detector plane depends on the rotation angle of the grating and also the projection angles of the scene with respected to the optical axis of the imaging system. As according to the central-slice theorem [77] the 3D data can be restored through the 2D Fourier transform of the projection slice [1, 77] under algorithms such as the Expectation-Maximization (EM) [1].

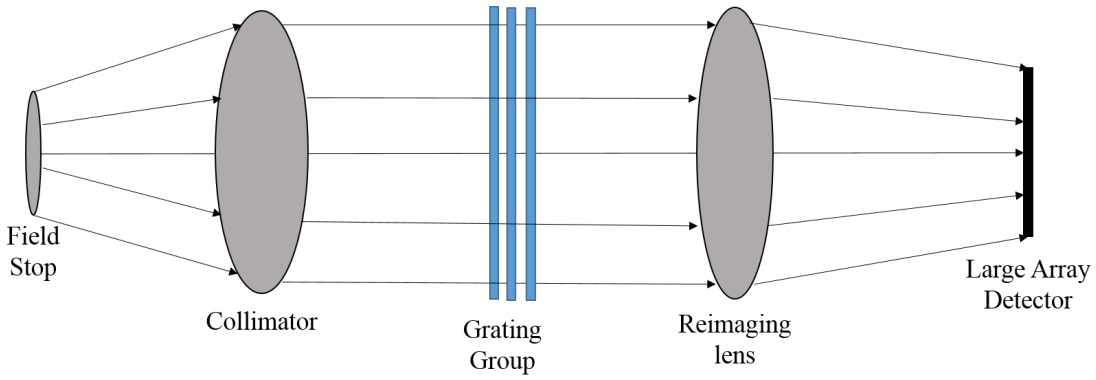

Figure 1.1: Schematic of Computed Tomographic Imaging Spectrometer which consists of five parts: the field stop, the collimator, the grating group, the reimaging lens and a large format detector. Image source is from [1].

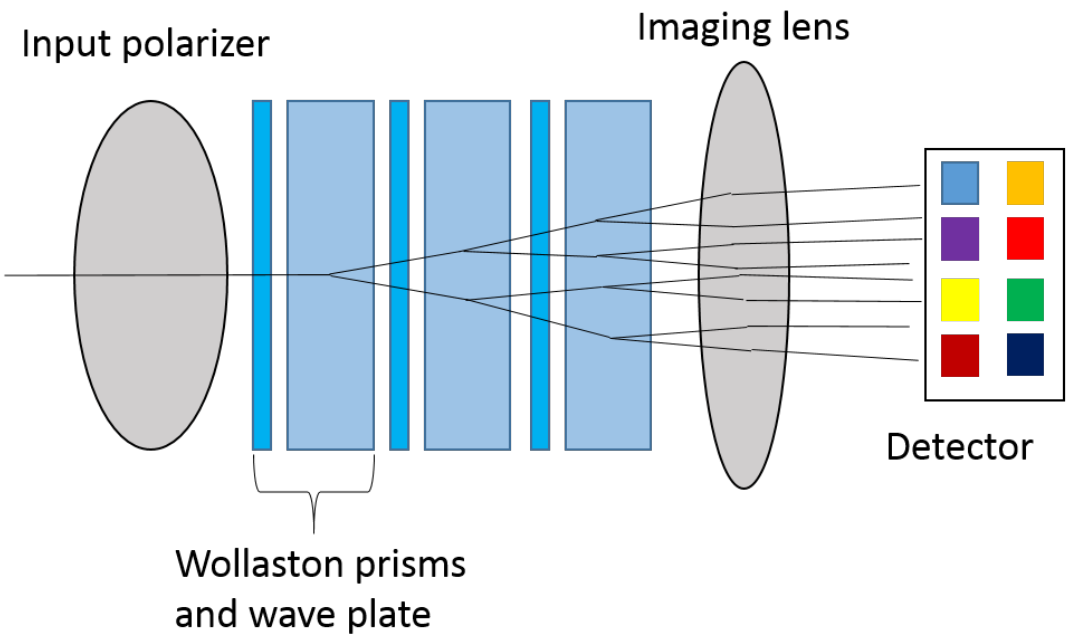

Figure 1.2: Schematic of the Image Replicating Imaiging Spectrometer (IRIS) system which utilises the coherent fibre bundle as the reformatting media [2].

Image Replicating Imaging Spectrometer (IRIS) [78, 79] is an electro-optical based multispectral imaging system which de-multiplexes spatial spectral multiplexed data without the need of software image reconstruction. Examples of IRIS has been the sandwich of Lyot filter [80] and the Wollaston beamsplit polarisers for demultiplex spatial-spectral information as shown in Fig. 1.2 [79]. In the heart of the IRIS it is the birefringent spectral demultiplexor (BSD) which consists of a wave plate and a Wollaston prism to resolve the polarised input into two orthogonally polarised beams and the spectral transmission is dependent on the spectral-polarisation characteristics of the reflected light from the scene. The system achieves 2^N spectral bands of data by cascading N number of BSD units in the IRIS. Such optical design has a high optical efficiency with small attenuation due to transmission loss of filters.

Image Mapping Spectrometry (IMS) [61] utilises a set of strip mirrors which oriented at individual tilt angles as image slicer for the redirection of incoming rays. As a consequence, the image of the scene is segmented into a number of sliced subimages which are then dispersed by dispersion element such as prisms or gratings and they are then subse-

quently reimaged onto the FPA. Image reconstruction is simply achieved by integrating the subimages. Spectral resolution in such a system is typically about 3.3 nm over 450 nm to 650 nm with 80 channels. However, the performance of such system is heavily dependent on the precision of the slicing mirror assembly which is a costly component making the overall system very expensive to implement.

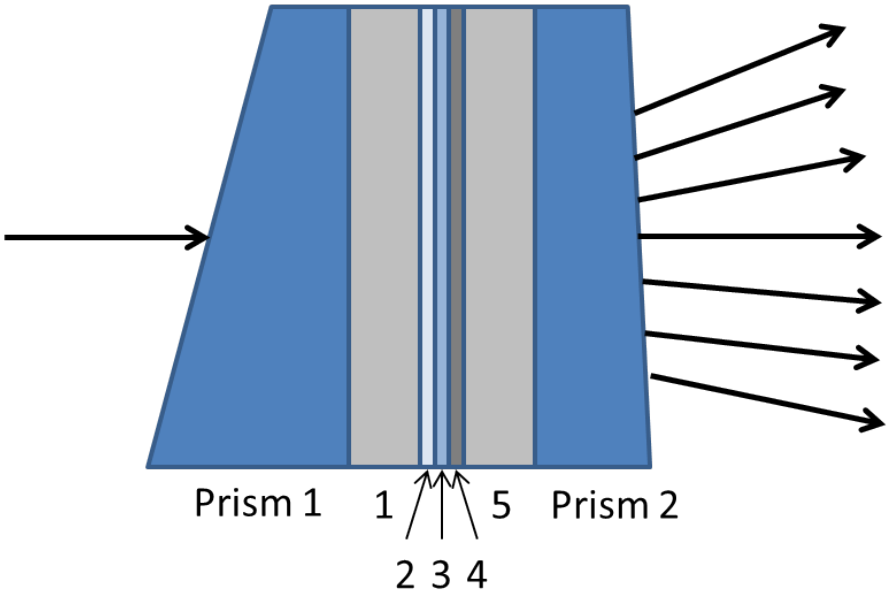

Figure 1.3: Schematic of the Prism-Grating-Prism compound which is a transmissive grating module sandwiched by two prisms. The grating module contains 1) longpass filter, 2) covering glass, 3) grating 4) substrate glass and 5) shortpass filter. Incoming ray bundle enters PGP from the left side and multiple dispersed rays emergent from the right hand side. Image source is from [3].

Prism-Grating-Prism (PGP) spectrograph was invented as a compact low-cost spectral imaging system for industrial and research applications [3]. The schematic of the PGP structure is shown in Fig. 1.3 and the assembly is composed of one transmissive grating module sandwiched by two prisms to optimise the dispersion characteristics through the adjustment of thickness and angles of the prism. The long and low pass filters set the spectral range of optical transmissions of the system. Such design provides excellent optical performance over large spectral range from 320 nm to 2700 nm with high diffracion efficiency up to 70% and polarisation-independent throughput. The design is suitable for tubular optomechanical platforms making a stable and compact system.

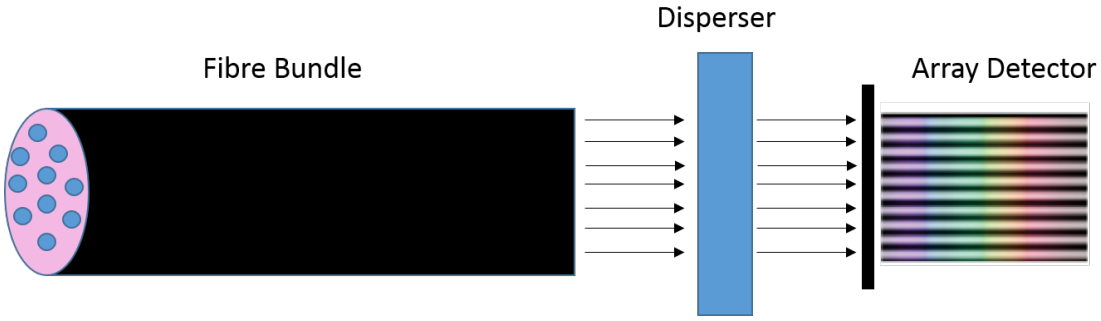

Figure 1.4: Schematic of Fibre-reformatting imaging spectrometry shows the coherent fibre bundle as the reformatting media and. Image source is from [2].

Fibre-reformatting imaging spectrometry (FRIS) [2, 81] is the technique which reformat 2D image into a linear array through the fibre bundle which functions as a slit, and they are then dispersed and subsequently integrated coherently by the detector (see Fig. 1.4). The drawbacks of this design is the focal ratio degradation [82] due to change of phase and also it suffers from modal noise especially when it is deployed for high spectral resolution applications [83].

1.3 Coded Aperture Snapshot Spectral Imager (CASSI)

Coded Aperture Snapshot Spectral Imager (CASSI) has been one of the most remarkable snapshot spectral framework which has been widely studied in the past decade [60, 64, 71, 72, 84–88, 88–91]. The theory behind CASSI is *Compressive Sensing* [92–94] which will be discussed in the next section. The working principle of compressive snapshot spectral imaging is the "Mask & Dispersive element" process which is schematically outlined in Fig. 1.5. The figure depicts an input 2D signal (1D spatial and 1D spectral) which is spatially modulated by the coded aperture mask and subsequently dispersed along the spatial dimension. The resulting spatial spectral multiplexed information is then integrated by a row of the focal plan array (FPA) detector. In the case of real scene which contains 3D matrix of information, i.e. 2D spatial and 1D spectral data, the measurement of the 3D data at the detector will be in a 2D format such that the spectral information will be 'mixed' with the spatial content. More details of the CASSI will be given in the

compressive sensing theory section.

The very first version of CASSI [95] was a Dual-Disperser CASSI (DD-CASSI) structure which utilised two sets of dispersion optics, one to function as positive dispersion while the other served as counter-dispersion which cancels out the dispersion by the first set (see Fig. 1.6). The result is effectively to recover the dispersed information back to the original spatial structure, instead of having the spectral-spatial-multiplexed information at the detector. Subsequently, the work in the Single Disperser CASSI (SD-CASSI) [60] was proposed in 2008 which employed only one arm configuration directly acquire spectral-spatial multiplexed information at the detector. In this case the spatial spectral information of the scene can be fully recovered under the compressive sensing theory [92–94] with the assumption that the scene can be represented in sparse condition. The SD-CASSI consists of one coded aperture mask and one dispersive element. The reported proto-

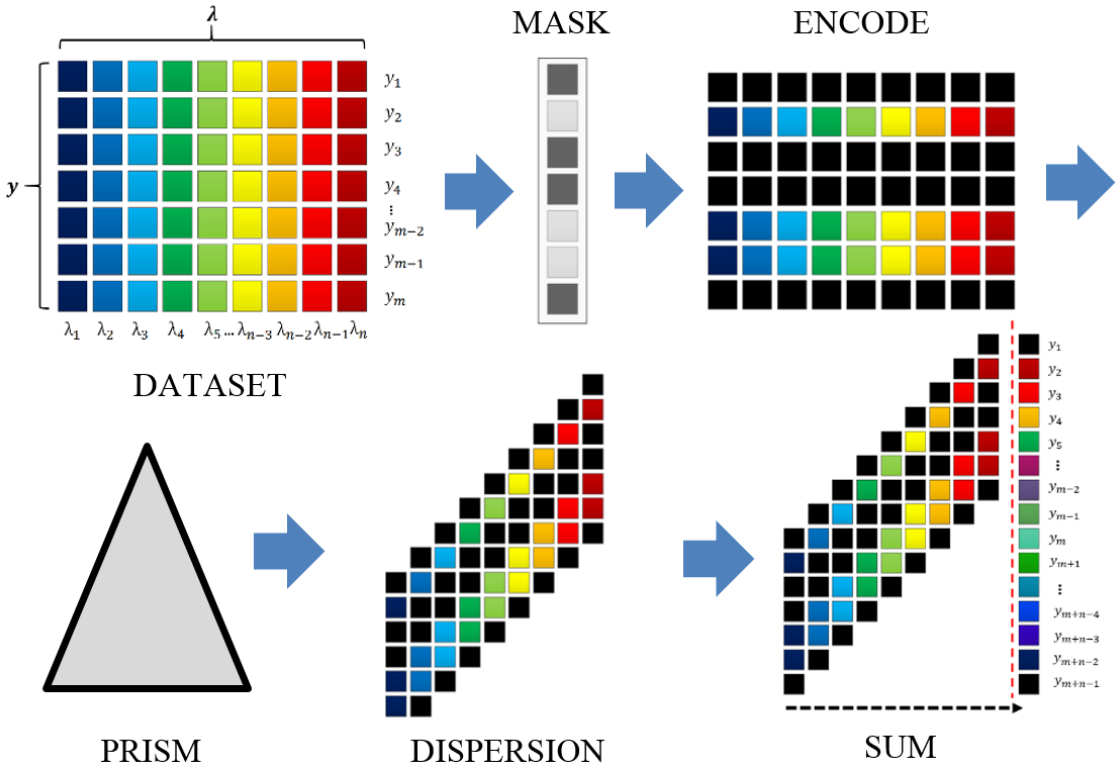

Figure 1.5: Schematic of CASSI showing three stages in CASSI "Mask & Dispersive element" model: Original multispectral data are encoded by an array of coded aperture mask; encoded dataset is sheared by the prism and eventually the spatial-spectral multiplexed data is integrated at detector.

type of the SD-CASSI utilised off-the-shelf optics as a proof-the-concept system [60]. The 2nd generation SD-CASSI was reported by using a Double Amici Prism [96] as the dispersion element. This version reduced optical aberration caused by the equilateral prism which was employed in the SD-CASSI. One drawback in the 2nd generation SD-CASSI [97] was the small aperture which was improved in the 3rd generation SD-CASSI. This version adopted an electrical piezo-device for coding the scene in multi-frame measurements which dramatically improved the reconstruction results [97]. The latest version known as Ultraviolet-Visible CASSI (UV-CASSI) [98] was the extension of the system for ultraviolet-visible spectral range applications [99]. The main feature of the UV-CASSI is that the double Amici prism was placed in the collimating space of the relay optics as an effective means for correcting the aberration caused by dispersion element. Furthermore, the relay optics of the system was optimized by optical software to achieve optimum optical performance [97].

As depicted in Fig. 1.7 the recent development of CASSI has improved the accuracy of multiplexed spectral-spatial data recovery and the resolutions of SSI system rather significantly. One design was the Dual-Camera CASSI which adopted a conventional

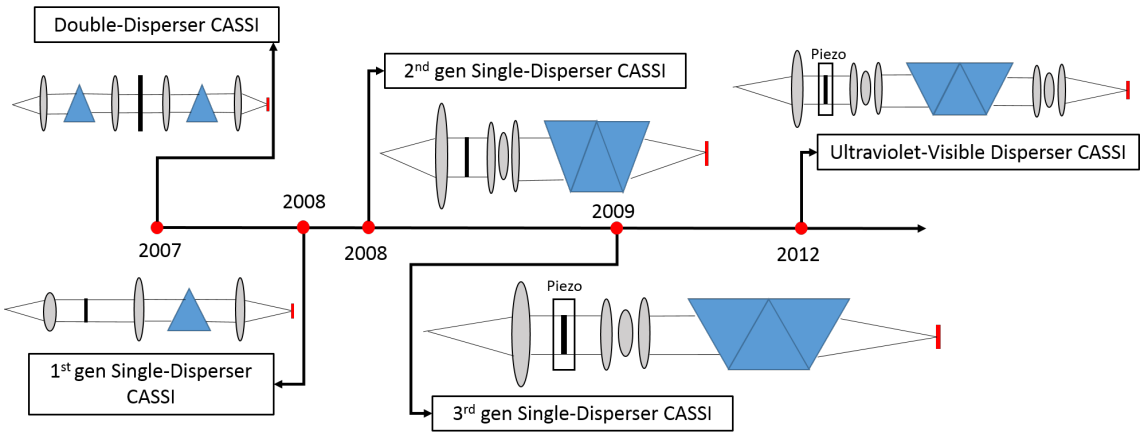

Figure 1.6: Overview of historical developments in CASSI: Double-Disperser CASSI in 2007, 1st generation Single-Disperser CASSI in 2008, 2nd generation Single-Disperser CASSI in 2008, 3rd generation Single-Disperser CASSI in 2009 and Ultraviolet-Visible CASSI in 2012. The schematic diagram depicts key components: coded aperture mask (in black), digital micromirror device as spatial modulator, prism (in blue) and diffraction grating as spectral modulator, optical lens (in grey) and spectral optics, and the detector (in red).

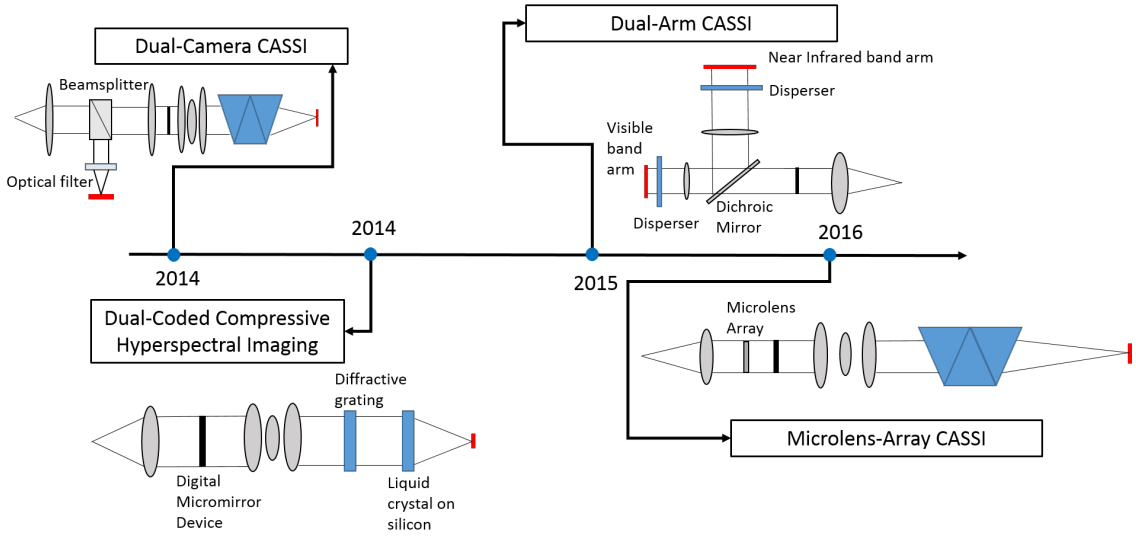

Figure 1.7: Overview of historical development of CASSI: Dual-Camera CASSI in 2014, Dual-Coded Compressive Hyperspectral Imaging in 2014, Dual-Arm CASSI in 2015 and Microlens-Array CASSI in 2016. The figure highlights key components of systems: coded aperture mask (in black), digital micromirror device as spatial modulator, prism (in blue) and diffraction grating as spectral modulator, optical lens (in grey) and spectral optics and the detector (in red).

CASSI architect in one arm, with another arm to image the scene through a beam splitter without any spectral/spatial modulator [91]. The purpose of the second arm information is to augment the CASSI measurements thereby to improve the accuracy of the spatial-spectral recovery of the scene. Another design was the use of a dual-Coded Compressive Hyperspectral Imaging architect through two high speed spatial light modulators. In this design a digital-micromirror-device (DMD) and a Liquid Crystal on Silicon was employed as spatial and spectral modulator respectively. One drawback of these designs was the small aperture of the system due to the lengthy relay optics to bridge the images between multiple modulators. Other factors, such as the limited pixels in the focal plane array, imposed constraints to compromise between spatial and spectral resolution in SSI systems [100, 101]. Another design which was known as the Dual-Arm VIS/NIR Compressive Spectral Imager extended the SD-CASSI to near-infrared region with good results [102]. The use of Microlens-Array in the CASSI which adopted microlens array to slice the 3D scene through each microlens element had been reported [103, 104]. While most of the present work focuses on improving spatial resolution of the SSI system, the

work on flexible, tuneable SSI is heavily lacking.

1.4 Contributions and Thesis Structure

This study contributes three areas in the snapshot imaging research:

1. Spectral tuneable snapshot spectral imager using double prism CASSI (DP-CASSI):

   The spectral tuning of the proposed DP-CASSI is achieved by adjusting the air gap displacement of the dual prism assembly. Typical spectral shifts of about 5 nm at 450 nm and 10 nm at 650 nm wavelength have been achieved in the present design when the air-gap of the dual prism is changed from 3.44 mm to 5.04 mm. The details of the design and the performance of the tuneable DP-CASSI have been submitted for two journals and one conference paper publications:

   - **M. Ding**, P. WT Yuen, J. Piper, P. Godfree, A. Chatterjee, U. Zahidi, Senthuran Selvagumar, D. James and M. Richardson, "Tuneable snapshot multispectral imaging system using a dual prism as dispersive element". *Submitted* to Optical Engineering, 2018 (review in progressing).
   - **M. Ding**, P. WT Yuen, J. Piper, P. Godfree, A. Chatterjee, U. Zahidi M. Gunes, S. Selvagumar, D. James and M. Richardson, "Design of a tunable snapshot multispectral imaging system through ray tracing simulation", J. Imaging, 2019; 5(1); 9.
   - **M. Ding**, P. WT Yuen, U. Soori, S. Selvagumar, M. Gunes and U. Zahidi, "Enhanced CASSI snapshot imager using dual prism dispersion", Poster paper, Hyperspectral Imaging & Applications Conference, 2016.

2. Design of the Single-Prism CASSI (SP-CASSI):

   By using a tailored design of lens and optical components, the SP-CASSI has been optimised with throughput F/4 and the details of the design has been fully documented in an IEEE conference:

- **M. Ding**, P. WT Yuen and M. Richardson, "Design of single prism coded aperture snapshot spectral imager using ray tracing simulation", IEEE British and Irish Conference on Optics and Photonics, pp. 1-4, 2018.
- **M. Ding**, P. WT Yuen and M. Richardson, "Design of single prism coded aperture snapshot spectral imager using ray tracing simulation", Conference Paper to be rewritten for Journal of Imaging submission.

3. Improvement of spectral accuracy in wavelength tuneable DP-CASSI:

   The accuracy of the spatial spectral multiplex in the DP-CASSI is further studied and the spectral accuracy is found to be improved significantly when the number of spectral wavelength is reduced from 50 bands to 15 bands. This contribution is in the form of a paper to be submitted to the Journal of Imaging:

   - **M. Ding**, P. WT Yuen, J. Piper, P. Godfree, A. Chatterjee, U. Zahidi, Senthurran Selvagumar, D. James and M. Richardson. "Improvement of spectral accuracy in wavelength tuneable double prism CASSI (DP-CASSI)", Paper in preparation for the Journal of Imaging Submission.

The layout of the thesis is as follow:

- Chapter 1: Introduction: motivations and achievements of the present research.
- Chapter 2: Present the prior work in snapshot spectral imaging and to give an overview of the CASSI framework and working principles.
- Chapter 3: Provide the details of optical design of four CASSI systems: (a) Single-Prism CASSI, (b) Double-Amici CASSI, (c) Ultraviolet-Visible CASSI and (d) Dual-Prism CASSI.
- Chapter 4: Summarise the simulation results for three CASSI systems: (a) SP-CASSI, (b) UV-CASSI and (c) DP-CASSI and the simulated images are decompressed by using the TwIST algorithm as mentioned in Chapter 2.

- Chapter 5: Concludes the work done in this research and to propose future work.

Chapter 2

COMPRESSIVE SENSING (CS)

Compressive Sensing (CS) has been a popular subject since the turn of century and it has been widely deployed for many applications such as in magnetic resonance imaging [105, 106], radar application [107, 108], mathematics and signal processing [109], information security [110] and hyperspectral imaging [111]. The popularity stems from the fact that compressive sensing works without the Nyquist limitations [109] and it asserts that signals can be recovered from far fewer sampling than the original dimensions of information when the signal in question can be represented in sparse condition [109, 112]. In the spectral sensing context this implies that the full spectral characteristics of the scene can be obtained from just a few measurements of spectral data. This is a typical inverse problem and the solutions are underdetermined meaning that the equations to be solved are far less than the number of parameters. However, near 'exact' solutions still can be found for these ill-posed problems when 'proper' constraints are imposed [113]. The general conditions for obtaining 'near exact' solutions in CS requires: (1) the signal of interest is sparse meaning that they can be represented in some basis where zeros are in majority. This is so-called the sparsifying basis. (2) Incoherence or independence between the sparsifying basis and the sensing basis. The sensing basis is the linear measurement of the data, e.g., the sampling of small number of projection of the image data and the solution will be dependent on this sensing basis with respect to the actual sparsity of the

image [109].

2.1 Compressive Sampling

Many signal/image systems for instance in remote sensing, radar imaging, astronomic and microscopy imaging, the data can be fully observed through a set of linear operations even when the intrinsic features of the scene cannot be measured directly. Typical examples such as applications for image denoising, restoration and demosaicing applications, the intrinsic signal x can be recovered from the observation data y through the measurement operator K (measurement matrix), i.e. $y = Kx$ [114]. This is a typical Linear Inverse Problem (LIP) in which the approximated signal x can be recovered through the estimated $\tilde{x}$ for the given observation y provided that it is linearly dependent on the signal. The posedness of the LIP is defined by the existence of an unique solution and whether it is continuously dependent on the initial data [115]. In practice most LIPs in engineering applications are often ill-posed without *priori* knowledge. Through compressive sensing theory it provides a means to find solutions even in underdetermined conditions when the observations are fewer than the dimension of the signal, provided that the signal in question is sparse in nature.

In general, natural signals can be concisely represented by suitable basis [109] due to the inherent compressive characteristic of natural signals [116]. The sparse signal $\mathbf{f} \in \mathbb{R}^n$ can be linearly span in the sparse basis $\boldsymbol{\Psi} \in \mathbb{R}^{n \times n}$ as

$$\mathbf{f} = \boldsymbol{\theta}\, \boldsymbol{\Psi}, \tag{2.1}$$

where $\boldsymbol{\theta}$ is the sparse representation (i.e. coefficient) of the signal in the sparsifying basis $\boldsymbol{\Psi}$. The sparsity of the signal is known as S-sparse when the signal $\boldsymbol{\theta}$ has S number of non-zero elements [94]. Fourier transform or wavelet transform have been the most commonly employed sparsifying basis in many engineering applications [117]. As mentioned the sensing scheme or sampling protocol is crucially important to correlate the sparse signal

in the observation space. The sensing matrix in the sparse domain $\mathbf{\Phi} \in \mathbb{R}^{m \times n}$ represents the scheme for measuring the sparse signal along the sensing basis. Then the system measurement matrix is a product of the sensing and the sparse matrix: $\mathbf{H} = \mathbf{\Phi\Psi} \in \mathbb{R}^{m \times n}$ where $m \ll n$ due to the smaller number of measurements than the dimension of the sparse signal. Every row in the m dimension represents each independent observation. Note that the basis of the signal ideally features high sparsity while the basis of the observation should contain highly dense information in order to capture meaningful measurements. This implies that the sensing basis is supposed to be incoherent to the sparsifying basis and the incoherency can be quantitatively assessed by [118],

$$\mu(\mathbf{\Phi}, \mathbf{\Psi}) = \sqrt{n} \cdot \max |\langle \varphi_i, \psi_j \rangle| \ , \ 1 \leq i, j \leq n, \tag{2.2}$$

where φ_i and ψ_j are the elements of the vector form $\mathbf{\Phi}$ and $\mathbf{\Psi}$ respectively, while i and j are the indices of the signal dimension. The above equation measures the maximum correlations of all basis pairs and a larger μ represents a higher correlation. The objective of sampling under compressive imaging theory is to search for highly incoherent basis pair, for instance, the Fourier and the time basis pair or the wavelet and the noiselet basis pair etc. [119]. In particular the random basis which features a Gaussian probability density function is highly incoherent to basis such as wavelet characteristics of higher order statistics [120], which may suggest that the use of the random coded aperture pattern as the measurement basis is appropriate for the CASSI work to be presented here in this thesis.

However, real world signal y in general is corrupted by additive noise and in many cases they are inexact, therefore the ideal form of $y = Kx$ is needed to take the noise or exactness factor into account:

$$\mathbf{g} = \mathbf{H}\boldsymbol{\theta} + \boldsymbol{\omega} = \mathbf{\Phi\Psi}\boldsymbol{\theta} + \boldsymbol{\omega}, \tag{2.3}$$

where $\mathbf{g}$ denotes the observation data and $\boldsymbol{\omega}$ represents the noise matrix. Note that the $\mathbf{H}$ is

normally not invertible and hence to solve the LIP problem when corrupted noise cannot be ignored the simple inversion $\boldsymbol{\theta} = \mathbf{H}^{-1}\mathbf{g}$ will not be applicable in general. Instead, the common way is to find an estimate of the $\boldsymbol{\theta}$ from the measurement $\mathbf{g}$ through the minimisation of the discrepancy of the $\left\|\mathbf{H}\tilde{\boldsymbol{\theta}} - \mathbf{g}\right\|_{l_2}^2$, where the l_2 norm $\|\cdot\|_{l_2}$ is:

$$\|\mathbf{x}\|_2 = \sqrt{\sum |x_i|^2}. \tag{2.4}$$

The L2 norm here represents the Euclidean distance along the length of the vector variable. Thus, the previous LIP can be rewritten as

$$\min_{\tilde{\boldsymbol{\theta}}} \left\|\mathbf{g} - \mathbf{H}\tilde{\boldsymbol{\theta}}\right\|_2 \quad \text{subject to } \|\mathbf{x}\|_0 \leq S. \tag{2.5}$$

where $\|\mathbf{x}\|_0$ is the number of nonzero elements which conforms to the S-sparsity. This unconstrained problem can be further rewritten to a constrained objective function as

$$\min_{\tilde{\boldsymbol{\theta}}} \frac{1}{2} \left\|\mathbf{g} - \mathbf{H}\tilde{\boldsymbol{\theta}}\right\|_2^2 + \|\mathbf{x}\|_0 . \tag{2.6}$$

Note that this constrained objective function solves the LIP problem through all possible sets within the sparse basis space (i.e. all S non-zero elements) and it is a classical combinatorial optimisation problem with prohibitive non-deterministic polynomial time hard (NP-hard) complexity [121, 122]. However, this can be converted into a manageable convex linear programming problem by using the L1 minimisation instead [123]. This methodology is also known as the basis pursuit.

Early analytic tools employed for studying the recoverability and stability of the signal x under compressive imaging theory has been making use the Restricted Isometry Property (RIP) of the measurement matrix K (i.e. the combined system matrix $\mathbf{H}$) [94, 112]. The RIP measures the 'onditioning' of the set of submatrices of $\mathbf{H}$ through a RIP parameter of δ_S :

$$(1 - \delta_S) \|b_\Omega\|_2^2 \leq \|H_\Omega b_\Omega\|_2^2 \leq (1 + \delta_S) \|b_\Omega\|_2^2 , \tag{2.7}$$

where $\delta_S \in (0,1)$ and b is any S-sparse vector. The Ω represents the set of indices of the non-zero elements of S-sparse signal and the H_Ω is the submatrices of Ω selected from the system matrix $\mathbf{H}$. The condition states that the smaller the δ_S, the better is the submatrices H_Ω for retaining the sparse condition, i.e. the measurement matrix retains the linear property of all the sub-vectors in the sparse basis thus the sparse signal x can be recovered more faithfully under this measurement matrix.

2.2 Signal recovery: Reconstruction Algorithm

There are five common approaches for solving the LIP problem [121]: the greedy pursuit, convex optimisation, bayesian framework, nonconvex optimization and brute force methods. Since this thesis concerns mainly on the optical system design and therefore three of the above commonly adopted methodologies for recovering signal under compressive sensing are outlined here.

2.2.1 Orthogonal Matching Pursuit

Algorithm 1 Orthogonal Matching Pursuit

1: **Initialisation.** Input signal $\mathbf{u} \in \mathbb{R}^m$, dictionary matrix $\mathbf{D} \in \mathbb{R}^{m \times n}$, index set Ω, the residual $\mathbf{r}_0 = \mathbf{u}$ and initial counter $i = 1$.
2: **Identification.** Find maximum correlated column n_k with the residual from the dictionary $\mathbf{D}$: $n_k = \arg\max_n |\langle \mathbf{r}_{k-1}, d_a \rangle|$ and $\Omega_k = \Omega_{k-1} \cup n_k$.
3: **Estimation.** Find the best coefficients for the signal approximation of the chosen column. $\mathbf{x}_k = \arg\min_{\mathbf{y}} \left\| \mathbf{u} - \mathbf{D}_{\Omega_k} \mathbf{y} \right\|_2$.
4: **Iteration.** Update the residual: $\mathbf{r}_k = \mathbf{u} - \mathbf{D}_{\Omega_k} \mathbf{x}_k$. Increment k, repeat step 2 to step 4 until stopping criterion holds.
5: **Output.** Return the $\mathbf{x}$ with components $x(n) = x_k(n)$ for $n \in \Omega_k$ and $x(n) = 0$ otherwise.

Orthogonal Matching Pursuit is a greedy algorithm which finds the solution by iteratively matching the sparsed signal structure with one or several sparse coefficients selected from the dictionary [121]. The most computational demanding part of the algorithm is the computation of the maximum inner product via the matrix-vector multiplication which

has a complexity of $O(N^2)$:

2.2.2 Gradient Projection for Sparse Reconstruction (GPSR)

Under this scheme the sparse reconstruction [124] is approached by turning the LIP into a convex optimisation problems through a Bound-Constrained Quadratic Programming (BCQP) formulation:

The signal in the objective function is transformed into a 2D wavelet domain:

$$\hat{f}(\tau) \;=\; W \;\cdot\; \arg\min_{\theta}\left[\frac{1}{2}\,\|g-\Phi W\theta\|_2^2+\tau\,\|\theta\|_1\right], \tag{2.8}$$

where W is the 2D wavelet transform and the θ is the coefficients in the wavelet domain. The approach is to find the best wavelet coefficients which minimises the objective function. The GPSR method transforms the objective function in Eq. 2.8 to the BCQP formation with $\mathbf{x} = \mathbf{u} - \mathbf{v}, \mathbf{u} \geq 0, \mathbf{v} \geq 0$ as,

$$\min_{\mathbf{z}}\; \mathbf{c}^T\mathbf{z} + \frac{1}{2}\mathbf{z}^T\mathbf{B}\mathbf{z} \equiv F(\mathbf{z}), \text{subject to}\, \mathbf{z} \geq 0, \tag{2.9}$$

where

$$\mathbf{z} = [\mathbf{u}\,\mathbf{v}]^T,\; \mathbf{b} = \mathbf{A}^T\mathbf{y},\; \mathbf{c} = \tau\mathbf{1}_{2n} + [-\mathbf{b}\,\mathbf{b}]$$

and

$$\begin{bmatrix} \mathbf{A}^T\mathbf{A} & -\mathbf{A}^T\mathbf{A} \\ -\mathbf{A}^T\mathbf{A} & \mathbf{A}^T\mathbf{A} \end{bmatrix}$$

The algorithm searches for the best value along the negative gradient and subsequently to project the gradient onto the nonnegetive splitting part. A backtracking line search is then employed until a sufficient decrease in the BCQP function is found. The projection is in the form of:

$$\alpha_0 \;=\; \frac{(\mathbf{g}^{(k)})^T\mathbf{g}^{(k)}}{(\mathbf{g}^{(k)})^T\mathbf{B}\mathbf{g}^{(k)}}, \tag{2.10}$$

where the vector $\mathbf{g}_i^{(k)} = (\nabla F(\mathbf{z}^{(k)}))_i$, if $\mathbf{z}^{(k)} > 0$ or $(\nabla F(\mathbf{z}^{(k)}))_i < 0$.

Since the GPSR adopts the 2D wavelength and inverse transform, the transformation processes present substantial computational cost to the algorithm. The wavelet transform has complexity of $O(n^2)$ and it can be reduced to $O(n)$ if the fast wavelet transform is employed [125].

Algorithm 2 Gradient Projection for Sparse Reconstruction

1: **Initialisation.** Given $\mathbf{z}^0$, choose parameters $\beta \in (0,1)$ and $\mu \in (0,0.5)$, initial counter $k = 0$.
2: **Precomputing.** Compute α_0 and replace α_0 by $\text{mid}(\alpha_{min}, \alpha_0, \alpha_{max})$.
3: **Backtracking Line Search.** Choose $\alpha^{(k)}$ to be the first number in the sequence α_0, $\beta\alpha_0$, $\beta^2\alpha_0$,... such that

$$F\left(\left(\mathbf{z}^{(k)} - \alpha^{(k)}\nabla F\left(\mathbf{z}^{(k)}\right)\right)_+\right) \leq F\left(\mathbf{z}^{(k)}\right) - \mu\nabla F\left(\mathbf{z}^{(k)}\right)^T\left(\mathbf{z}^{(k)} - \left(\mathbf{z}^{(k)} - \alpha^{(k)}\nabla F\left(\mathbf{z}^{(k)}\right)\right)_+\right), \quad (2.11)$$

and set $\mathbf{z}^{(k+1)} = (\mathbf{z}^{(k)} - \alpha^{(k)}\nabla F(\mathbf{z}^{(k)}))_+$.
4: **Iteration.** Perform convergence test and terminate with approximate solution $\mathbf{z}^{(k+1)}$ if it is satisfied; otherwise set $k = k + 1$ and return to 1.

2.2.3 Two-step Iterative Shrinkage/Thresholding (TwIST)

TwIST utilises the Iterative Shrinkage/Threshold (IST) approach to convert the convex unconstrained optimisation problems into a linear inverse problems for image reconstruction under the compressive sensing theory. The IST type of algorithms have drawbacks of slow convergence particularly when the linear observation operator model is ill-posed. TwIST employs a regularization framework to constrain the objective function for achieving faster convergences even for strongly ill-posed situations [126]:

$$f(x) = \frac{1}{2}\|\mathbf{y} - \mathbf{A}\mathbf{x}\|_2^2 + \tau\Phi(x), \quad (2.12)$$

where $\mathbf{A}$ is the linear observation operator. Φ is regularization function used for constraining the objective function to find an estimate $\mathbf{x}$ and total variation regularizer is commonly

employed [127].

Unlike conventional IST methods, TwIST estimates $\mathbf{x}_{i+1}$ based on two previous weighted iterations $\mathbf{x}_{i-1}$ and $\mathbf{x}_i$ as

$$\mathbf{x}_1 = \mathbf{\Gamma}_\lambda(\mathbf{x_0}), \tag{2.13}$$

$$\mathbf{x}_{i+1} = (1-\alpha)\mathbf{x}_{i-1} + (\alpha-\beta)\mathbf{x}_i + \beta\mathbf{\Gamma}_\lambda(\mathbf{x}_i), \tag{2.14}$$

where original denosing function $\mathbf{\Gamma}_\lambda$ as

$$\mathbf{\Gamma}_\lambda(y) = \arg\min_x \left\{ \frac{d_y^2(x)}{2} + \lambda\Phi(x) \right\}$$

where d_y denotes $\|x-y\|$ adopts the soft-thresholding, or weighted L1-norm $\Phi(x)$ e.g. the Total Variation as the regularizer, in order to be obtained in closed form. The shrinkage method splits the part $\mathbf{A}_i$ in the conventional linear problem $\mathbf{A}_i\mathbf{x} = \mathbf{b}$ into $\mathbf{A}_i = \lambda\mathbf{D}_i + \mathbf{K}^T\mathbf{K}$. The non-negative diagonal matrix $\mathbf{D}_i$ shrinks the components of $\mathbf{x}_{i+1}$. Further take $\mathbf{C} = \mathbf{I} + \lambda\mathbf{D}_i$ and $\mathbf{R} = \mathbf{I} - \mathbf{K}^T\mathbf{K}$ in the $\mathbf{A}_i$ and combine with the soft-thresholding, then we have new denoising function,

$$\mathbf{\Gamma}_\lambda(x) = \mathbf{\Psi}_\lambda(x + \mathbf{K}^T(y - \mathbf{K}x)). \tag{2.15}$$

The weight parameters α and β are assigned by two real numbers ξ_1 and ξ_m which constrain the convergence of the TwIST algorithm, as follows,

$$\alpha = \hat{\rho}^2 + 1, \tag{2.16}$$

$$\beta = \frac{2\alpha}{\xi_1 + \xi_m}. \tag{2.17}$$

where $k = \xi_1 \,/\, \xi_m$ and

$$\hat{\rho} = \frac{1 - \sqrt{k}}{1 + \sqrt{k}}.$$

Algorithm 3 Two-step Iterative Shrinkage Thresholding

1: **Initialisation.** Given $\mathbf{y}_0$, denoising function Ψ_λ, regularizer function Φ, set parameters τ, λ_1, λ_m and initial iteration i.
2: **Precomputing.** Compute the initial $\mathbf{x}_0$, k, $\hat{\rho}$, α, β.
3: **Two-Step Shrinkage/Thresholding.**

$$\mathbf{x}_1 = \mathbf{\Gamma}_\lambda(\mathbf{x_0}), \tag{2.18}$$
$$\mathbf{x}_{i+1} = (1-\alpha)\mathbf{x}_{i-1} + (\alpha-\beta)\mathbf{x}_i + \beta\mathbf{\Gamma}_\lambda(\mathbf{x}_i), \tag{2.19}$$
$$\mathbf{\Gamma}_\lambda(x) = \mathbf{\Psi}_\lambda(x+\mathbf{K}^T(y-\mathbf{K}x)). \tag{2.20}$$

4: **Iteration** Perform convergence test and terminate with approximate solution x_{i+1} if it is satisfied; otherwise set $i = i + 1$ and return to 3.

2.3 The coded aperture snapshot spectral imaging (CASSI) Model

Fig. 1.5 illustrates how compressive sensing is implemented in the CASSI system. Assuming the signal of interest has spectral density $f_0(x,y,\lambda)$ where x and y represent the 2D spatial dimensions, λ is the 1D spectral vector. For a given 2D coded aperture with pattern $M(x,y)$ in which the smallest distance between the coded pattern (pixel pitch) is represented by Δ_C, the pattern is in a discrete form with zeros and ones. The pitch of the coded aperture and that of the detector affects the imaging resolution and ideally $\Delta_C = q\Delta_D$ where q is an integer and $\Delta_D$is the pitch of the detector. When the signal is encoded by the coded aperture, the spectral density $f_0(x,y,\lambda)$ is modulated by M:

$$f_1(x,y,\lambda) = f_0(x,y,\lambda)T(x,y), \tag{2.21}$$

where $x,y,\lambda \in \mathbb{R}$, $0 \le x \le m$, $0 \le y \le n$, $0 \le \lambda \le l$, and T(x,y) is the transmission of light through the aperture. Then the dispersive prism modulates the encoded signal in the spectral domain. If the effective dispersion coefficient of the prism is $\alpha(\lambda)$ and the dispersion of the prism $S(\lambda)$ with respect to the centre wavelength λ_C in the spectral range Ω is $S(\lambda) = \alpha(\lambda)(\lambda - \lambda_C)$, then the image of the detector $g(x,y)$ receives a multiplex of

modulated spectral and spatial contents in the x-direction can be expressed by:

$$g(x,y) = \int_{\Omega} f_0(x+S(\lambda),y,\lambda)T(x+S(\lambda),y)d\lambda. \tag{2.22}$$

The measured spectral density at the detector integrates the spatial shift of spectral channels $\lambda\{1,2,\ldots,l\}$ and the modulated spatial content of the scene over the spectral range of the system. The spectral resolution is constrained predominantly by the dispersion capability of the prism and the number of resolved spectral bands $l = p\left[\frac{\lambda_1-\lambda_L}{\Delta_C}\right]$, where $[\cdot]$ represents the maximum integer value and p is the magnification constant.

Therefore, Eq. (2.22) can be written as

$$g_{m,n+l-1} = \sum_{k=1}^{l} (f_k)_{m,n+k-1} T_{m,n+k-1} + \omega_{mn}, \tag{2.23}$$

and in operator form where T is replaced by the operator $\mathbf{H}$,

$$\mathbf{g} = \mathbf{H}\mathbf{f} + \mathbf{W}, \tag{2.24}$$

where $\mathbf{H} \in \mathbb{R}^{[m\cdot(n+l-1)]\times(m\cdot n\cdot l)}$ denotes the observation operator, $\mathbf{f} \in \mathbb{R}^{(m\cdot n\cdot l)\times 1}$ and $\mathbf{g} \in \mathbb{R}^{[m\cdot(n+l-1)]\times 1}$ denotes the detector measurement matrix and the recovered signal respectively and the $\mathbf{W}$ includes all possible noise sources. The g_{mn} is the multiplex measurement version of f_{mnk} and if the spectral data cube f_{mnk} can be expressed as $f = \Psi\theta$ where Ψ is the inverse transform (eg wavelet) and θ is the three dimensional coefficient decomposition of f_{mnk}. Then Eq. (2.23) can be rewritten as:

$$g_{mn} = H\Psi\theta + \omega_{mn}, \tag{2.25}$$

where the linear operator $\mathbf{H}$ represents the system forward model. The reconstruction of f_{mnk} is attained by solving the reconstruction algorithm to recover f_{mnk} from g_{mn} through

the optimisation of the LIP:

$$\hat{f}(\tau,\Gamma) \;=\; \Psi \cdot \arg\min_{\theta}\Big[\frac{1}{2}\left\|g - H\Psi\theta\right\|_2^2 + \tau\left\|\Gamma(\theta)\right\|_1\Big], \tag{2.26}$$

where g is the measurement data and H accounts for the effects of the coded aperture and the dispersion. The first term minimises the l_2 difference between the model and the measurement g_{mn}. The variable $\tau > 0$ is the regularization parameter that balances the conflicting tasks of minimizing the least square of the residuals and at the same time to yield a sparse solution. It can be seen that the sparser the source f_{mnk} in θ, the better the performance of the reconstruction algorithm. The regularizer Γ can be in various forms and the Total Variation (TV) [127] regularization is adopted in this work for enhancing spatial smoothing. The TV regularizer has a discrete formulation given by

$$\Gamma_{TV}(f) = \sum_i \sqrt{(\Delta_i^h f)^2 + (\Delta_i^v f)^2}, \tag{2.27}$$

where Δ_i^h and Δ_i^v denote discrete gradient operators in the horizontal and vertical directions. The regularization product is in the l_1 norm which can be minimized by exploiting Chambolle projection algorithm [127] to compute the projection of the weighted estimate from the the convex dataset. The tuning parameter τ and the solution $\hat{f}$ in Eq. (2.26) affect the balance between spatial smoothness and the spectral recovery fidelity.

Chapter 3

SYSTEM DESIGN

The design of modern optical system nowadays routinely employs *Computer Aided Software* which helps scientists and engineers to effectively construct the optical system, its performance evaluation and optimisation without tedious manual mathematical calculations and large-scale ray tracing. Many optical design softwares have been developed and they are readily available from commercial off the shelf. Choices are available for engineers and researchers for the design of camera lenses, mirrors, thermal imaging systems and diffractive optical systems, such as the Zemax®, Optica®, CODE V®, ASAP® and FRED®. As one of the commercial optical design programs, OSLO® owned by Lambda Research Corporation has been widely used for the design, simulation and analysis of optical systems. Standard features such as Modulation Transfer Function (MTF), Point Spread Function (PSF) and Spot Diagram (SD), and design tools such as aberration controls and merit functions are readily available for system optimisation. OSLO also provides a special macro programming language *Compiled Command Language* which allows the development of specialised optical systems through a script. In this chapter, the design of CASSI frameworks, particularly the Single-Disperser CASSI, Double-Amici CASSI and Ultraviolet-Visible CASSI, will be presented here through the OSLO design tools. The pros and cons of individual systems will be commented. The main goal of this project is (1) to develop a proof-of-concept wavelength-tuneable system based on the

CASSI framework and it is named as the Dual-Prism CASSI (DP-CASSI); (2) to demonstrate the optical performance of CASSI prototypes by using optical design software. The specific design and analysis of the DP-CASSI system will be demonstrated under the OSLO environment and the details will be presented in the next chapter.

3.1 Optical System Design Procedure

Optical system is always designed to serve some specific needs of applications. Those needs can be specified as optical requirements to determine the initial system. The critical considerations for a system's needs are mainly focusing on three questions in the first place, whether it is an imaging system or non-imaging system, what is the working spectral range for target/scene (visible/near infrared/shortwave infrared/thermal bands) and what is the environment conditions (temperature, radiation, moisture, illumination level and so on). In our case, this project aims at an imaging system ranging from 400 nm to 700 nm under room condition, which gives a typical design configuration. A rough design from the sketch is dealt with multiple optical parameters for the reason that a complex system commonly is assembled by several optics elements and each element involves a set of defined parameters i.e. radii of curvature, thickness, refractive index and aperture size. Meanwhile, cemented or airspaced position of several adjacent lenses generates many combinations as a lens group, which makes the system design more complicated. To efficiently manipulate the optics parameters to achieve the final goal, a design procedure therefore has to be followed up to guide experienced optics designers especially beginners and the procedure is presented as a flow chart in Fig. 3.1 which illustrates a design cycle of optical system in 4 stages.

1. Pre-definition of system parameters:

   System configuration describes the basic form of an optical system. It consists of the number of optical elements and the distribution of those elements such as optical power, airspace and relative position. A sketch of the targeted system commonly

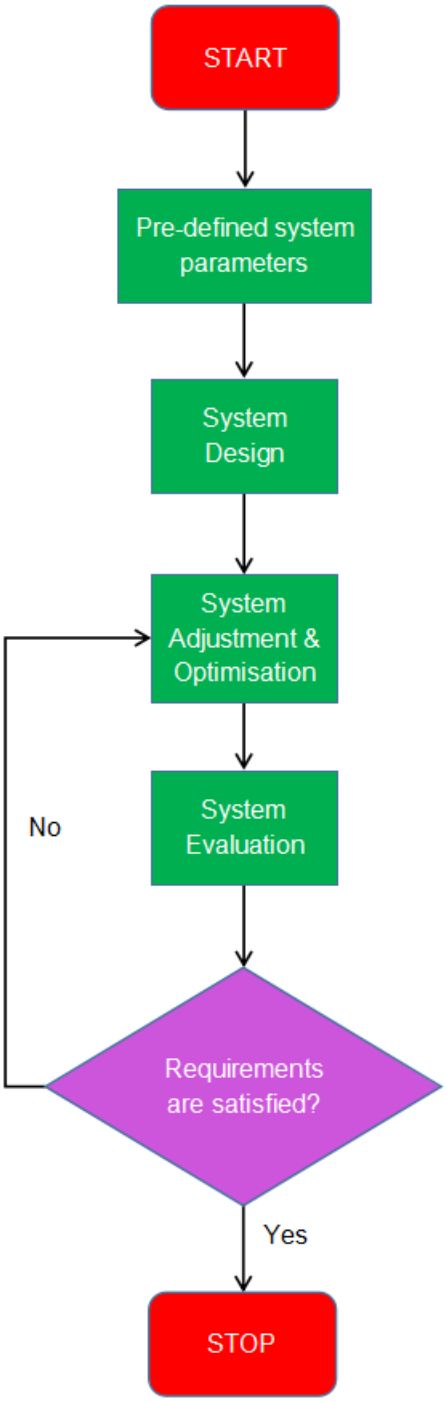

Figure 3.1: Optical design flow chart contains four main stage: pre-definition of system parameters, system design, system adjustment & optimisation and system evaluation.

starts with some widely-used configurations with either purchased or open file information from patents and database as a starting point prior to design stage. This provides a convenient start point close to the basic requirements in terms of spectral

range, focal length, F-number, field of view, image resolution and so on for further modification.

Concretely, it is clear to understand that one imaging system is to correspond one real point on object with one real point on image on focus. Extend both points to the space where either of them stays and we can define the object space and the image space to analyse the situation how rays propagates through the system and the performance at detector. Focal length is a prior parameter to describe the distance from where the focal point of incoming rays is on image space to the entrance pupil at which the parallel rays from object space enters. The entrance pupil is a clear aperture to the system which determines the amount of light goes into the system. The F-number, defined as the ratio of focal length to the clear aperture diameter, more technologically describes the light throughput of lens system. Another factor to be considered is size of detector with pixel pitch which critically allows how big the captured image can be. This is mutually determined by field of view corresponding to angular resolution and image height corresponding to spatial resolution. It often needs to consider the actual limitation of detector manufacturing although the detector specifications can be varied by simulating in optical software which accords to imaging optics. Besides that, classic lens combinations such as singlet, doublet and triplet are mostly used in preliminary configuration, which would be easy to be manipulated later on, including adjustment of lens number and material kinds at next stage.

It is also noted that the calculation of those aforementioned parameters are based upon thin-lens theory which assumes the lens has no thickness in an ideal situation when the system is analysed using ray tracing at this stage. This simplicity too commonly adopts few optical components to basically satisfy the requirements instead of starting with a complex multiple-lens system. The configuration complies to those parameters in a way that all optics in the system are perfect and free from any aberration, which leads to the calculation of ray trajectory following the

trigonometry with the slope of angles to the optical axis and angles of incidence and refraction to the lens surfaces. During this calculation, those parameters have a relationship with the slope, the angles and the ray height at each surface as the first-order expression, which calls first-order parameters [4]. In the meantime, it brings in an infinitesimal region where the rays are so close to the axis so that the angles are set equal to their sine and tangent. Such infinitesimal region is known as *Paraxial Region*, mathematically defined as

$$\sin\,\theta \approx \theta, \tan\,\theta \approx \theta, \tag{3.1}$$

where θ denotes the angle of incidence or refraction. Based upon the above conditions, the paraxial approximation becomes utterly fast to determine the configuration with the Snell's law [4]. Since the paraxial approximation gives the exact location of a perfect focal point for the aberration-free configuration, it can be further regarded as a comparison to show how far the actual ray trajectory deviates from the ideal location.

2. System design:

   Following the start point built up at previous stage, biggest challenge during the translation from the paraxial approximation to the practical configuration in software is the existence of curvature and thickness of each one of optical components which result in aberrations due to the fact that the refraction and reflection varied with spectral wavelength and the angle of incidence are capable of causing deviations of ray height at image space from the ideal image.

   Aberrations are the main concern to optical system design. There are two kinds of aberrations dependant on the spectra. The monochromatic aberration or so-called *Seidel Aberration* is a set of 5 primary aberrations expressed as five third-order coefficients in an aberration polynomial. The aberration polynomial is derived by the pupil coordinates (x,y) and object coordinates (h_x,h_y) of a ray throughout a

rotation-invariant system. Since the system has rotational symmetry, the aberration polynomial in meridional plane can be presented in the polar coordinate (h, ρ, θ) [128] as

$$\varepsilon = \sigma_1 \rho^3 \cos\theta + \sigma_2 (2 + \cos 2\theta) \rho^2 h + (3\sigma_3 + \sigma_4) \rho h^2 \cos\theta + \sigma_5 h^3, \quad (3.2)$$

where the third order comes from the sum of powers of ρ and h. The coefficient indices σ denote Spherical Aberration (σ_1), Coma (σ_2), Astigmatism (σ_3 and σ_4), Petzval Curvature (σ_3 and σ_4) and Distortion (σ_5), as vividly shown in Fig. 3.2.

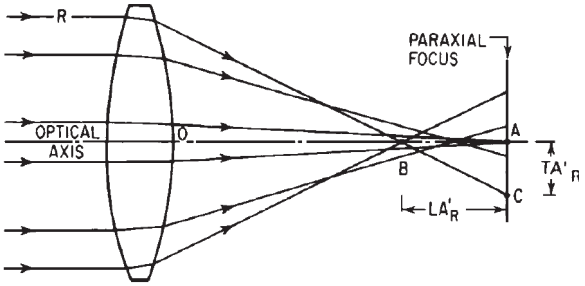

(a) Spherical aberration: longitudinal spherical aberration and transverse spherical aberration.

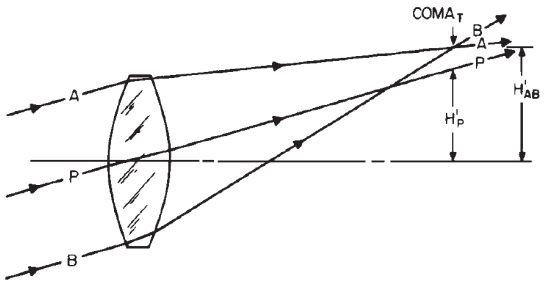

(b) Coma: tangential coma and sagittal coma.

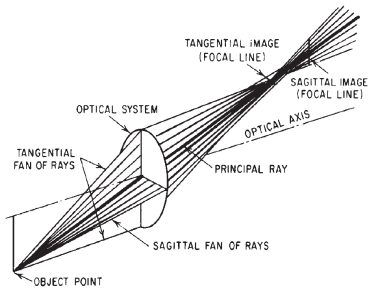

(c) Astigmatism: tangetial astigmatism and sagittal astigmatism.

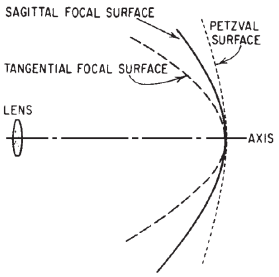

(d) Petzval curvature: sagittal curvature and tangential curvature.

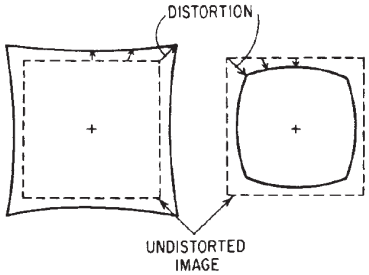

(e) Distortion: pincushion distortion and barrel distortion.

Figure 3.2: Five primary aberrations of Seidel Aberration from [4] are clearly demonstrated using ray tracing.

Spherical aberration is due to the focal distance of the ray intersection on axis are varied with the ray height through the lens, which causes multiple focus points rather than a perfect point at paraxial focus. The spherical aberration consists of two types, longitudinal and transverse deviation referred to the horizontal and vertical direction along the axis. Coma describes a non-uniform magnified pattern or coma patch at off-axis position for oblique incident rays due to the unbalanced magnification capability at central region and edge of lens. The coma can be defined into two types, tangential coma by the axial direction of rays and sagittal coma by the sagittal direction of rays. Extending the concept of coma, two perpendicular planes (tangential and sagittal planes) of the incident rays in object space form one-line focal image in image space where tangential image lies in sagittal plane and sagittal image lies in tangential plane. When those two images do not intersect with each other, the astigmatism occurs. With the position of off-axis points moving further away from the axis, the astigmatism appears severer. When the astigmatism exists in the system, Petzval Curvature will be formed by all the images of the axial and sagittal points due to the field curvature of lens itself. Distortion shows how far the displacement of actual image is away from the paraxial image. The edge of the image commonly presents more displacement than the central region due to the curvature of lens, especially when a lens with strong optical power is used. This causes expanded image which is called pincushion distortion and pull-inward image which is called barrel distortion. Chromatic aberration is due to the lens has wavelength-dependant refraction characteristics, which causes multiple focal points to each of wavelengths. Similar to spherical aberration, chromatic aberration occurs in longitudinal and transverse direction. It needs to be particularly taken into account during designing a dispersive system in our case.

To counter the aberrations at this stage, it usually adopts one or lens combinations with positive aberration or negative aberration to balance the total aberration of system. The design of those lens combinations can be achieved by splitting one

thick lens into two or more lenses, then manipulating curvatures and glass materials to realise the aberration balancing in optical software.

3. System adjustment and optimisation

System design stage is to adjust major part of the preliminary configuration to close the paraxial approximation and then try to reduce or eliminate the aberration, while, at this stage, the system will be slightly adjusted to achieve the improvement of performance in an optimal version of the optical system. This is realised through built-in optimisation functions in optical software where users can define the number and the type of parameters as input variables to construct a weighted sum of squares of those parameters of error function. The error function calculates the difference between the current optical system and the ideal system with required conditions. It then is run by optimisation algorithm to find out a suitable minimum. Particularly, in the optimisation of optical system's error function, the dimensionality of inputs is relatively high and the number of local minima is often large [128], which leads to difficulty in finding the global minimum. It therefore is of importance to depend on experience to choose a suitable start point for the seek of a closer local minimum.

Damped least squares (DLS) is a standard optimisation algorithm widely used in most optical software. In DLS, first of all, the error function constructed in a form of a weighted sum of variables has a representation as

$$\phi(\mathbf{x}) = \sum_{i=1}^{n} w_i f_i^2(\mathbf{x}), \tag{3.3}$$

where $\mathbf{x}$ represents a set of optimisation variables and the f represents operands which are defined by the users to do one kind of math conditions such as addition, subtraction, great than or less than and multiplication between any two inputs. Usually the former input is assigned to the actual value of optical parameters and the latter one is assigned to the target value. The weight w is to adjust the relative importance of the parameters to be optimised. The optimisation is based on iteration

of the error function by changing the operands as

$$f_i(x_i + \Delta x_j) = f_i(x_j) + \frac{\partial f_i}{\partial x_j}\Delta x_j \tag{3.4}$$

where it represents the change happens in i^{th} operand with a change in j^{th} variable. In a real situation of optical design, there may be no solution to reduce f_i to zero due to physical condition in optics. It therefore turns to find a least-squares solution for Δx_j to have a minimal operand. In order to achieve that, it introduces a partial derivative matrix $\mathbf{A}$ to the multi-variable function $\mathbf{f}$ as

$$\mathbf{A}\Delta\mathbf{x} = -\mathbf{f}. \tag{3.5}$$

The lease squares algorithm iterates $\mathbf{x}_k$ with the initial value $\mathbf{x}_0$ by solving the following linear equation to update $\mathbf{x}_k$ with $\mathbf{x}_{k+1} = \mathbf{x}_{k+1} + \Delta\mathbf{x}_k$,

$$\mathbf{A}_k^T\mathbf{A}_k\Delta\mathbf{x}_k = -\mathbf{A}_k^T\mathbf{f}_k. \tag{3.6}$$

To avoid the divergence of the Δx especially for a nonlinear system, the solution becomes a damped least squares equation by adding a damping term μ as

$$(\mathbf{A}_k^T\mathbf{A}_k + \mu_k\mathbf{I})\Delta\mathbf{x}_k = -\mathbf{A}_k^T\mathbf{f}_k \tag{3.7}$$

where I is the identity matrix. The point of adding the damping term is to stabilise the least squares equation by reducing the magnitude of the change vector $\Delta\mathbf{x}$. It is crucial to know which value of the damping term to be selected. In OSLO, there is an algorithm for automatically choosing the damping term [128]. It initialises the starting value, normally set to 10^{-8}. The algorithm uses large step to increase the damping over the optimum and then decreases it using the scaling factor α until it finds the optimum.

4. System evaluation

   Several items or evaluation functions such as *Spot Diagram*, *Point Spread Function* and *Modulation Transfer Function* established for quantitative measurement of optical performance are used to evaluate whether the system reaches the requirements or not. Those evaluation functions are distinguishable from the pre-defined requirements in paraxial approximation, because the requirements in the initial stage are mainly first-order parameters which can be calculated by only tracing a few important rays, for example marginal ray that pass through the edge of aperture pupil to define aperture diameter and chief ray that pass through the centre of aperture pupil to find location of aperture. As for the evaluation functions, there may use a large amount of rays to observe some 2D or 3D diagram. Spot diagram is a resulting ray data diagram from tracing a ray bundle from a single object point through the aperture. The diagram shows the geometric distribution of the rays as "spot" to illustrate how distorted the image could be or aberration situation. The number of rays for tracing will be determined by the number of aperture divisions on a virtual grid pattern which uniformly divides the entrance pupil. It usually comes with the Airy disk as a black circle to check spot size and location of shifted focal point. In our case, the spot diagram is of great importance to use for the location of monochromatic wavelength and its spot size since our to-be-designed system is a multispectral dispersive imager.

3.2 OSLO Environment

The OSLO program provides an interactive environment for users to conveniently adjust parameters for system design and interactively feedback the corresponding results in 3D visual graphs and specific quantitative changes in printed text [129]. Basic configuration of OSLO can be segmented into three sections as the screen shot of overview in Fig. 3.3: (1) Command window, the main window for users to interactively process exe-

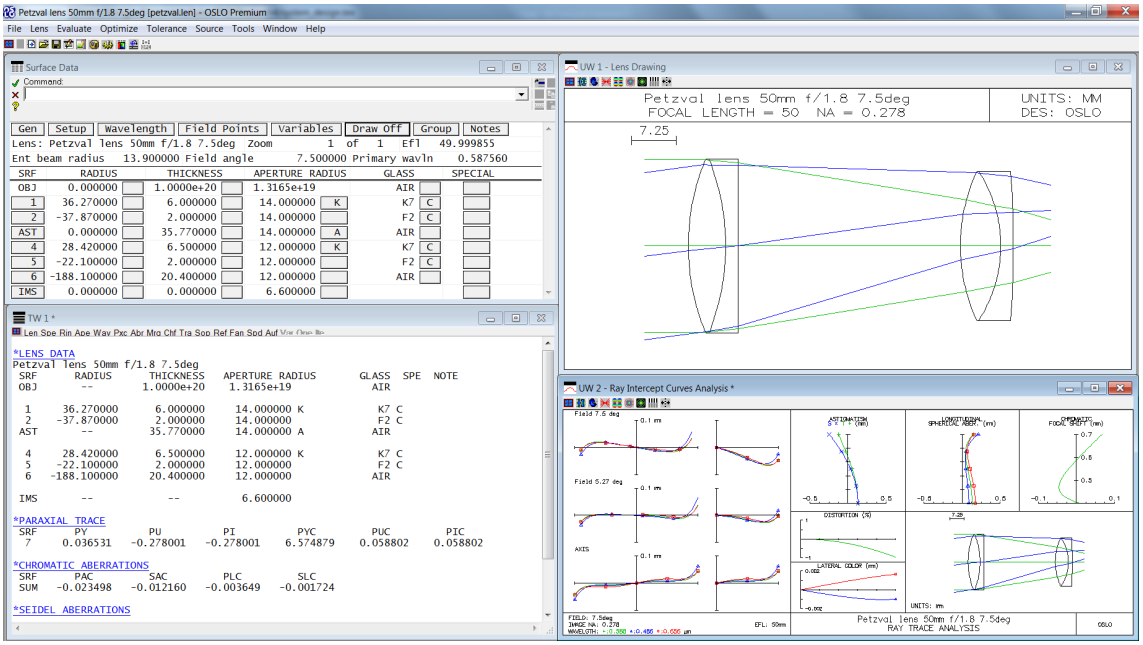

Figure 3.3: Screenshot of configuration of OSLO software showing main windows for users to interact with the program.

cutable commands and display system configuration in spreadsheet mode, including four main categories of system (surface radius, thickness, aperture radius and glass materials), first-order parameters (Effective Focal Length, Numerical Aperture, Working F-number, Field Angle and Wavelengths) and other supportive data. (2) Graphic window, mainly displays system sketch with marginal rays and chief rays interacted with in 3D visualisation. This window can be extendible to many parallel windows to visually demonstrate evaluation function and relevant diagrams such as Modulation Transfer Function (MTF), Spot Diagram, Ray Intercept Curves Analysis and so on. (3) Text window, an output window feedbacks numerical parameters of system displayed in text format and the output is stored in a spreadsheet buffer owned by Text window in case users want to read out or access in any time. Apart from interactive windows, the OSLO® also provides a feature that allows users to build their own executing commands to access specific parameter, invoke built-in functions or construct custom evaluation functions to optimise system, rather than relying on limited built-in functions, by using macro language CCL [128, 129], similar to C language.

3.3 Resolution

Generally, designing target for any optical imaging system is to achieve a diffraction-limited imaging system, which can focus a clear spot free from any aberration to a point light source. For example, for a diffraction-limited imaging system with a circular aperture, a perfect point source will form a concentric bright spot surrounded by a series of degrading bright and black rings on the image plane far away from the aperture, which is due to Fraunhofer diffraction [130]. The diffraction pattern, also called Airy Disk [130], to the point source as an impulse function is actually the impulse response of the system. Such function of Airy Disk in spatial domain is terminologically defined as the Point Spread Function (PSF). Since the concentric spot takes a large amount of energy compared to the rest bright rings, the small area of that bright spot whose boundary is defined by the first dark ring can be regarded as the image of the point light source, the radius of which is mathematically represented as

$$r = \frac{1.22\lambda L}{D}, \tag{3.8}$$

where λ is the wavelength of the light source, D is the effective aperture diameter and L is the distance between the aperture and the image plane. Especially, when the spot on image plane is at focus the distance becomes the focal length, which means

$$r = \frac{1.22\lambda f}{D} = 1.22\lambda \cdot F/\#, \tag{3.9}$$

where $F/\# = f/D$ denotes the F-number which is an useful terminology for optical system design and further calculation. This radius r is more importantly defined by Lord Rayleigh as the minimal resolvable distance Δl to distinguish two projected spots on image plane, where one's centre is right at the location of the other's first dark ring.

Resolution, therefore, can be determined through the above equations as the first step to design an imaging system.

3.3.1 Modulation Transfer Function

The Modulation Transfer Function (MTF) [130] physically describes how well an optical system resolves a series of sinusoids of spatial frequencies with input 100% ratio defined as

$$MTF = \frac{Am_{max} - Am_{min}}{Am_{max} + Am_{min}}, \tag{3.10}$$

where Am_{max} denotes maximum amplitude of a sinusoid at a certain spatial frequency and Am_{min} denotes minimum amplitude of the sinusoid. This only involves the irradiance in greyscale, rather than monochromatic or chromatic optical characteristics, from an input of periodic line pairs with only bright part and dark part. To a diffraction-limit system, ideally it could resolve Am_{max} and Am_{min} correctly at 100%, which means dark part is as relatively small as zero to bright part. However, it is nearly impossible to achieve an aberration-free system in reality. As a consequence, the bright and dark parts could get distorted to be expressed as their original values, which cause MTF less than 100%. Multiple MTF values can be collected to plot a curve as a function of spatial frequencies, resulting in a critical measurement to indicate optical system's quality.

To be more explicit, the MTF curve is mathematically computed as the magnitude of Optical Transfer Function (OTF), which describes the Fourier Transform of PSF in spatial frequency domain, given as [131]

$$MTF(f_y) = \frac{2}{\pi}\left[cos^{-1}\left(\frac{f_y}{f_c}\right) + \frac{f_y}{f_c}\sqrt{1-\left(\frac{f_y}{f_c}\right)^2}\right], \tag{3.11}$$

where f_y denotes the current spatial frequency and f_c denotes the cut-off spatial frequency, mathematically defined as

$$f_c = \frac{2NA}{\lambda}, \tag{3.12}$$

where NA denotes the numerical aperture. Numerical aperture is determined by system FoV. The value of the numerical aperture is defined at pre-design stage by system requirement. Once numerical aperture is set according to the system pre-design, the cut-off

spatial frequency can be found out corresponding to the required wavelength and applied back to Eq. (3.11). Therefore, the spatial frequency to reach 50% MTF can be calculated through Eq. (3.11) accordingly.

3.3.2 Dispersion

To the targeted CASSI framework as a dispersive system, spectral wavelength is more concerned with system design. Resolving the spectral wavelengths is dependent on *Prism* used in most of CASSI systems. Glass material not only for the prism but also for other optical components described in *Abbe Number* [130], or called V number which is used to describe the dispersion ability. Commonly it can be defined in V_d by

$$V_d = \frac{n_d - 1}{n_F - n_C} \tag{3.13}$$

where three refractive indices n_d, n_F and n_C represent the refractive value at three specific wavelengths, that are the helium d line (587.6 nm), the hydrogen F line (486.1 nm) and the hydrogen C line (656.3 nm). In OSLO, in order to flexibly use V number in accordance with the design purpose of specific spectral region, the equation of V number is dynamically related to top three wavelengths in the program. Wavelength 1 denotes the primary wavelength mainly used to determine focal length or F-number of system, the refractive index of which is associated with n_d. Wavelength 2 denotes the shortest wavelength associated with n_F and Wavelength 3 denotes the longest wavelength associated with n_C. All the system evaluation functions in the following sections will be associated with these three wavelengths only.

3.4 Geometrical Structure Design

A typical imaging system is comprised of an objective lens, several relay lenses, an eyepiece lens, optional reflective or dispersive elements and detector. Unlike such visual sys-

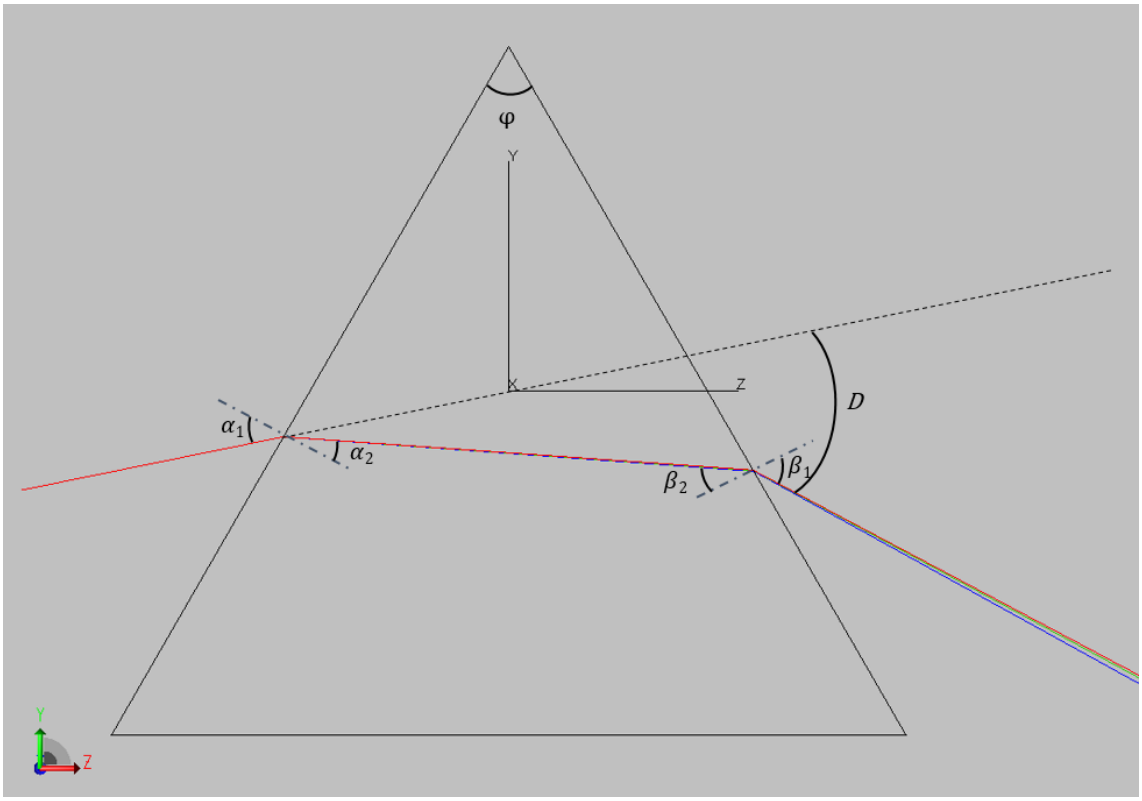

Figure 3.4: Rays propagation in dispersive equilateral prism is simulated in TracePro to demonstrate the singe prism dispersion.

tems as the telescope and microscope, the CASSI includes dispersive element e.g. prism or diffractive grating essentially while eyepiece lens is not necessary as such imager does not serve the naked eyes.

3.4.1 Single-Prism System Design

Single-Prism CASSI [60] utilises a simple structure that an objective lens forms incident rays from the scene onto a coded aperture mask, an equilateral prism being placed right after to provide dispersion and a detector receive the final image with front relay lens to bridge the rays from the mask to the prism and back relay lens to bridge the dispersed rays from the prism to the detector. This experimental work has been done with the off-the-shelf optics by A. Wagadarikar [60].

As the core element in the system, the equilateral prism generates a typical dispersion when a bundle of rays strikes front surface at an incident angle α_1, as shown in Fig. 3.4.

Light propagation during the dispersion encounters the refraction twice, which causes angular deviation $(\alpha_1 - \alpha_2)$ at front surface and $(\beta_1 - \beta_2)$ at rear surface. The total angular deviation, therefore, can sum up as

$$D = (\alpha_1 - \alpha_2) + (\beta_1 - \beta_2). \tag{3.14}$$

Given the fact that the vertex angle of the prism $\varphi = \alpha_2 + \beta_2$, Eq. (3.14) can be written as

$$D = \alpha_1 + \beta_1 - \varphi, \tag{3.15}$$

where the unknown angle β_1, due to the refraction, can be computed further by applying Snell's law as follows,

$$\sin\beta_1 = n\sin\beta_2, \tag{3.16}$$

$$\beta_2 = \varphi - \alpha_2, \tag{3.17}$$

$$\sin\alpha_2 = \frac{1}{n}\sin\alpha_1. \tag{3.18}$$

Therefore, combining all the aforementioned equations, the total angular deviation of the equilateral prism, only based on the incoming ray's incident angle α_1 and the refractive index corresponding to its wavelength, can be represented as

$$D = \alpha_1 - \varphi + \arcsin\left[\sin\varphi\sqrt{n(\lambda)^2 - \sin^2\alpha_1} - \cos\varphi\sin\alpha_1\right], \tag{3.19}$$

particularly, the refractive index of prism will be explained in Sellmeier formula [128] throughout the entire thesis for system design and dispersion calculation as

$$n^2(\lambda) = 1.0 + \frac{b_1\lambda^2}{\lambda^2 - c_1} + \frac{b_2\lambda^2}{\lambda^2 - c_2} + \frac{b_3\lambda^2}{\lambda^2 - c_3}, \tag{3.20}$$

where λ is the wavelength in µm. b_1, b_2, b_3 and c_1, c_2, c_3 are the glass materials' coefficients. This is also adopted by optical materials library in OSLO, which is widely

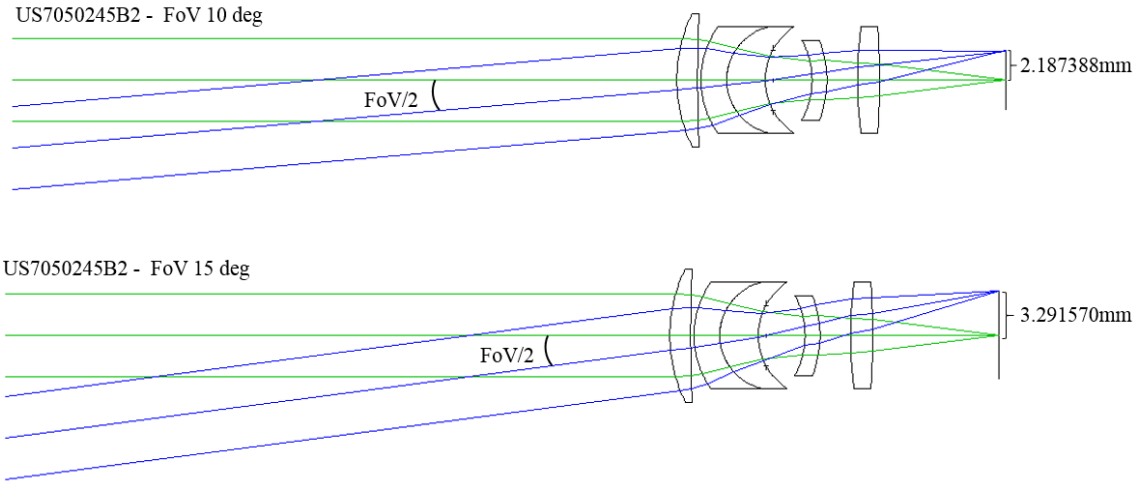

Figure 3.5: Change of image height associated with tilted FoV set in an example of US7050245B2 with two FoV: 10° and 15°.

used by Schott AG and other glass manufacturers. According to the above equation of total angular deviation, the monochromatic angular deviation could be computed. With the wavelength decreasing, it is noticed that the deviated angle becomes large. Relative angular deviation at a certain range of the wavelength of incoming rays changes from zero to a scope that is bound to shortest wavelength and longest wavelength, as follows

$$D_{long} = \alpha_1 - \varphi + \arcsin\left[\sin\varphi\sqrt{n(\lambda_{long})^2 - \sin^2\alpha_1} - \cos\varphi\sin\alpha_1\right], \tag{3.21}$$

$$D_{short} = \alpha_1 - \varphi + \arcsin\left[\sin\varphi\sqrt{n(\lambda_{short})^2 - \sin^2\alpha_1} - \cos\varphi\sin\alpha_1\right], \tag{3.22}$$

$$D_{scope} = D_{short} - D_{long}, \tag{3.23}$$

where D_{long} denotes the angular deviation at longest wavelength of incident rays, D_{short} denotes the angular deviation at shortest wavelength of incident rays. So D_{scope} denotes the angular range between short wavelength and long wavelength, which is the key to the associated dispersion displacement at final image plane.

The scope of total angular deviation from emergent rays too defines field angle of back relay lens, which is associated with the image height formed on image plane. Likewise, the incident angle at front surface of the prism is associated with the object height on object plane of front relay lens. Fig. 3.5 shows the corresponding image height in the

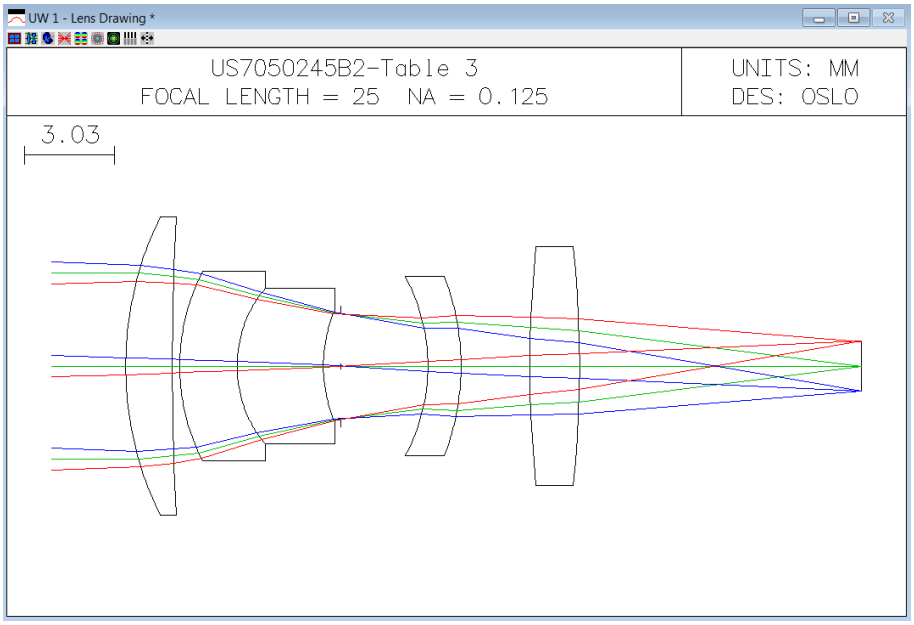

Figure 3.6: Modified imaging lens F/4, focal length 25 mm showing propagation of marginal rays and chief rays to demonstrate the full field angle of the system.

patent US7050245B2 [132] by setting FoV 10° and 15° at 587.56 nm. This imaging lens assembly has 25 mm focal length and accepts a full field of view of 15° with 0% vignetting and less than 1% distortion. By modifying this patent to be used in SP-CASSI as shown in Fig. 3.6, collimated beams emit from infinity and propagate from left to right. Particularly, green rays represent the on-axis rays and focus at axis point at image plane and blue rays represent the off-axis rays at a defined FoV and reach an off-axis point at image plane. The relationship between FoV and location at image plane can be computed by using paraxial approximation, which commonly adopts half FoV as

$$\tan(FoV/2) = \frac{Image\ height}{EFL}, \tag{3.24}$$

where *EFL* denotes *Effective Focal Length*, which means the distance from focal plane to *Rear Principal Plane*. Through this equation, linear displacement of chromatic wavelengths at image plane is only determined by non-linearly choosing FoV, when *EFL* is fixed.

As detector pixel pitch refers to smallest feature of our laboratory sensor 6.5 µm , the

resolution Δx, according to Sec. 3.3, applies Nyquist sampling $\frac{1}{2}$ *lp/mm per pixel*, as

$$Resolution = \frac{1}{2 \times 0.0065\ mm} = 76.92\ lp/mm. \tag{3.25}$$

System F-number at such resolution can be computed in Eq. (3.9) to obtain a minimum F-number (at longest wavelength 700 nm when visible spectrum from 400 nm to 700 nm is considered: $\frac{1}{1.22 \cdot 700nm \cdot 76.92lp/mm} = F/15$ to reach MTF 9% Rayleigh criterion. While, in further simulations, the smallest feature of coded aperture is considered to be 2× sensor pitch and the spectral range is set from 450 nm to 650 nm to compare the performance of different optical systems under the same condition. Therefore, the sensor resolution can be less rigorous so that it reaches $\frac{1}{2 \times 2 \times 0.0065\ mm} = 38.46\ lp/mm$. Consequently, the requirement of the minimal system F-number to serve new spectral range at Rayleigh criterion, becomes F/32 at 650 nm.

Based upon that, continue applying those parameters in Eq. (3.11) and Eq. (3.12) and

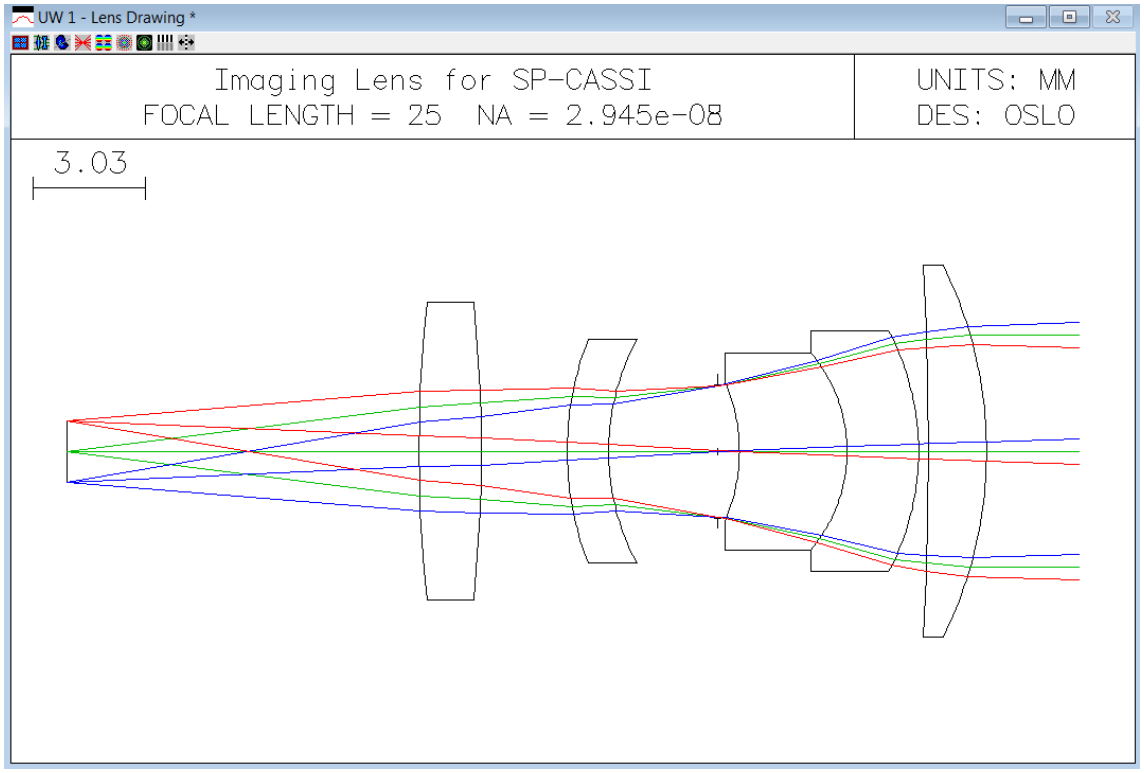

Figure 3.7: Imaging lens F/4, focal length 25 mm, Object Numerical Aperture 0.125 for SP-CASSI, emitting from the full field points and axial point.

then the system is required to obtain an F/16 to achieve the spatial frequency 38.46 *lp/mm* @ MTF 50% 650 nm. The previous example US7050245B2, therefore, must maintain a clear aperture of above $D = \frac{25mm}{\mathrm{F}/16} = 1.56mm$, which is also the diameter of *Entrance Pupil*. The entrance pupil is the virtual image of *Aperture Stop* formed by all the optics before the aperture stop. By controlling the radius of the physical aperture stop, this first-order parameter can adjust the amount of incident rays into the system. To ensure the entrance pupil large enough to collect the rays across 450 nm-650 nm, the radius of the entrance pupil is set to 3.125 mm in paraxial approximation when the system F-number is F/4, numerical aperture 0.125 and aperture radius 1.765 mm accordingly. The patent US7050245B2, therefore, is adjusted to satisfy F/4 requirements as shown in Fig. 3.7. The figure shows that the imaging lens is reversed placed after the object plane on the left hand where the location of the coded aperture is. The focused image through the coded aperture would become collimated and propagate towards the next component when it propagates from the left to the right throughout the imaging lens. The colour rays in the figure only distinguish their location of the coded aperture while the central wavelength 587.56 nm was the one used for demonstration. Before the imaging lens is integrated with other SP-CASSI components, as a single lens itself, Fig. 3.8 shows monochromatic MTF diagrams at primary wavelength 587.56 nm, second wavelength 450 nm and third wavelength 650 nm when Field Points are set at On-Axis (0°), 1.334° (0.707 ratio of half FoV) and 1.906° (half FoV), corresponding to object height 0 mm, 0.582 mm and 0.832 mm. There are 7 curves in every single diagram, including MTF on tangential (as symbol **T**) and sagittal (as symbol **S**) direction plus the ideal diffraction-limited curve. The T line and S line not only show how good from the ideal condition the contrast along both directions, but also the relative position between T line and S line characterises the situation of optical phase (e.g. phase reversal). However, in this case, the overall performance behaves very well, wherein the cut-off spatial frequency in all three diagrams is above 300 *lp/mm*, MTF at 50% reaches 120 *lp/mm* at 587.56 mm, 200 *lp/mm* at 450 mm and 150 *lp/mm* at 650 mm, the variance between T line and S line are almost zero at 650 nm

while in primary wavelength and second wavelength there is a subtle variance, which could not affect the system. 2D spot diagrams in Fig. 3.9 shows the spatial distribution

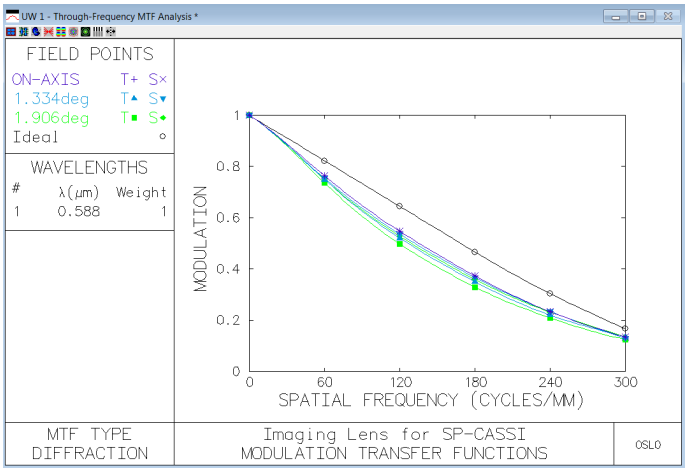

(a) Primary wavelength 587.56 nm

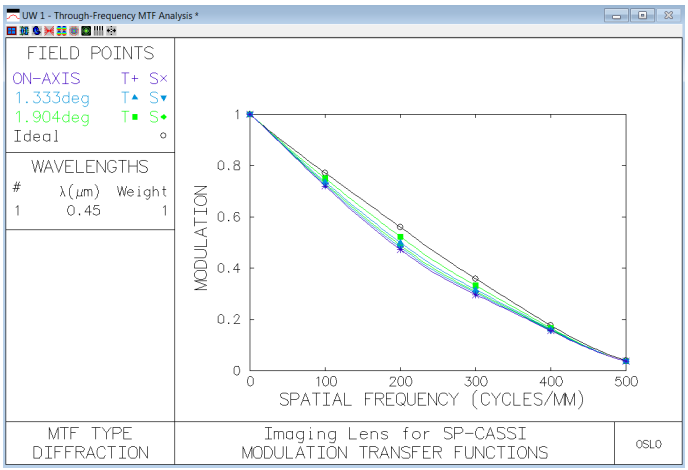

(b) Second wavelength 450 nm

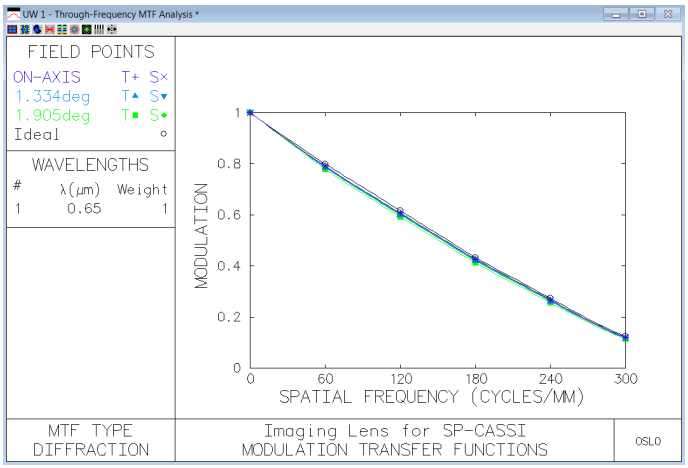

(c) Third wavelength 650 nm

Figure 3.8: MTF diagrams for imaging lens used in SP-CASSI.

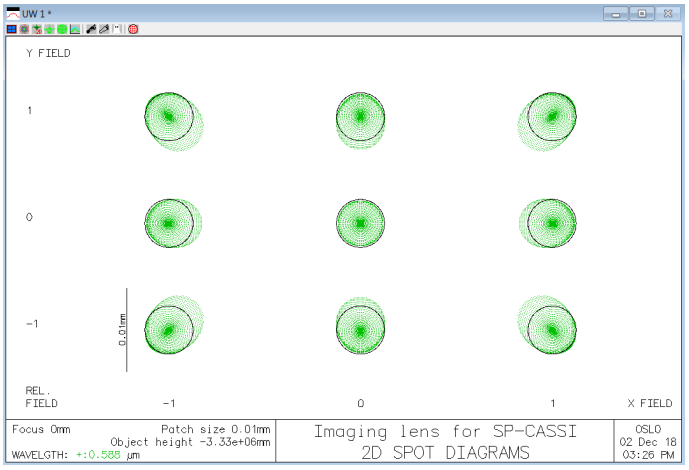

(a) Primary wavelength 587.56 nm

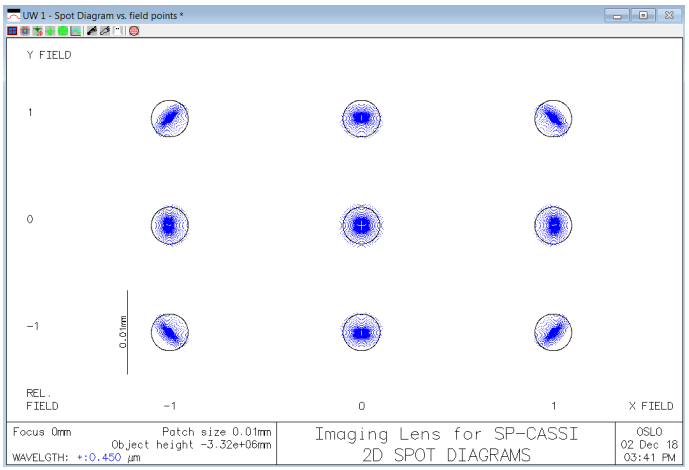

(b) Second wavelength 450 nm

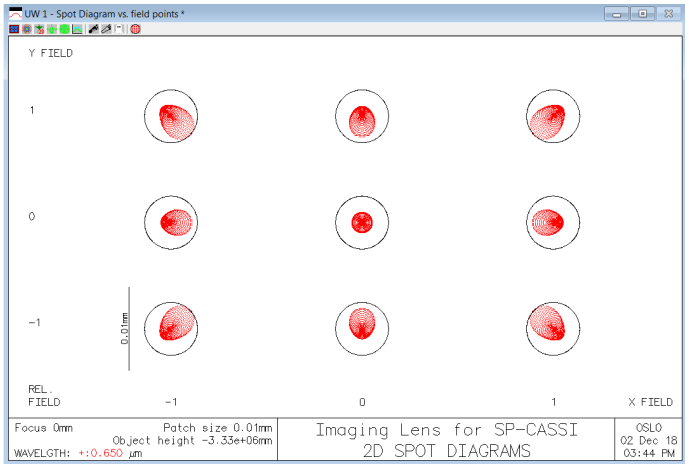

(c) Third wavelength 650 nm

Figure 3.9: Spot diagrams of imaging lens for SP-CASSI.

of rays through all over the aperture pupil with respect to 9 field points symmetrically set at image. It illustrates the quality of the lens by focusing a circular spot. Fig. 3.9a shows

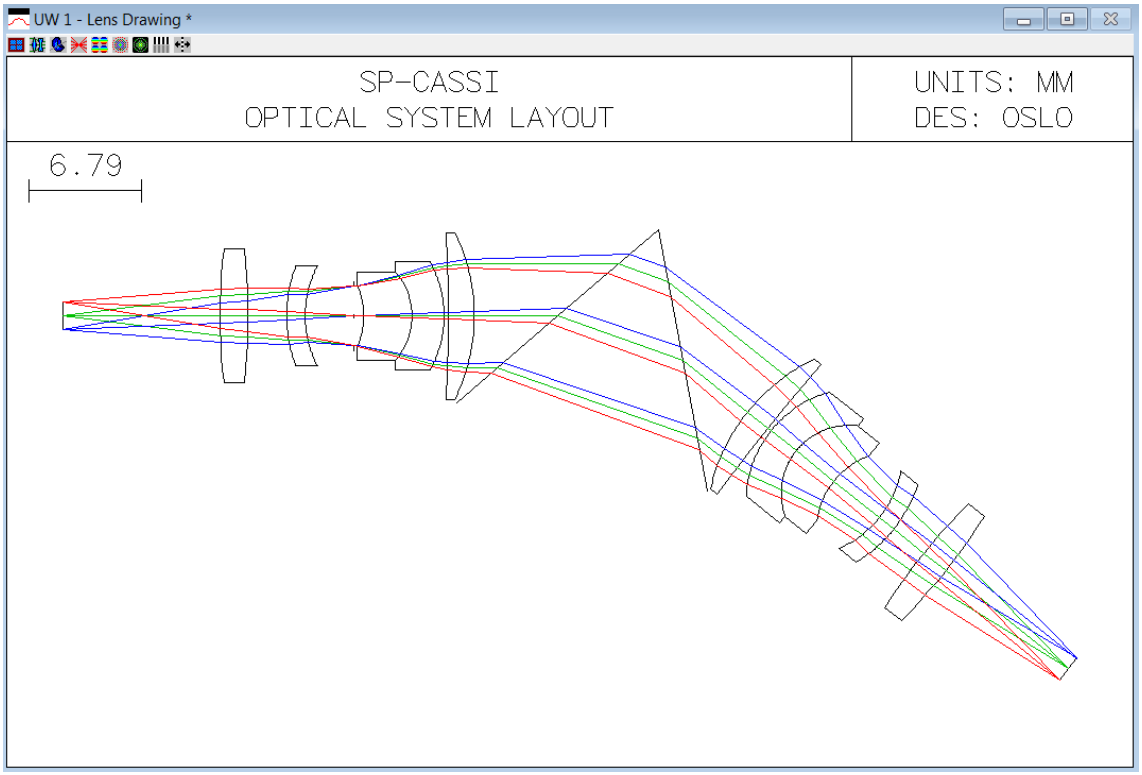

Figure 3.10: Rays propagation in imaging lenses and equilateral prism, the main part of the SP-CASSI, emitting from full field points and axial point through the full clear aperture of system.

the spots at 9 directions are in a well circular shape. Although the spots at four corners have subtle coma aberration which is out of the black circle (the Airy Disk), most of them are still centralised within the Airy Disk. The spots at third wavelength all stay within the Airy Disk and will be regarded as a perfect spot, despite that the coma aberration of those points at edge is more severer apart from the central point. Same situation happens in the spot diagram at second wavelength, except that it also suffers from spherical aberration. To be summarised, this imaging lens is able to be integrated to the system at next stage.

3.4.1.1 System Assembly

As described before, two imaging lenses and one prism are used to assemble the main part of SP-CASSI. Considering that the prism has to cover a full field angle 1.906° at which the exiting rays from the imaging lens, the imaging lens either at front or at back was placed at 5 mm distance from the prism with 16 mm long. Particularly, the exiting rays

after the prism could exceed the field angle and then we slightly expanded the aperture radius of the back imaging lens due to the angular deviation, which accommodates all the bands across 450 mm to 650 mm, especially for the off-axis rays at 450 nm and 650 mm. Rotation angle of equilateral prism is associated to the dispersion capability of SP-CASSI, which is set to 49.45° to balance the distortion to individual bands caused by the prism and will be explained in the following section. Therefore, the combination of imaging lenses and the prism is displayed in Fig. 3.10, where three colours of ray, red, green and blue, indicate location at top, on-axis and bottom of object in order. At each location, three emitting rays at central wavelength 587.56 nm which covers the full pupil of system aperture with object NA 0.125, propagate through the system and strike final image plane at focus with an inverted image as the magnification of this system is -1.

The monochromatic MTF diagrams after assembling the system, shown in Fig. 3.11, can be seen that the overall MTF is not as good as MTF diagrams of single imaging lens present in Fig. 3.8, which is due to that more optics, especially the prism was brought in and degraded the image quality. Concretely, Fig. 3.11a shows the central wavelength 587.56 nm behaves even better than the result of single imaging lens. Even though the original optical axis was bended by the prism, the back imaging lens was still aligned with the bended axis by tilting the deviated angle at 587.56 mm. Due to that, the back imaging lens in fact was mirror-symmetrically placed to the front imaging lens, aside the prism as the centre, which enhanced the image quality at the final image plane. For the wavelength 450 mm in Fig. 3.11b, its MTF drops dramatically from 50% at 40 *lp/mm* to 10% at 80 *lp/mm* and remains less than 10% till 200 *lp/mm*, wherein the tangential line at -0.832 mm crosses other lines once at the region of 80 *lp/mm* to 120 *lp/mm*, which indicates the phase of spatial line pairs is inverted at that region. Such decline from 200 *lp/mm* in Fig. 3.8b to the current 40 *lp/mm* is mainly due to the strong bending effect to the short wavelength from the equilateral. However, this would not cause image quality insignificantly to be identified at 450 nm since MTF 50% at 40 *lp/mm* can satisfy the resolution. The wavelength 650 in Fig. 3.12c has MTF 50% at around 80 *lp/mm* and

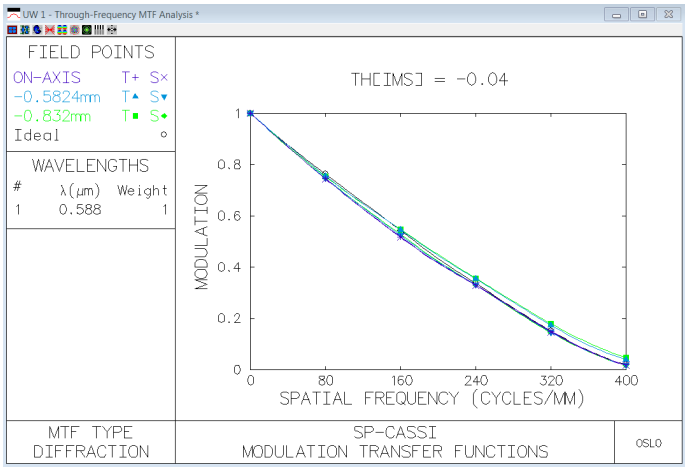

(a) Primary wavelength 587.56 nm

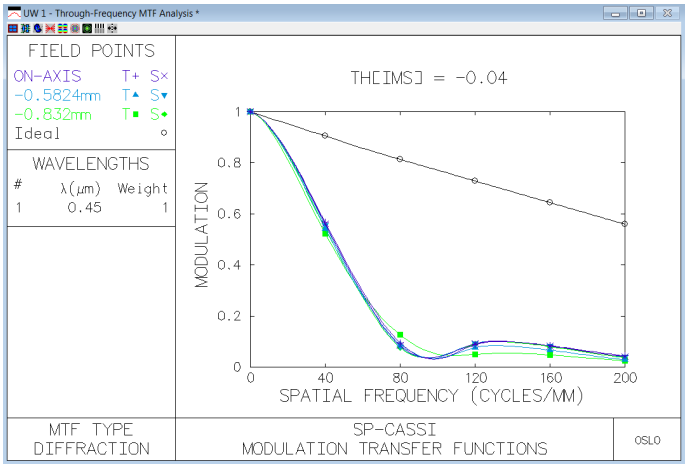

(b) Second wavelength 450 nm

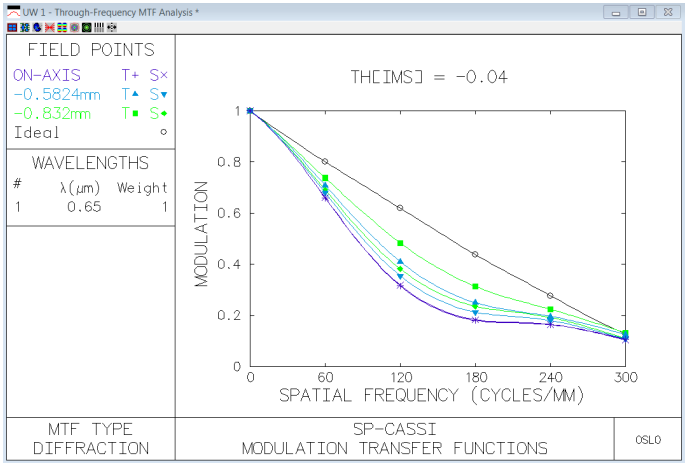

(c) Third wavelength 650 nm

Figure 3.11: MTF diagrams of imaging lens used in SP-CASSI.

smoothly drops to 20% at 180 *lp/mm*.

Spot diagram in Fig. 3.12 shows the system suffers mainly from SA and CA, partic-

(a) Primary wavelength 587.56 nm

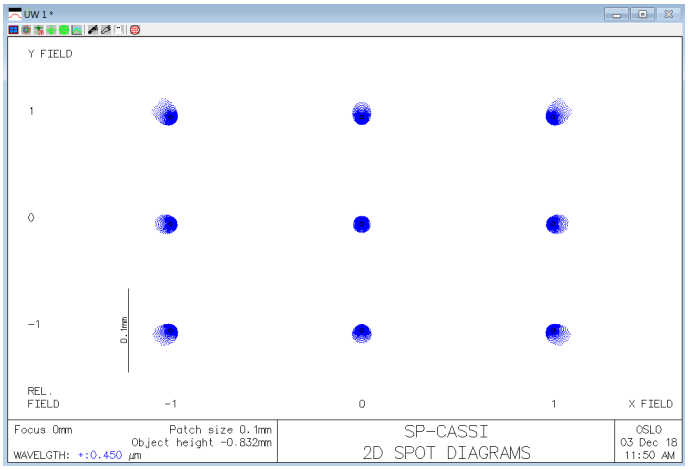

(b) Second wavelength 450 nm

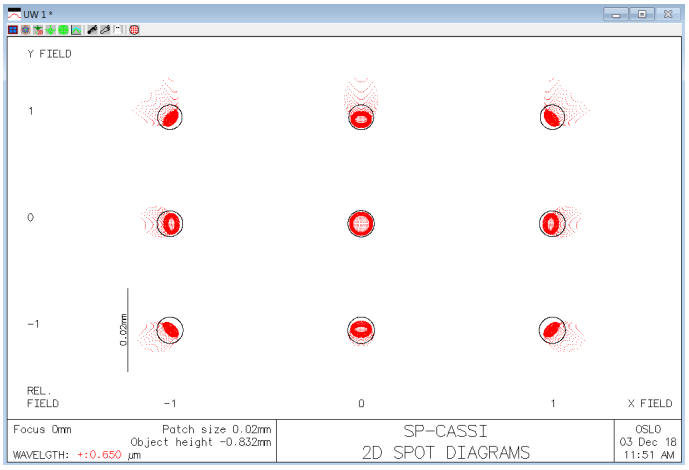

(c) Third wavelength 650 nm

Figure 3.12: Spot diagrams of the combination of prism and imaging lenses of SP-CASSI.

ularly subtle astigmatism exists in the wavelength 587.56 mm. Overall aberration of the system is under the acceptable condition.

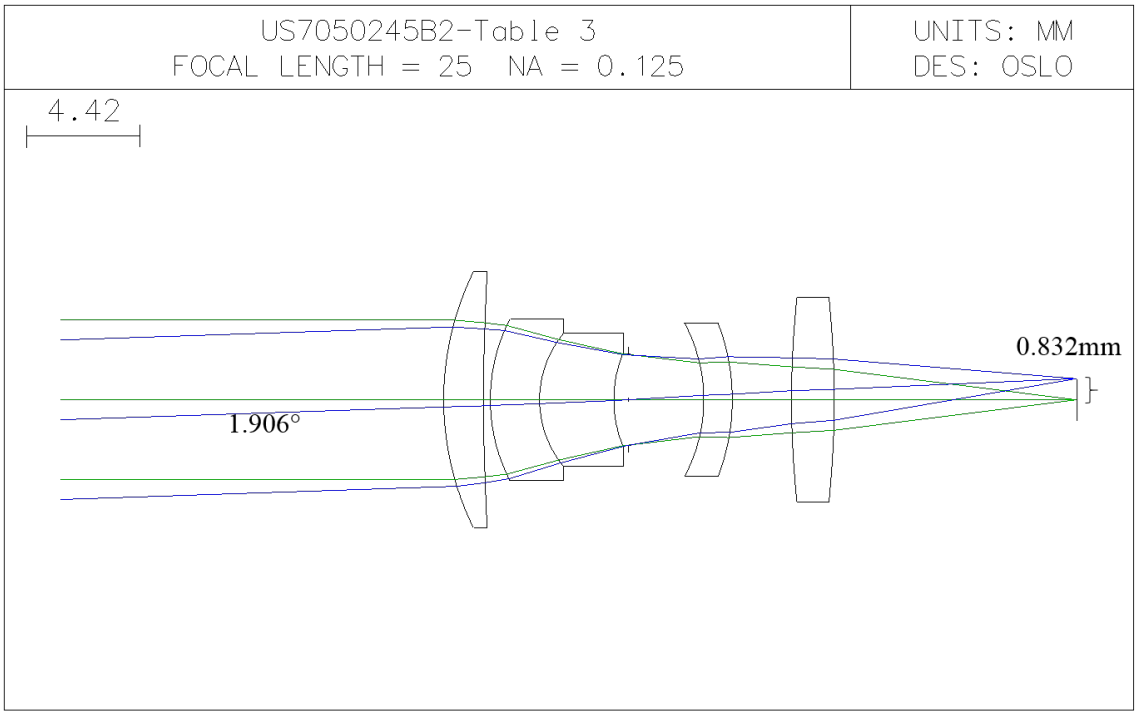

Figure 3.13: F/4 Objective lens for 128 × 128 pixels coded aperture is under the ray tracing of axial rays and off-axis rays at full FoV.

3.4.1.2 System Dispersion

Optical system aperture is determined by the smallest optical component to control the light throughput into the system. In our case, the coded aperture has the smallest size in the SP-CASSI system. The objective lens was based on the same design of imaging lens so that the *image numerical aperture* at the image plane of the objective lens can match the *object numerical aperture* to the following imaging lens straight away, which saves the time in finding a new objective lens that can pair up with. Although the FoV in this case is limited to 1.906°, it can be changeable with the specific needs in applications. At this stage, the goal is to focus on the performance of the core part of the SP-CASSI. The coded aperture mask in this case, was designed as a 128 × 128 random pattern with 13 µm, which gives a size of 1.664 mm × 1.664 mm to the objective lens as the spatial modulator to "punch" the incoming rays. In other words, the mask restricts the size of image that can be collected by the objective lens to a height of 1.664 mm, translated to an "Object Height" of 0.832 mm in OSLO. As the mask was placed at the effective focal distance

of the objective lens, the corresponding field angle at such objective height is 1.906° as depicted in Fig. 3.13. An image with the object height of 0.832 mm and NA 0.125 was relayed by the following front imaging lens to strike the prism with an angular coverage of $-1.906°$ to 1.906°, since the imaging lens has the same structure. Therefore, incident angle I to the front surface of the prism exiting from the front relay lens is varied from $I_0 - 1.906°$ to $I_0 + 1.906°$ over all the wavelengths, where I_0 denotes the on-axis ray's incident angle on the front surface.

Due to the dispersion effect from the prism, additional angular deviation through Eq. (3.21) would contribute to all the wavelengths unequally, leading to unequal image height at image plane of back imaging lens. That is the source of the dispersion capability of the SP-CASSI. However, the prism imposes angular deviation asymmetrically on monochromatic rays at varied incident angles, corresponding to unsymmetrical size on monochromatic image. A full monochromatic image is determined by rim rays exiting from the front imaging lens, i.e. upper ray defined at $I_0 + 1.906°$ and lower ray defined at $I_0 - 1.906°$, besides central ray at I_0. Quantitatively speaking, lower ray and upper ray at 587.56 nm are altered to 40.4414°, 39.7448° and 39.2459°, respectively, when the incident angle I_0 is 41.5° to an BK7 prism at which Sellmeier coefficients of refractive index are as follows,

$$b_1 = 1.03961212,\ b_2 = 0.231792344,\ b_3 = 1.01046945,$$
$$c_1 = 0.00600069867,\ c_2 = 0.0200179144,\ c_3 = 103.560653.$$

The relative angular deviation of lower ray and upper ray referred to central ray are $-2.4048°$ and 2.6025°, respectively, according to Eq. (3.19). The unequal portion of the deviated angles indicates that lower ray and upper ray would be no longer symmetrical to the on-axis ray; thus, causing unsymmetrical aberration of image height corresponding to their angles through the back relay lens, which are -1.050 mm and 1.1364 mm at final image plane while the corresponding object height is 0.832 mm and -0.832 mm,

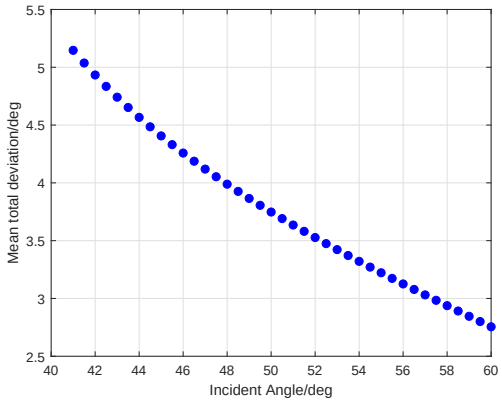

(a) Mean total deviation range over spectral region of interest as a function of the incident angle

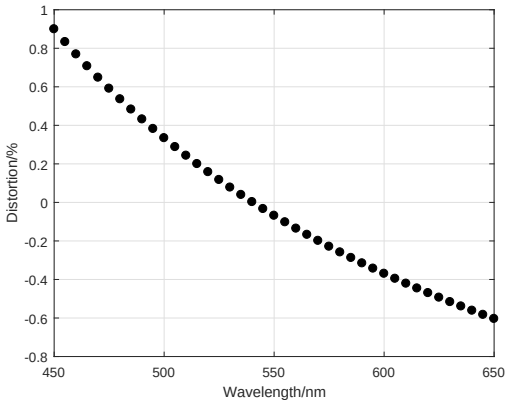

(b) Monochromatic distortion as a function of wavelength

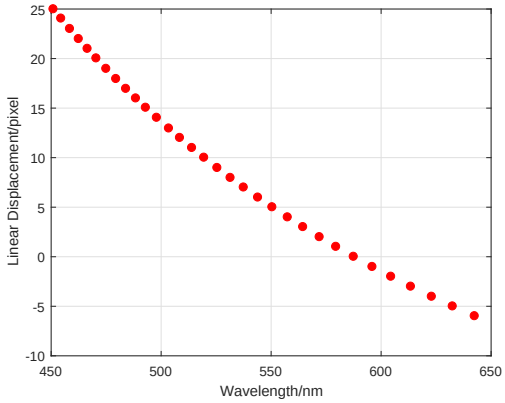

(c) Dispersion displacement at rotation angle 49.4489°

Figure 3.14: Linear Dispersion Analysis of SP-CASSI.

respectively. A relevant curve of total angular deviation over 450 nm to 650 nm with respect to the rotation of the prism could be drawn in Fig. 3.14a, showing the mean value

of polychromatic total angular deviation as a function of the incident angle from 41° to 60°, while note that the critical angle is considered to prevent the prism from occurring the internal reflection. From the figure, the optimal angle that yields an image height of 1.664 mm corresponding to 3.812° was explicitly found at 49.4489°. Under such incident angle, the prism yields the deviation angle −1.9556° and 1.8448° at 587.56 nm corresponding to the image height 0.8537 mm and −0.8053 mm, which causes a distortion of −0.3% compared to the object of 1.664 mm, where − indicates the actual image height is smaller than the expectation. By comparing to the object height 0.832 mm, it can be further found out that lower ray results in a barrier distortion and upper results in a cushion distortion. This can be extended to the whole bands, yielding a distortion of 0.9% at 450 nm and −0.6% as shown in Fig. 3.14b. Eventually, the dispersion function of on-axis single point source versus 450 nm to 650 nm in this case was pixelated with 2 sensor pixels of 13 nm as described in Fig. 3.14c, wherein the vertical axis has been adjusted to move the origin point where 587.56 mm arrives at detector. Based on this function, a set of wavelengths corresponding to linear dispersion displacement can be generated to build up a system calibration matrix. The following simulation in Fig. 3.15 gives a visualisation of single point dispersion in the SP-CASSI.

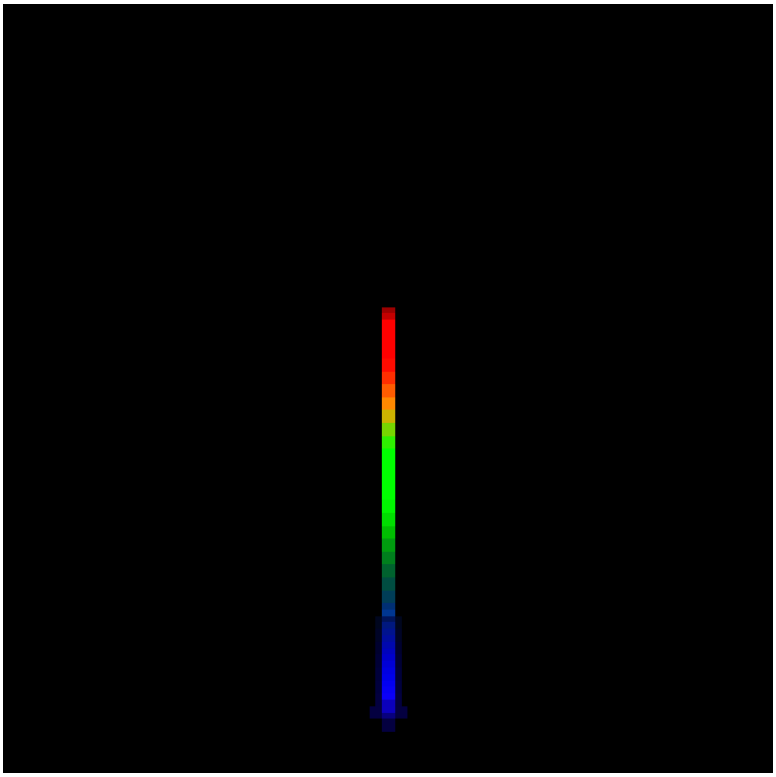

(a) Front view

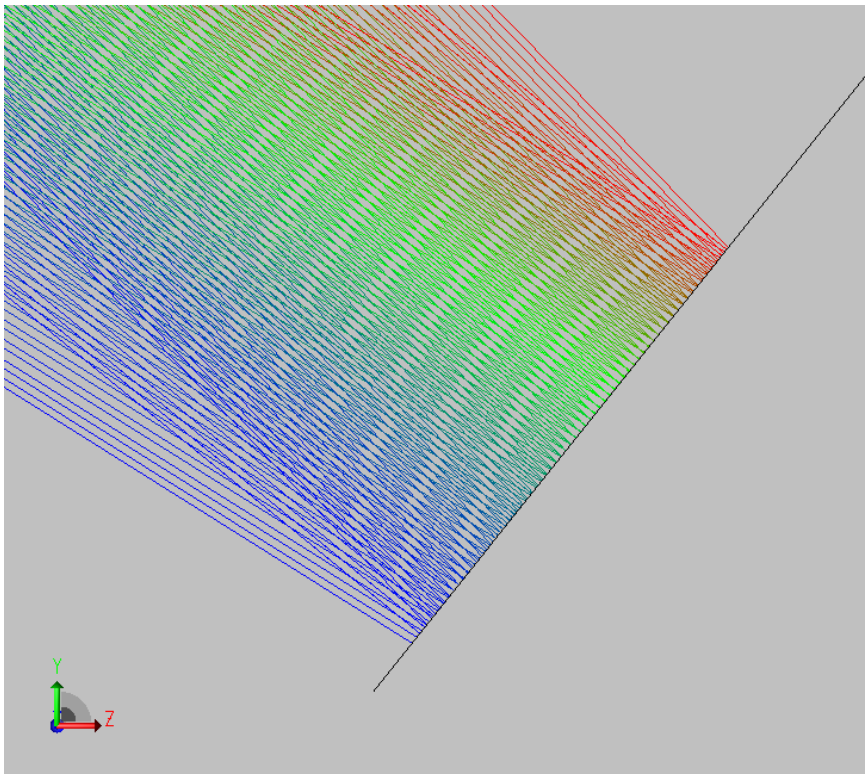

(b) Side view

Figure 3.15: Dispersion of a single pixel source simulated in TracePro: (a) the false RGB image at front view of detector, (b) the wavelength-dependant colour rays at side view of detector.

3.4.2 Double-Amici-Prism System Design

3.4.2.1 Double Amici Prism

Double Amici prism was introduced into CASSI [96–98] to bring a feature of undeviated optical axis for both incident rays and exiting rays during the propagation in double amici prism. This feature, shown in Fig. 3.16, allows the structure of CASSI design to be a direct-view system, instead of the structure like SP-CASSI. The double amici prism is a compound prism cemented by three single prisms with two types of materials. To undevi-

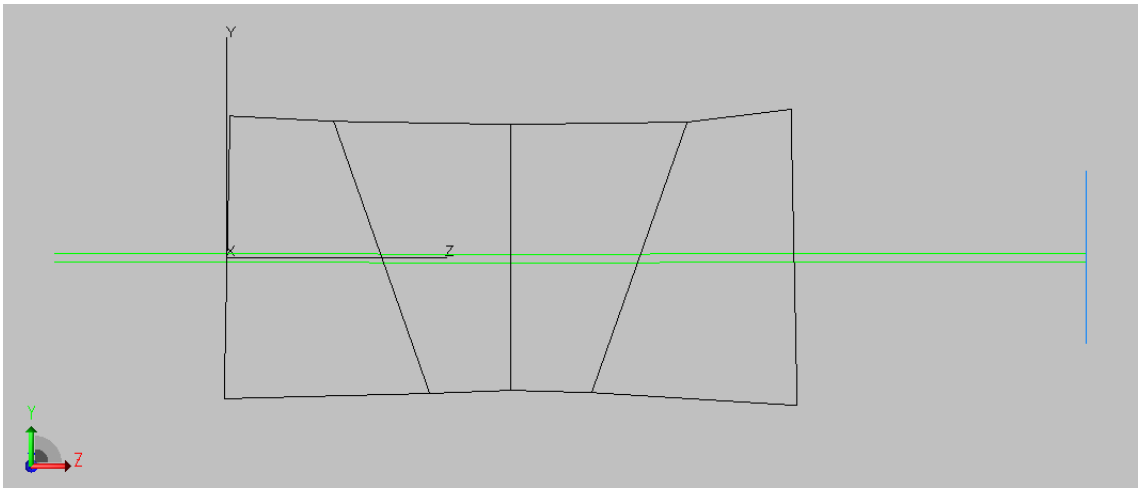

Figure 3.16: Central wavelength 550 nm propagates through double amici prism from the left side to the right side and the detector is placed at blue plane. The double amici prism consists of four cemented prisms, which keeps the central wavelength remain the same optical axis after the prism.

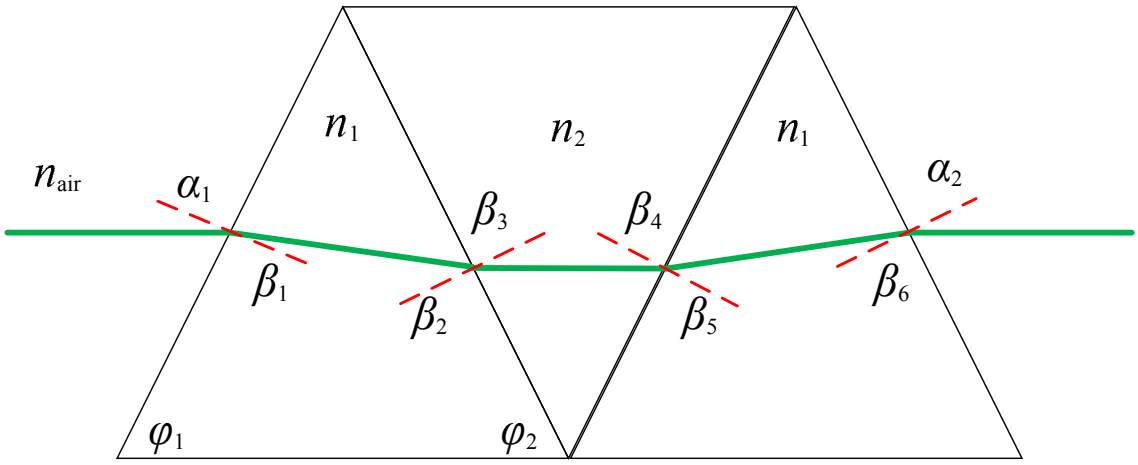

Figure 3.17: Schematic of propagation of 550 nm in double amici prism.

ate exiting angle from incident angle, the prism adopts a symmetrical combination where front prism and rear prism are identical with lower refractive index and middle prism has a higher refractive index. The schematic of central wavelength 550 nm propagating in double amici prism is shown in Fig. 3.17 where the Snell's law is applied for multiple times with $n_2 > n_1 > n_{air} = 1$ as follows,

$$n_{air} \sin\alpha_1 = n_1 \sin\beta_1, \tag{3.26}$$

$$180^\circ - \varphi_1 - \varphi_2 = \beta_1 + \beta_2, \tag{3.27}$$

$$n_1 \sin \beta_2 = n_2 \sin \beta_3, \tag{3.28}$$

$$180^\circ - \varphi_2 - \varphi_2 = \beta_3 + \beta_4, \tag{3.29}$$

$$n_2 \sin \beta_4 = n_1 \sin \beta_5, \tag{3.30}$$

$$180^\circ - \varphi_1 - \varphi_2 = \beta_5 + \beta_6, \tag{3.31}$$

$$n_1 \sin \beta_6 = n_{air} \sin \alpha_2, \tag{3.32}$$

where φ_1 and φ_2 denote two bottom angles of front prism or rear prism and middle prism, therefore it has to be a isosceles triangle with bottom angle of φ_2. α_1 and α_2 denote incident angle and exiting angle, which is associated to front prism angle φ_1. The series of angles β denote all the refracted angles inside prism. To make sure the undeviated condition to central wavelength, $\alpha_1 = \alpha_2$ deduces $\beta_3 = \beta_4 = 90^\circ - \varphi_2$. Hence, design of double amici prism only depends on front prism angles (φ_1, φ_2) and prism materials (n_1, n_2).

Provided that the undeviated condition is satisfied, angular deviation of double amici prism is of more importance to determine the capability of a dispersive spectrometer. For instance, referring to the setup in [96], the bottom angles of front prism are 85.9° and 73.7° and the material SK2 was used for the front prism and the material SF4 was used for the rear prism. By applying this setup in Matlab to calculate the associated angles, the incident angle $\alpha_1 = 4.1^\circ$ yields an exiting angle $\alpha_2 = 4.01^\circ$ at central wavelength 550 nm, which gives an angle difference of 0.09°. By extending to all on-axis rays with spectral

Table 3.1: Double Amici Prism Angular Deviation.

Band	**Prism Combinations**				
/nm	**NSK2/SF4**	**CaF2/Fused Silica**	**BK7/NBaF10**	**BK7/NSF11**	**NLaK12/NSF6**
450	$-0.45°$	$-0.11°$	$-0.25°$	$-0.13°$	$-0.51°$
500	$-0.18°$	$-0.05°$	$-0.1°$	$-0.05°$	-0.2
550	$0.00°$	$0.00°$	$0.00°$	$0.00°$	$0.00°$
600	$0.13°$	$0.04°$	$0.07°$	$0.04°$	$0.14°$
650	$0.22°$	$0.07°$	$0.12°$	$0.06°$	$0.25°$

range from 450 nm to 650 nm, the prism yields a range of exiting angles from 3.56° to 4.23°, overall angular deviation of 0.67°. Table 3.1 shows the comparison of double amici prism dispersion result by varying different combinations in which the combination N-SK2/SF4 and CaF2/Fused Silica were used in prototyping of Double-Amici-Prism CASSI [96–98] as the reference and other combinations are chosen to compare. Although the reference combinations were customised for different applications, the spectral range is limited to the range of 450 nm to 650 nm for the convenience of comparing to others. The selection of prism materials obeys the rule that front and rear material has a lower refractive index than middle one. Five materials were chosen from *SCHOTT Abbe Diagram*, which are BK7 with $n_d = 1.5168$ and $V_d = 64.17$, N-BaF10 with $n_d = 1.67003$ and $V_d = 47.11$, N-SF11 with $n_d = 1.78472$ and $V_d = 25.68$, N-LaK12 with $n_d = 1.6779$ and $V_d = 55.20$ and N-SF6 with $n_d = 1.80518$ and $V_d = 25.36$, which groups into three combinations. Two combinations as reference are N-SK2 ($n_d = 1.60738$ and $V_d = 56.65$) / SF4 ($n_d = 1.7552$ and $V_d = 27.58$) and CaF2 ($n_d = 1.4338$ and $V_d = 94.99$) / Fused Silica($n_d = 1.4585$ and $V_d = 67.82$).

Those combinations were chosen to generate several types of angular deviation to study any consequences to the performance of Double-Amici CASSI by tilting different angular deviation. To keep the central wavelength 550 nm undeviated, the bottom angles were calculated in Matlab referring to Eq. (3.26), which has (85.9°, 73.7°) at N-SK2/SF4, (88°, 58.9°) at CaF2/FS, (80°, 59.9°) at BK7/N-BaF10, (88°, 86.2°) at BK7/N-SF11 and (87°, 74.8°) at N-LaK12/N-SF6. Concretely, the angular deviation between incident angle and exiting angle is not ideally zero. Under such settings, five combinations yield inci-

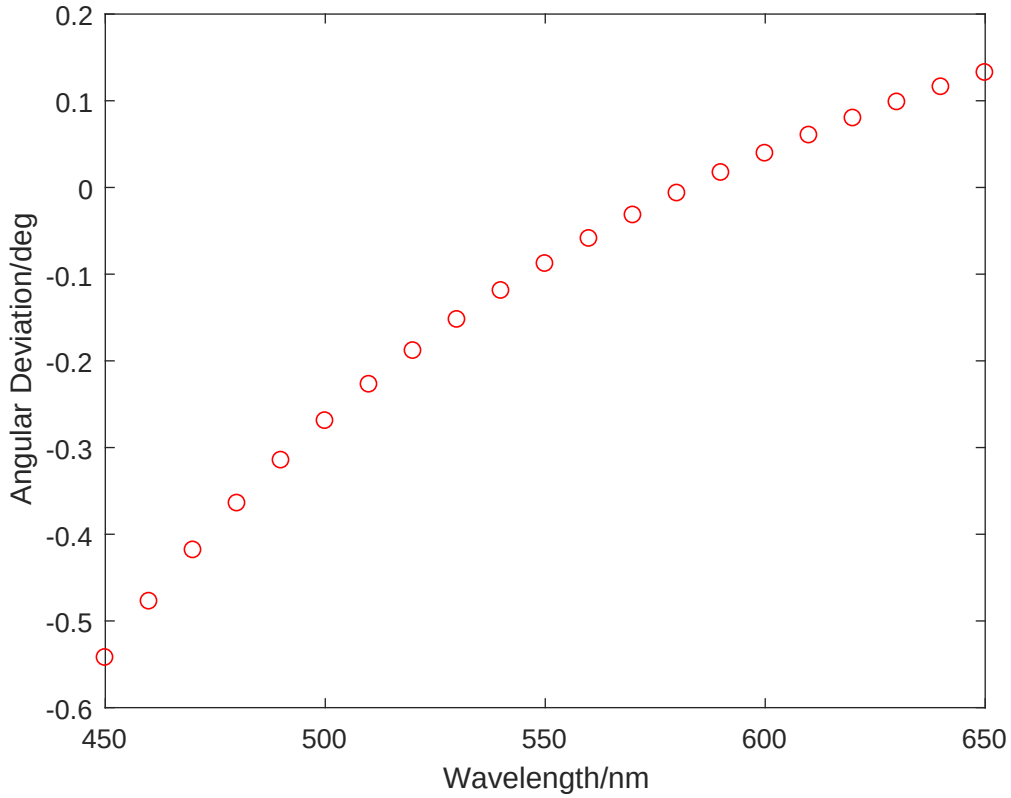

Figure 3.18: Angular deviation of double amici prism with 85.9° and 73.7° applied in N-SK2 and SF4 prisms.

dence/emergence pair 4.1°/4.01°, 2°/1.998°, 10°/10.0035°, 2°/1.9995° and 3°/3.0013°. Such difference is small enough to be negligible when considering the dispersion displacement. Additionally, it should be noted that the total angular deviations are 0.67° for N-SK2/SF4, 0.18° for CaF2/FS, 0.37° for BK7/NBaF10, 0.19° for BK7/N-SF11 and 0.76° for N-LaK12/N-SF6.

3.4.2.2 Double-Amici CASSI

The basic idea of using double amici prism is to solve the problem of the deviated optical axis of system due to a single prism. It becomes unnecessary to use relay lens or imaging lens at both sides of the prism to focus the image. The initial prototype of Double-Amici CASSI selected off-the-shelf optics [96], Edmund 45762 as the only relay lens between the coded aperture and the prism. As shown in Fig. 3.19, this relay lens is an F/8 system

with an effective focal length of 30 mm. From MTF diagrams in Fig. 3.20, the Edmund 45762 behaves well with MTF 50% at 80 *lp/mm* at 550 nm and at 50 *lp/mm* at 650 nm but only stays at 24 *lp/mm* at MTF 50% and barely holds MTF 20% after 36 *lp/mm* at 450 nm. As a matter of fact, the required resolution in the research with respect to Double-Amici CASSI was only 25 *lp/mm* for 19.8 µm smallest feature of coded aperture. Hence, this relay lens could just pass the system requirements.

The prototype of Double-Amici CASSI was constructed by the Edmund relay lens cascaded by Double-Amici prism (N-SK2/SF4) [60] that has a length of 12 mm. The distance from first surface of the relay lens to the coded aperture as the first element was adjusted to 39.3 mm. The last surface to the first surface of the double-amici prism is 8.6 mm and the last surface of the double-amici prism to the detector is 23.2 mm, as shown in Fig. 3.21. By introducing the prism into the system, the MTF diagrams can be seen in Fig. 3.22 that the resolution at the wavelength 450 nm was slightly improved from

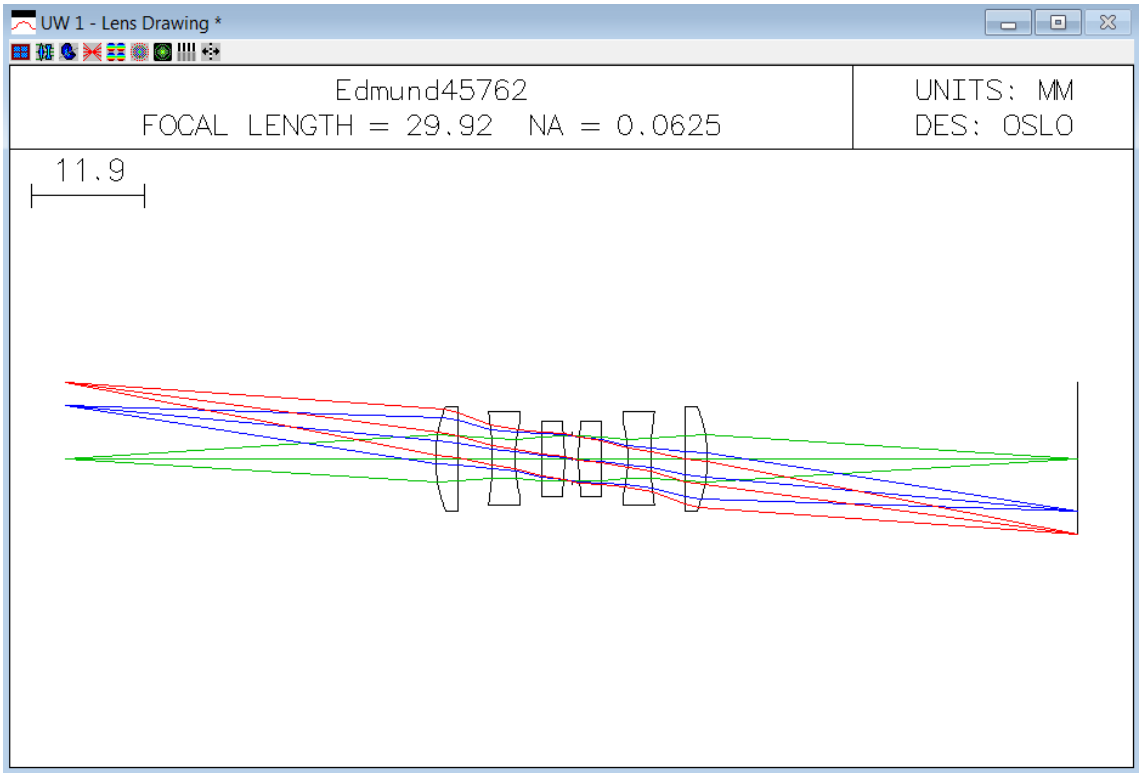

Figure 3.19: Edmund relay lens 30 mm Focal Length F/8: rays emit from three field point (full field, 0.707 field and axial point) to demonstrate the imaging performance when NA is 0.0625. The system achieves a -1 magnification.

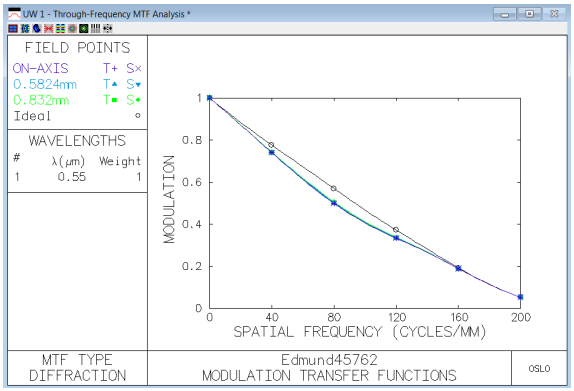

(a) Primary wavelength 550 nm

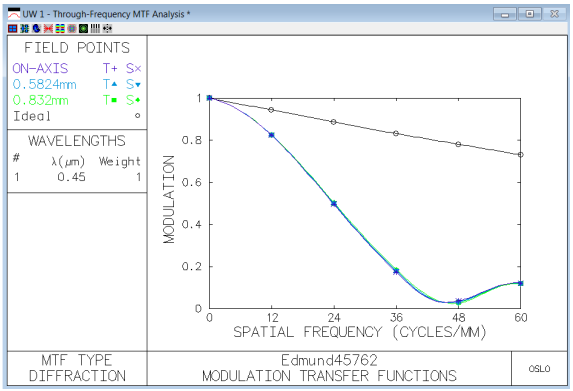

(b) Second wavelength 450 nm

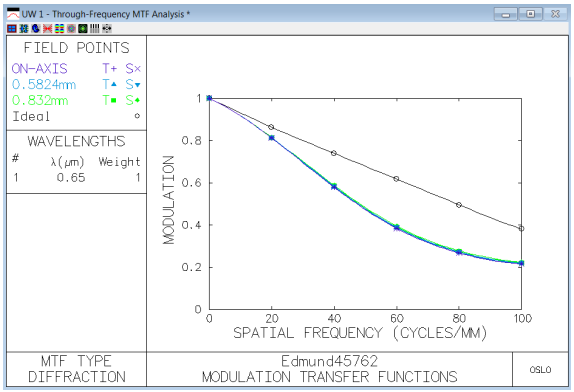

(c) Third wavelength 650 nm

Figure 3.20: Monochromatic MTF diagram of Edmund 45762 relay lens.

25 *lp/mm* to 36 *lp/mm* nearby while there exists a major gap of 10% to 20% between tangential and sagittal lines across all three field points at the central wavelength and narrow gap at other wavelengths, which indicates the prism contributes the aberration mainly in tangential direction. Further investigating the spot diagrams shown in Fig. 3.23, at three wavelengths by uniformly sampling 9 field points across full field of image plane (fractional coordinates Y -1 to +1 and X -1 to 1), we can find out that those spots present an

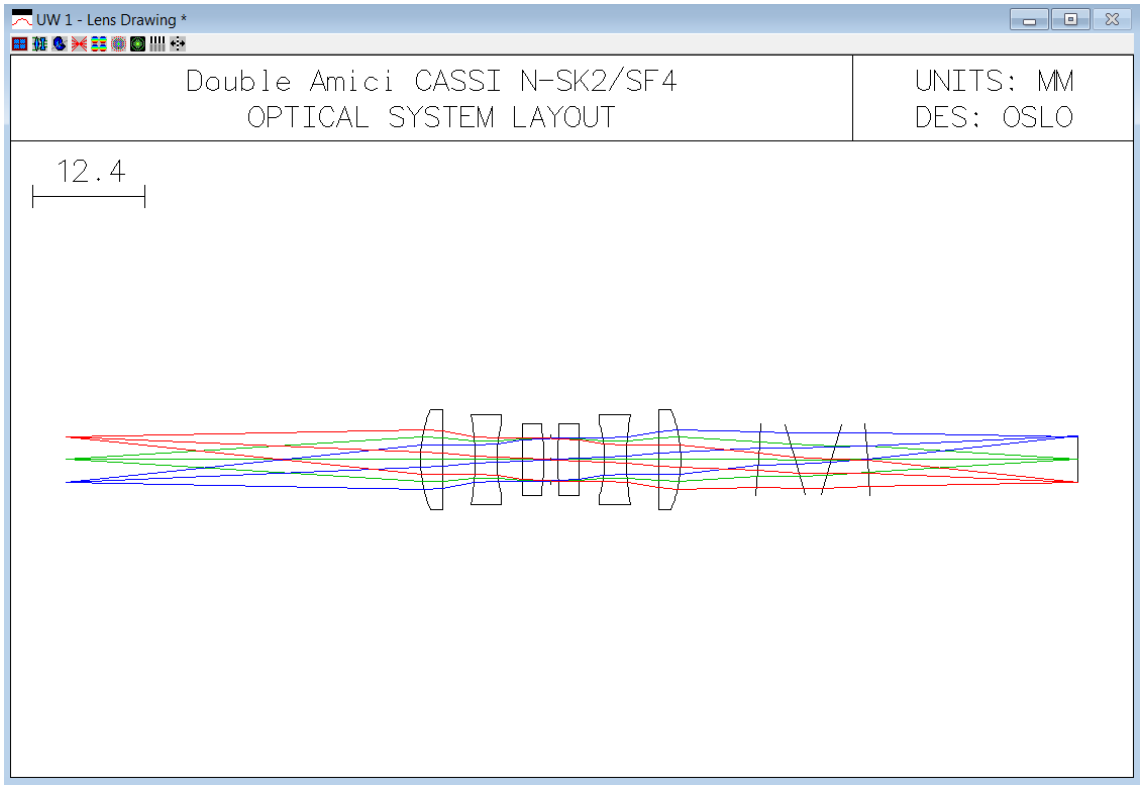

Figure 3.21: Overview of Double-Amici CASSI based on N-SK2/SF4 prism shows the the propagation of rays from three field points. The size of aperture determines the height of off-axis field points.

unsymmetrical shape, especially for the ellipse shape in 450 nm, which illustrates that the system suffers from the aberration. According to the geometrical shapes of aberration, the Spherical Aberration contributes most of the Seidel Aberrations. Quantitatively, we can read the specific values of the Seidel Aberrations by invoking the *Aberration* function in OSLO. However, it should be noted before directly read out the numbers, that the calculation of Seidel Aberrations is based on the paraxial approximation in OSLO, whilst the paraxial approximation assumes the evaluated system is invariant to the rotation as the optical axis, which means it is a symmetrical system. To the dispersive system in our case, due to the existence of the prism, the special surface would turn the paraxial approximation invalid. Although the function can still work, all the evaluation with respect to the paraxial approximated values would just treat special surface as a refracted plane with curvature remaining zero, perpendicular to the optical axis. As for the titled surface on the prism, the refraction would no longer be considered with the tilted angle between

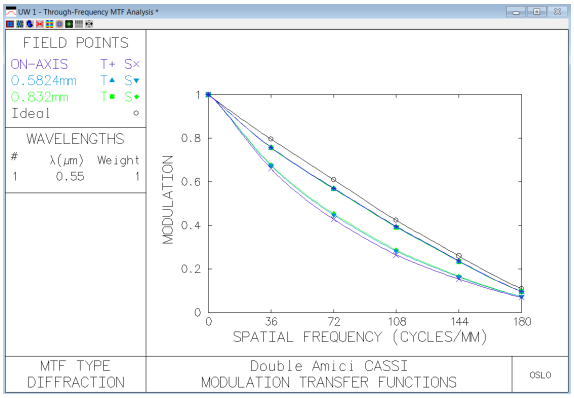

(a) Primary wavelength 550 nm

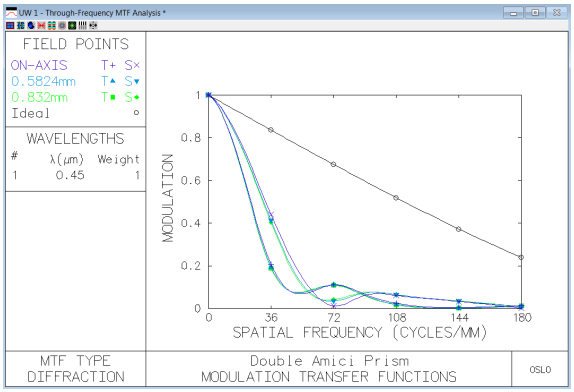

(b) Second wavelength 450 nm

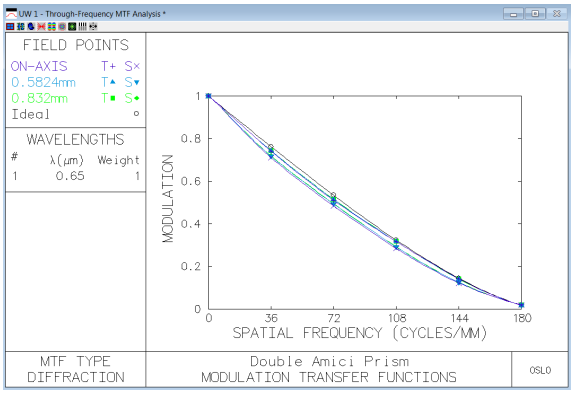

(c) Third wavelength 650 nm

Figure 3.22: Monochromatic MTF diagram of Double-Amici CASSI with N-SK2/SF4.

the surface and incident angle. Despite invalid paraxial approximation, it could give us some useful information of aberrated situation when paraxial rays go through such plane intermedium with the refractive index different from the air. Fig. 3.24 shows the bar chart of the Seidel Aberrations [4], including AST3, CMA3, DIS3, PTZ3 and SA3, at three main wavelengths in the use of 5 prism combinations for Double-Amici Prism, compared to the Edmund relay lens. As we can see from the chart, to the Double-Amici systems,

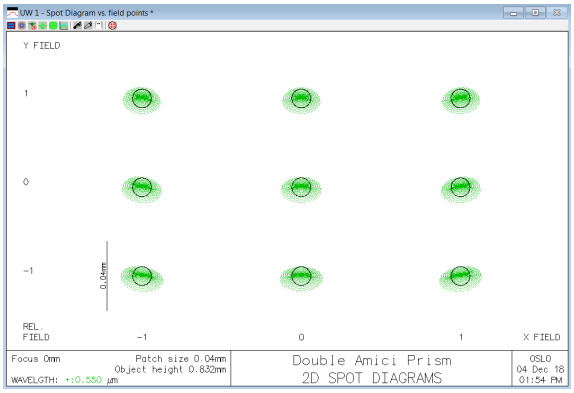

(a) Primary wavelength 550 nm

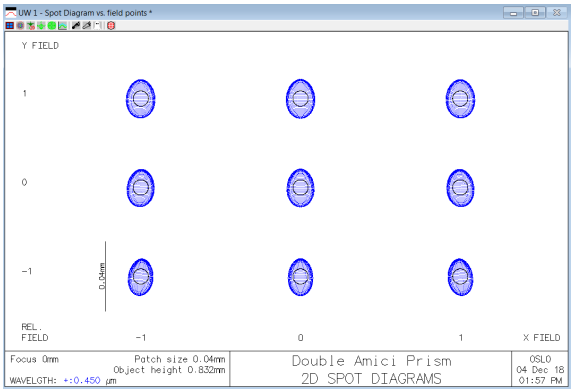

(b) Second wavelength 450 nm

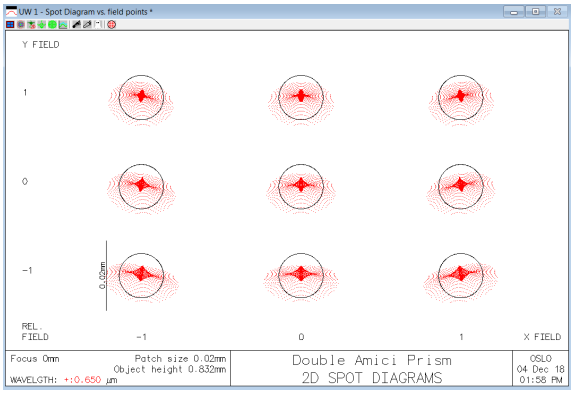

(c) Third wavelength 650 nm

Figure 3.23: Spot diagram of Double-Amici CASSI with N-SK2/SF4.

SA3 contributes above -10×10^{-3} which takes most of weights in the total aberration across all 5 prism combination, subtle PTZ3 and CMA3 followed. It can be believed that the SA3 was brought in by the relay lens itself while the prism eases this aberration by average 7% across all three bands. The prism, indeed, brought in the extra CMA3 with 0.12×10^{-3}.

From the analytical results of Double-Amici CASSI, it can be seen the essence of

custom relay lens to accommodate the prism, rather than using the off-the-shelf optics; hence, the following Ultraviolet-Visible CASSI was designed with a new structure to improve the aberration and MTF.

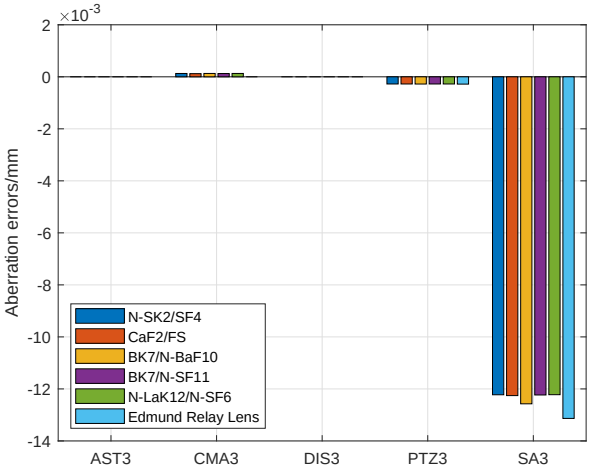

(a) Primary wavelength 550 nm

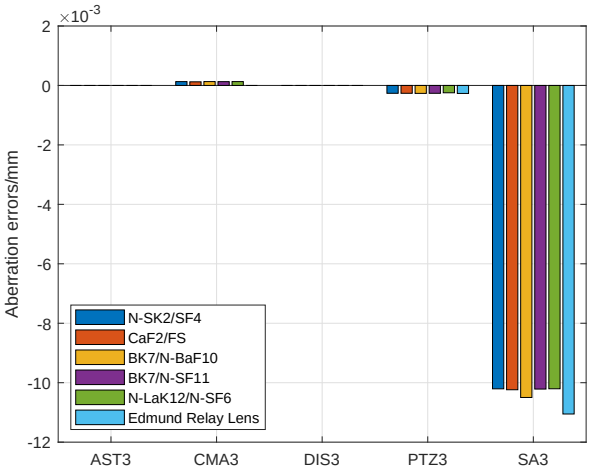

(b) Second wavelength 450 nm

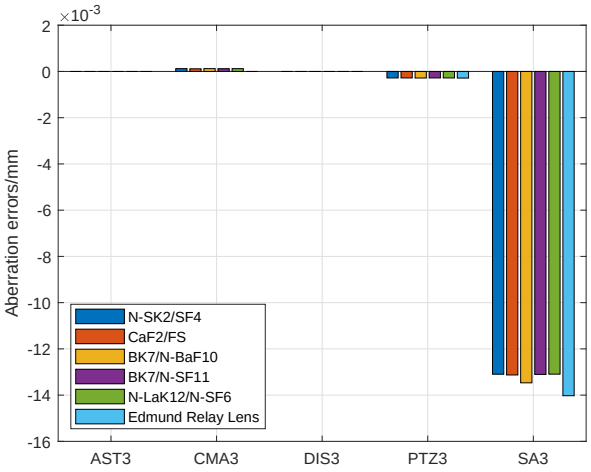

(c) Third wavelength 650 nm

Figure 3.24: Bar chart of Seidel Aberrations showing 5 third-order aberrations, *AST3*, *CMA3*, *DIS3*, *PTZ3* and *SA3* at three wavelengths, in the Edmund relay lens and 5 Double-Amici systems based on 5 prism combinations.

3.4.2.3 Ultraviolet-Visible CASSI

3.4.2.3.1 System Layout

As an application-oriented version of Double-Amici CASSI, the relay lens used in Ultraviolet-Visible CASSI (UV-CASSI) was customised in optical design software based on Cooke Triplet and further modified with embedded field lens [98]. Particularly, the double amici prism was placed at the collimated space in the relay lens, rather than the structure like Double-Amici CASSI. Such kind of design can ease the aberration due to the asymmetrical structure of prism (the existence of the tilted surface to generate the refraction in prism) by optimising the rear triplet lens group in optical design software. As shown in Fig. 3.25, the UV-CASSI was designed for a specific application which requires a very broad spectral range from 400 nm to 700 nm, where 500 nm is the central wavelength that passes through the prism undeviated. As a reference system compared to other structures of CASSI variations, this system has an F/8 to accept a target of *Object Height* 3.788 mm with magnification of -1. The object height was set to 0.832 mm in

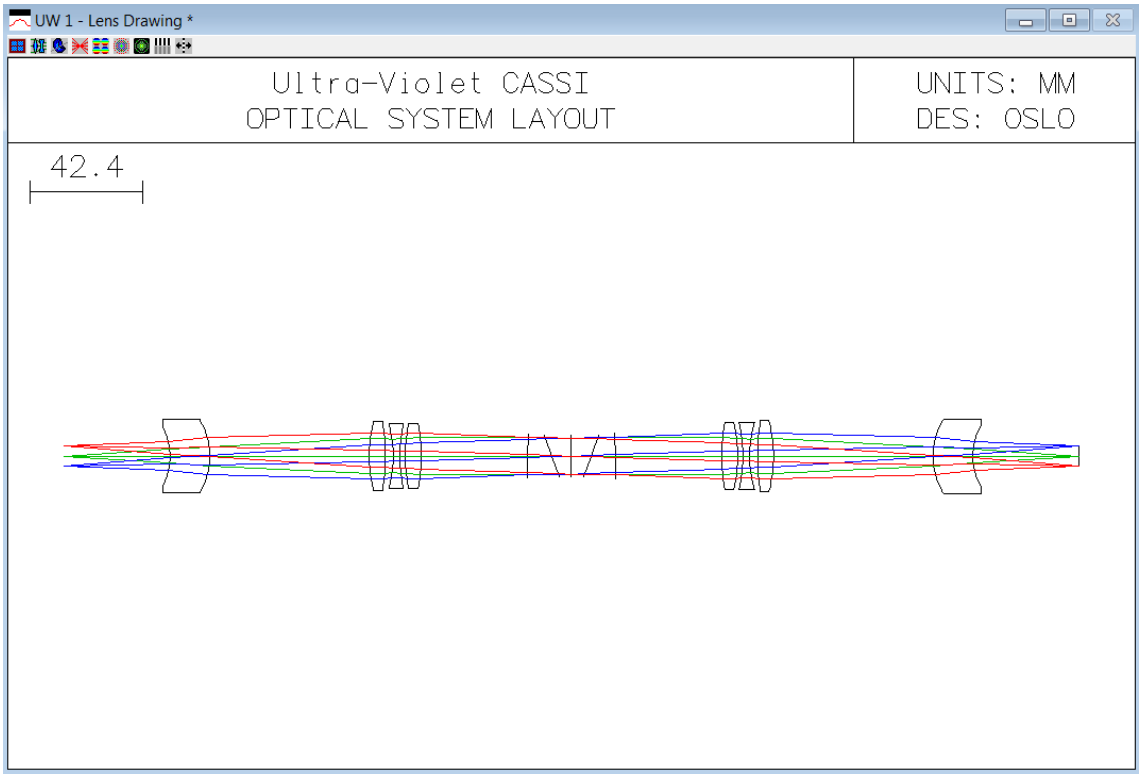

Figure 3.25: Overview of UV-CASSI based on CaF2/Fused Silica prism.

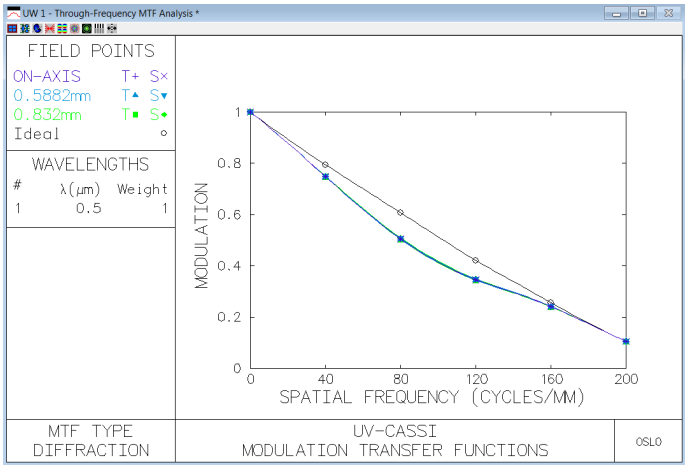

(a) Primary wavelength 550 nm

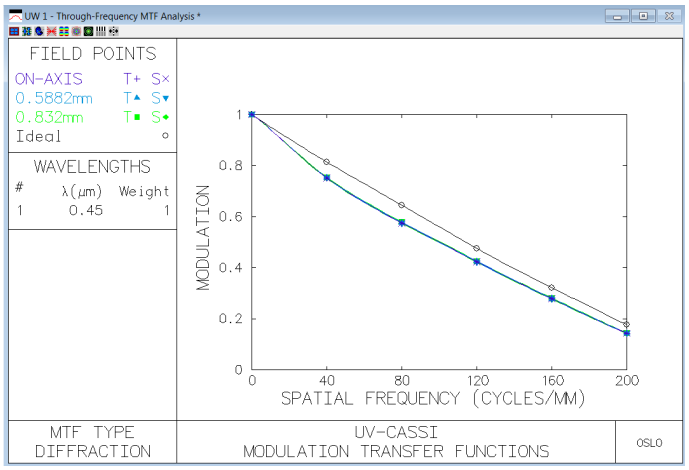

(b) Second wavelength 450 nm

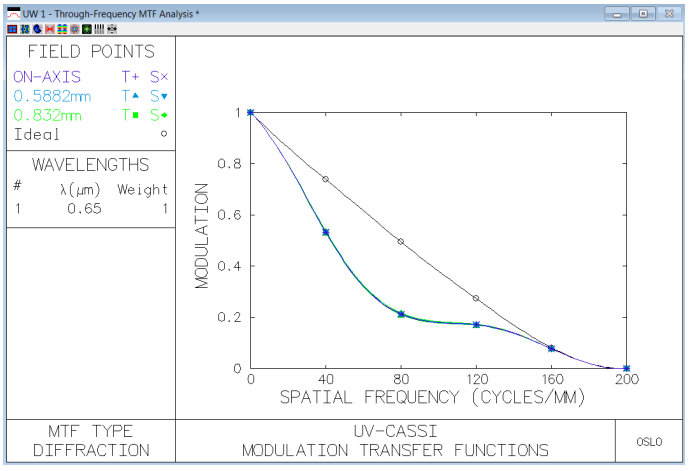

(c) Third wavelength 650 nm

Figure 3.26: Monochromatic MTF diagrams of UV-CASSI.

OSLO to fairly analyse the optical performance of UV-CASSI.

By setting the parameters to evaluate the system under the same condition as in

Double-Amici CASSI, the monochromatic MTF diagrams in Fig. 3.26 can be seen that tangential MTF and sagittal MTF are matched very well, with MTF 50% at 80 *lp/mm* at 500 nm, 100 *lp/mm* at 450 nm and 40 *lp/mm* at 650 nm. Compared to Single-Prism CASSI and Double-Amici CASSI, the resolution at short wavelength was dramatically enhanced due to the materials particularly considered for the region of short wavelength, while long wavelength was tradeoff for the enhancement in short wavelength. Combined with the spot diagrams in Fig. 3.27, the shape of spots across full filed is symmetrically round and centralised within the Airy Disk, despite that the central wavelength and short wavelength suffer from the Spherical Aberration.

3.4.2.3.2 System Dispersion

Unlike analysing the dispersion of the independent prism in previous systems, the dispersion and displacement on image plane was complicated to calculate due to the structure that the prism was embedded into relay lens. As a matter of fact, the acquisition of dispersion displacement and further calibration data was obtained through the experiment, rather than through any pre-design stage, which is one of the common problems existing in CASSI framework and that the work in this thesis wants to solve. The dispersion equation based on experimental data was fit to an exponential formation [98] as a function of wavelength, which is described as,

$$\lambda(x) = 320.2\ \exp(0.000384(x-16)) + 103.6\ \exp(0.03373(x-16)), \tag{3.33}$$

where x denotes the index of pixel location at detector, the origin of which has been shifted to the location of the central wavelength 500 nm. The smallest feature of (3.33) is 7.4 µm while in our simulation double smallest feature was used so that the calibration wavelengths within 450 nm to 650 nm were picked up by selecting every two shifting pixels in Eq. (3.33). A set of total 14 wavelengths, as displayed in Table 3.2, shows the spectral width between adjacent channels is quite larger than SP-CASSI, resulting a fewer number of dispersed channels and shorter displacement at detector as simulated in

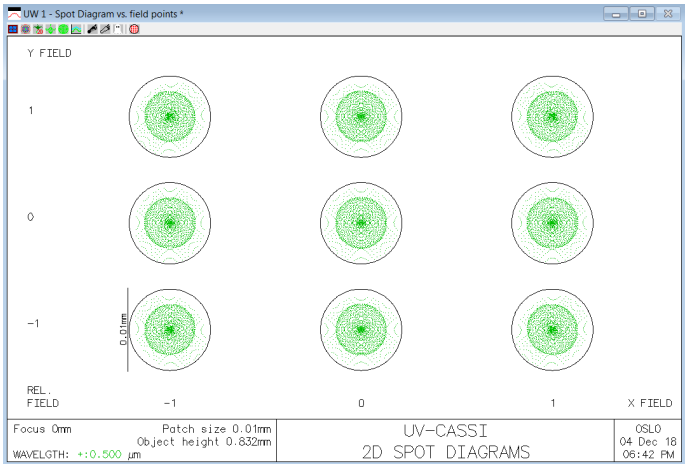

(a) Primary wavelength 550 nm

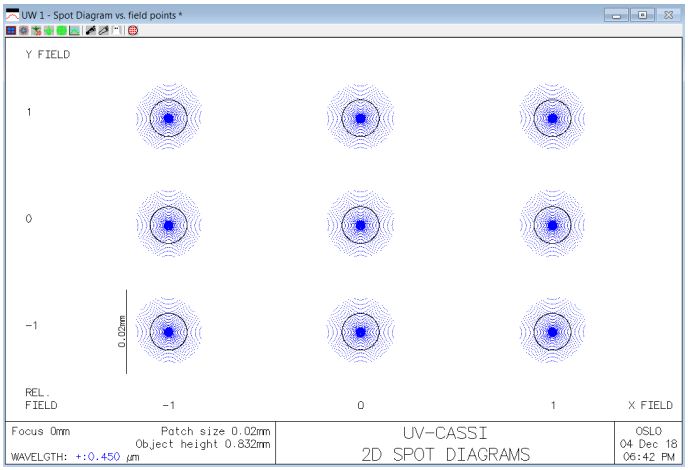

(b) Second wavelength 450 nm

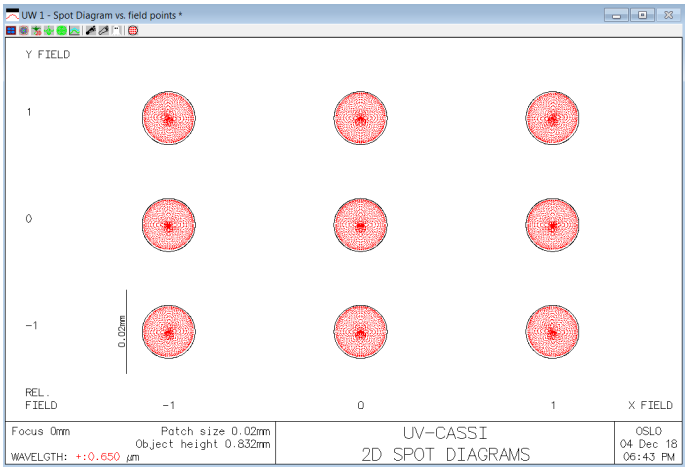

(c) Third wavelength 650 nm

Figure 3.27: Spot diagrams of UV-CASSI.

TracePro in Fig. 3.28.

Table 3.2: Ultraviolet-Visible CASSI Dispersion Displacement.

Band /nm	**Index of Pixel /No.**	**Relative pixel location /μm**
456.7	-8	-59.2
466.4	-6	-44.4
476.8	-4	-29.6
487.9	-2	-14.8
499.7	0	0
512.3	2	14.8
525.9	4	29.6
540.3	6	44.4
555.7	8	59.2
572.2	10	74
589.9	12	88.8
608.7	14	103.6
628.8	16	118.4
650.4	18	133.2

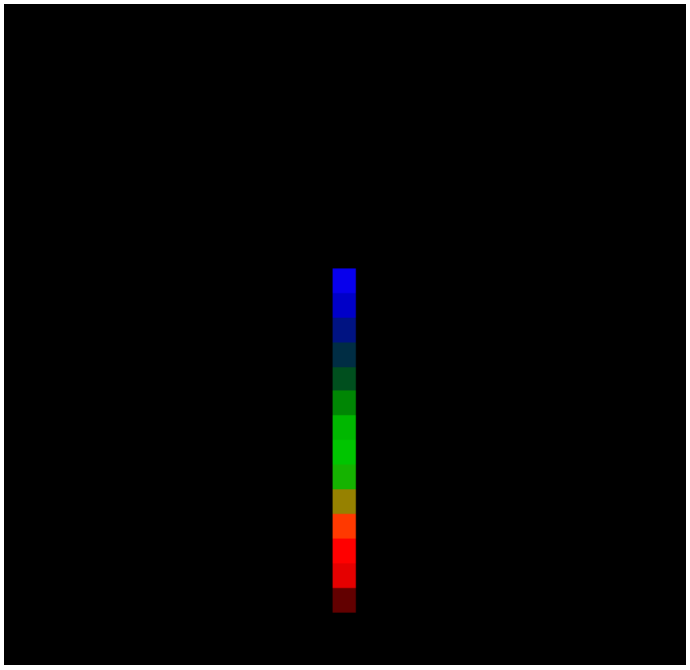

Figure 3.28: Single pixel dispersion displacement was done in TracePraco by illuminating a single pixel source tUltraviolet-Visible CASSI. The single pixel source contains 27 spectral bands and linear displaced at detector, which is linked to Table 3.2.

3.4.3 Dual-Prism System Design

Dual-Prism, a structure of two detached identical prisms mirror-symmetrically placed to each other, has been widely utilised for electro-optics application such as the introduction of group-delay dispersion to compensate the chirp of ultrashort laser pulses etc [133]. The idea of the utilisation of Dual-Prism is due to the parallel status between incident surface and exiting surface, providing the wavelength-dependant displacement without the angle altered after exiting prism, rather than the dispersion mechanism in previous CASSIs using the angular deviation to alter the location of different wavelengths at image plane. By doing that, the spectral dispersion displacement at image plane can be easily controlled to provide extra spectral information by simply tuning the air gap between two prisms without physically replacing or adding any hardware, and changing the detector accordingly in order to remain the central wavelength at the origin of the plane. This feature will enhance the CASSI framework's adaptability to a dynamic environment. In this section, the design and analysis of Dual-Prism CASSI (DP-CASSI) will be detailed.

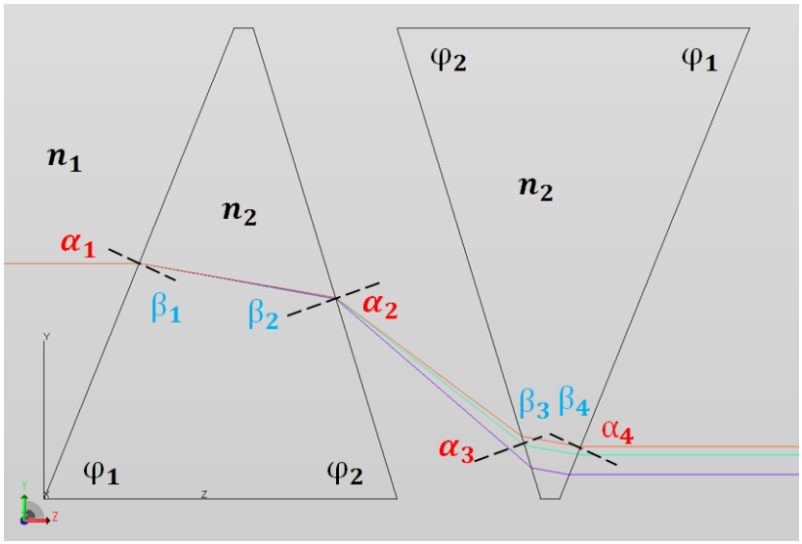

Figure 3.29: Ray propagation in the structure of the dual-prism, with refractive index marked as n_1 and n_2, prism angles φ_1 and φ_2, refracted angles α_{1-4} and β_{1-4}. A single ray combined with three kinds of wavelengths enters from left sided and disperses as three single parallel emerging from right side. This propagation was simulated in TracePro.

3.4.3.1 Dual-Prism Structure

As mentioned above, DP-CASSI utilises a pair of identical triangular prisms with air gap in between, so that the directions of propagation of the rays are undeviated and a relative dispersive displacement in the sagittal plane is generated as depicted in Fig. 3.29. The present dual-prism structure consists of a set of dual-prism with fundamental angles of φ_1 and φ_2, separated by a certain distance. The ray optics of the prism assembly as shown in Fig. 3.29 accord to the following behaviour, when on-axis ray bundle, the central, short and long wavelength strike the surface of the left prism towards the right prism:

Front prism:

$$n_1 \sin(\alpha_1) = n_2 \sin(\beta_1), \tag{3.34}$$

$$\beta_1 + \beta_2 = 180^\circ - (\varphi_1 + \varphi_2), \tag{3.35}$$

$$n_2 \sin(\beta_2) = n_1 \sin(\alpha_2). \tag{3.36}$$

Rear Prism:

$$n_1 \sin(\alpha_3) = n_2 \sin(\beta_3), \tag{3.37}$$

$$\beta_3 + \beta_4 = 180^\circ - (\varphi_1 + \varphi_2), \tag{3.38}$$

$$n_2 \sin(\beta_4) = n_1 \sin(\alpha_4), \tag{3.39}$$

where n_1 denotes the refractive index of air and n_2 denotes the refractive index of prism. A series of angles $\alpha_i, i = 1,2,3$ *and* 4 denote the refracted angles happening in the air and the other series of angles $\beta_i, i = 1,2,3$ *and* 4 denotes the refracted angles happening in the prism. As can be expected, the rays exit the surface of the rear prism (the prism on the right hand side) as three individual rays with the exiting angle α_4 matched to the incident angle α_1, regardless of the wavelengths of the incident rays. Quantitatively speaking, two prisms are identical and parallel to each other, thereby $\alpha_3 = \alpha_2$, likewise $\alpha_1 = \alpha_4$. Note that the incident angle at the surface of the front prism (the prism on the left hand side) is

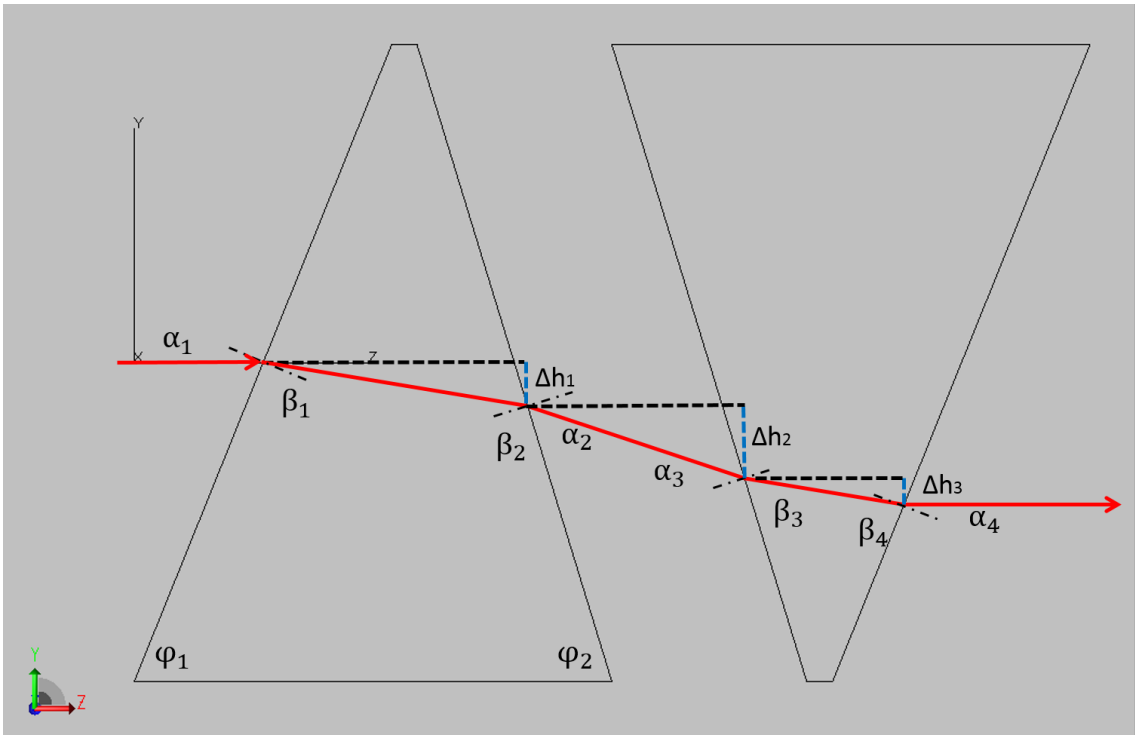

Figure 3.30: Schematic of dispersion of the DP-CASSI showing the ray propagation through the prism.

dependent on the prism angle φ_1 only and it equals to $90^\circ - \varphi_1 = \alpha_1$.

It is to be mentioned that no angular deviation was produced by the dual-prism when the dispersion happens. Consequently, if the location of the dual-prism in the system is either like the layout in UV-CASSI that the prism is placed in the collimated space among the relay lens, or at the mirror-symmetrical centre using two sets of imaging lenses serving the space-deviated spectral channels, therefore, would focus back to the same spot, although chromatic aberrations could contribute a displaced error at image plane instead of the dispersion itself; thus no dispersion would occur. The solution to this issue is arranging the prism after a re-imaging lens, similar to the layout of Double-Amici Prism. In our work, a custom relay lens serves this role. However, as discussed in the section of DA-CASSI, this kind of layout will bring unexpected aberrations in the system. This consideration will be balanced by optimising the optics in OSLO to some extent in the following section.

Considering that the relay lens helps the prism focus the image, the dual-prism tar-

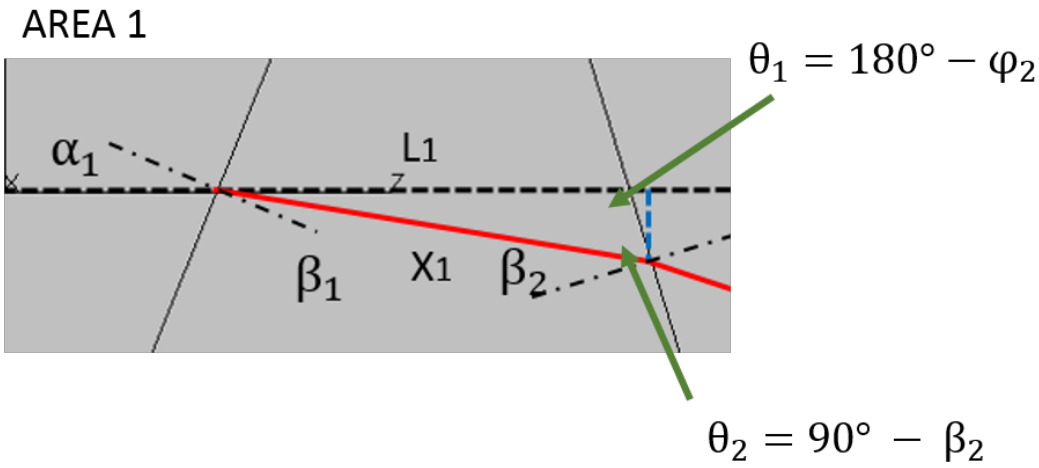

Figure 3.31: Area 1: the area where the refraction happens in the front prism.

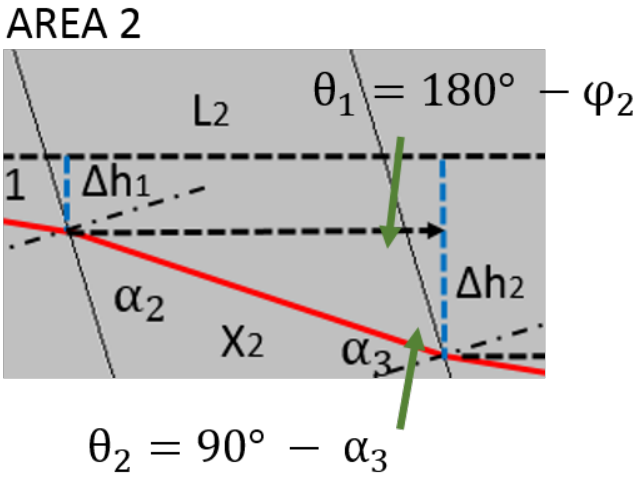

Figure 3.32: Area 2: the area of air gap between two prisms.

gets the on-axis rays after the relay lens to easily analyse the dispersion displacement as illustrated in Fig. 3.30. The dispersion process can be divided into three stages in the tangential plane as the direction facing towards reader in the figure. The three stages, Area 1 (Fig. 3.31), Area 2 (Fig. 3.32) and Area 3 (Fig. 3.33), indicate the propagation in the front prism, in the air gap and in the rear prism. Relationships between ray trajectory and the prism are described as follows,

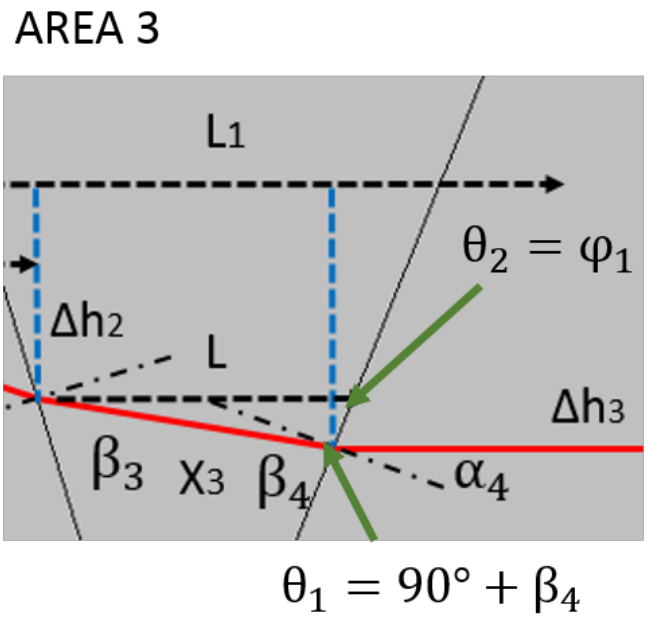

Figure 3.33: Area 3: the area where the refraction happens in the rear prism.

Area 1:

$$\frac{X_1}{\sin\,\theta_1} = \frac{L_1}{\sin\,\theta_2}, \tag{3.40}$$

$$\Delta\,h_1 = \sin(90^\circ - \varphi_1 - \beta_1)\,X_1. \tag{3.41}$$

Area 2:

$$\frac{X_2}{\sin(180^\circ - \varphi_2)L_2} = \frac{L_2}{\sin(90^\circ - \alpha_2)}, \tag{3.42}$$

$$\Delta\,h_2 = \sin(\varphi_2 + \alpha_2 - 90^\circ)\,X_2. \tag{3.43}$$

Area 3:

$$\frac{X_3}{\sin\,\varphi_1} = \frac{L}{\sin(90^\circ + \beta_4)}, \tag{3.44}$$

$$L = L_1 - (\Delta_{h_1} + \Delta_{h_2}) \times (\cot(\varphi_1) + \cot(\varphi_2)), \tag{3.45}$$

$$\Delta\,h_3 = \sin(\varphi_2 + \beta_3 - 90^\circ)\,X_1. \tag{3.46}$$

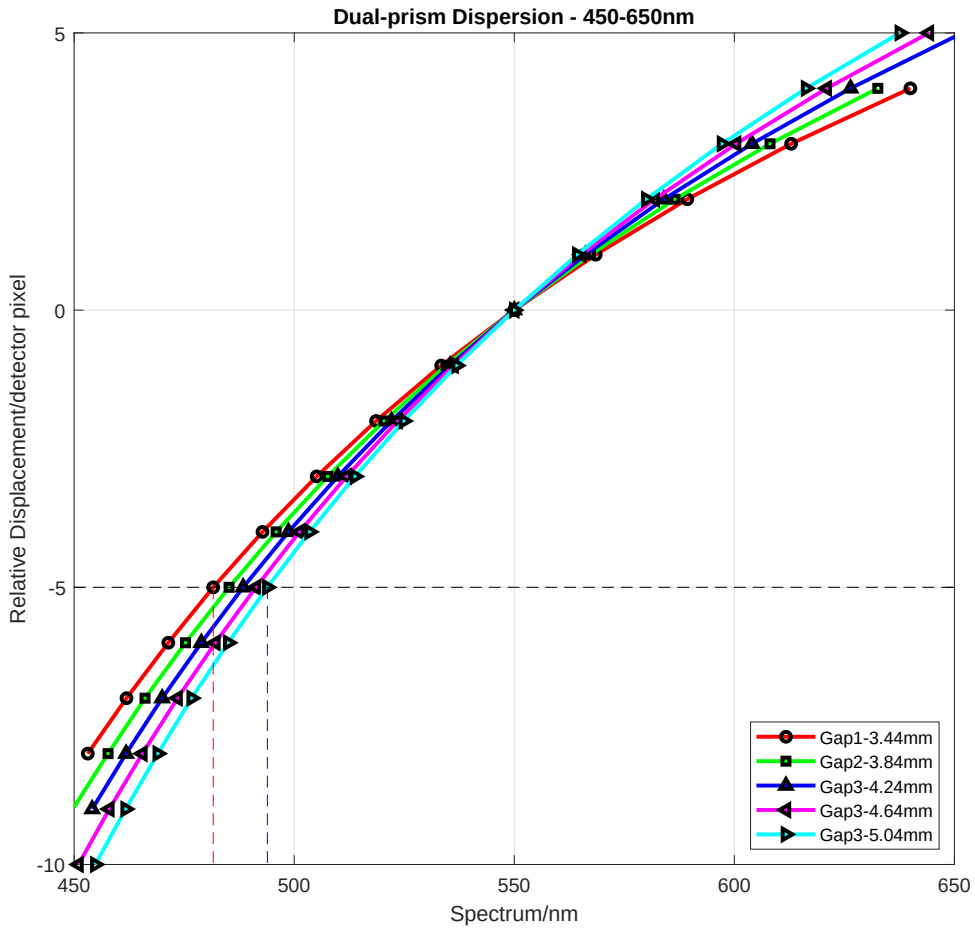

Figure 3.34: Dispersion displacement of the Dual-Prism in 5 air gaps of 3.44 mm, 3.84 mm, 4.24 mm, 4.64 mm and 5.04 mm in spectral range from 450 mm to 650 mm.

where θ_1 and θ_2 are the inner angles of the triangle area confined by the ray trajectory, axial line and prism surfaces. X_1, X_2 and X_3 denote the length of the ray trajectory between two adjacent surfaces. L_1 and L_2 denote the on-axis thickness between two adjacent surfaces. Δh_1, Δh_2 and Δh_3 denote the sagittal displacements in three areas. To the calculation of the displacements, the unknown length of the ray trajectory either inside prism or in the air gap can be deduced by applying the *Sine Law* in trigonometry multiple times with the pre-defined thickness of the prism. Therefore, the dispersion displacement is a sum of the sagittal displacements in three stages by knowing the corresponding ray trajectories.

Given a dual-prism of N-SF11 material with $\varphi_1 = 67.64°$ and $\varphi_2 = 83.48°$ at air gaps

of 3.44 mm, 3.84 mm, 4.24 mm, 4.64 mm and 5.04 mm, the specific dispersion of the dual-prism can be calculated through Eq. (3.40) - Eq. (3.44), as plotted in Fig. 3.34. The displacements were displayed in Fig. 3.34 in a spectral range 450 nm-650 nm relative to the centre wavelength of 550 nm, with the smallest shift 13 µm along the sagittal plane of image plane. Similar to the distribution of dispersion results of previous CASSIs, the dispersion data at each air gap present a curve in the figure, indicating the dual-prism still results in a non-linear dispersion displacement as a function of wavelength. Besides, with the air gap increasing, the dispersion function tends to close to the vertical line across the central point (550, 0). The number of dispersed wavelengths increases from 13 bands at Gap1 - 3.44 mm to 16 bands at Gap5 - 5.04 mm within the displacement range -10 to 5, which indicates the dispersion coverage expanding in accordance with the air gap increasing. It should be emphasised that the plot demonstrates the wavelength tuning characteristic of the DP-CASSI: the spectral shift at location of -5 pixel at detector plane is indicated by the horizontal line across the five curves when the air gap is changed from 3.44 mm to 5.04 mm. From Table 3.3, numerical results of dispersion displacement at the

Table 3.3: DP-CASSI Dispersion Displacement.

Relative Position /index	**Gap1** 3.44 mm **wv/nm**	**Gap2** 3.84 mm **wv/nm**	**Gap3** 4.24 mm **wv/nm**	**Gap4** 4.64 mm **wv/nm**	**Gap5** 5.04 mm **wv/nm**
5	*N.A.*	*N.A.*	651.8	644.2	637.6
4	640.0	632.6	626.4	621.0	616.3
3	612.9	608.1	604.0	600.4	597.2
2	589.3	586.5	584.0	581.9	580.0
1	568.5	567.3	566.2	565.2	564.3
0	550.0	550.0	550.0	550.0	550.0
-1	533.4	534.5	535.4	536.2	536.9
-2	518.6	520.4	522.1	523.5	524.9
-3	505.1	507.6	509.9	511.9	513.8
-4	492.8	495.9	498.7	501.2	503.5
-5	481.6	485.2	488.4	491.3	493.9
-6	471.4	475.3	478.9	482.1	485.0
-7	461.9	466.1	470.0	473.5	476.7
-8	453.1	457.7	461.8	465.5	469.0
-9	*N.A.*	449.7	454.1	458.0	461.7
-10	*N.A.*	*N.A.*	*N.A.*	451.0	454.8

horizontal line in Fig. 3.34 show the wavelength shifts from 481.6 nm to 493.9 nm by 12.3 nm with air gap increment of 1.6 mm, which results in a wavelength-tuning value of $\frac{12.3\ nm}{1.6\ mm} = 7.69\ nm/mm$ at this point. In comparison with the short wavelength region, the wavelength at 4 pixel decreases from 640 nm to 616.3 nm by 33.7 nm. It can be concluded that overall spectral resolution turns better from 14.37 *nm per channel* (186.9 nm for 13 channels) at Gap1 to 11.4 *nm per channel* (182.8 nm) for 16 channels at Gap5.

3.4.3.2 System Layout

The relay optics for the Dual-Prism CASSI (DP-CASSI) was started with a typical structure of Cooke triplet, the optimisation of which was conducted by the built-in function in OSLO. The goal of the optimisation is to achieve a minimal of merit function that is a sum of weighted mean squared error between the expected value and the operands relevant to the optical parameters of interest, i.e. the Seidel Aberration and first-order parameters. The optimisation tradeoff the aberrations among three wavelengths, i.e. 550 nm, 450 nm and 650 nm, to optimally obtain three dispersed spots focused at image plane. The opti-

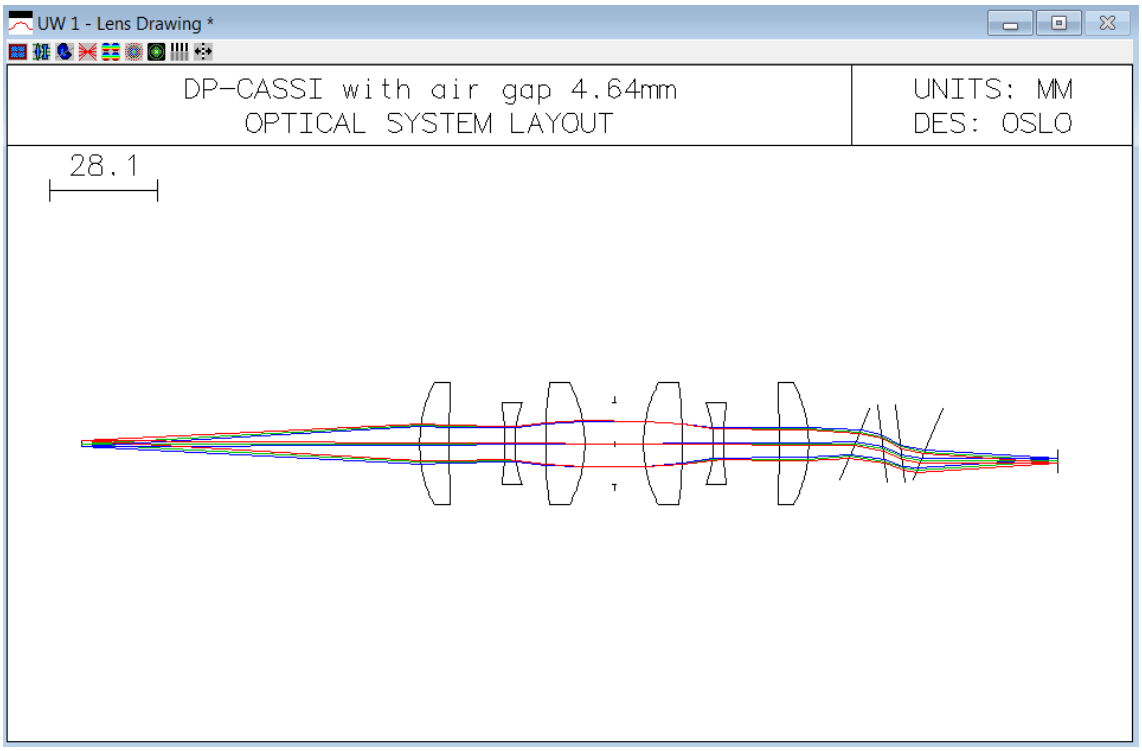

Figure 3.35: Ray diagram of the dual-prism system optics.

mised layout for air gap 4.64 mm shows the on-axis and off-axis rays from a small target of object height 0.832 mm, compared to a total track of 253.25 mm, propagating through the DP-CASSI in Fig. 3.35. Figure 3.36 presents zoom-in result at image plane when on-axis source of multi-bands propagates through the system, clearly demonstrating the dispersion happening. The evaluation result combined with spot diagrams in Fig. 3.37 and MTF diagrams in Fig. 3.38 shows the pros and cons of the DP-CASSI: the shape of spots are highly symmetrically with the gap between tangential MTF and sagittal MTF less than 5%, compared to more than 10% gap in the DA-CASSI which used the same layout while the main issue is the poor resolution, averagely 10 *lp/mm* across three wavelengths, which is regarded as the tradeoff to obtain the capability of tuning wavelengths. For the proof-the-concept DP-CASSI, it is believed that the system is theoretically feasible and the resolution can be enhanced by further upgrading the fore optics, e.g. utilise more optics and choose other glass materials or adjusting the optical layout, e.g. replace the refracted optics with the reflected optics.

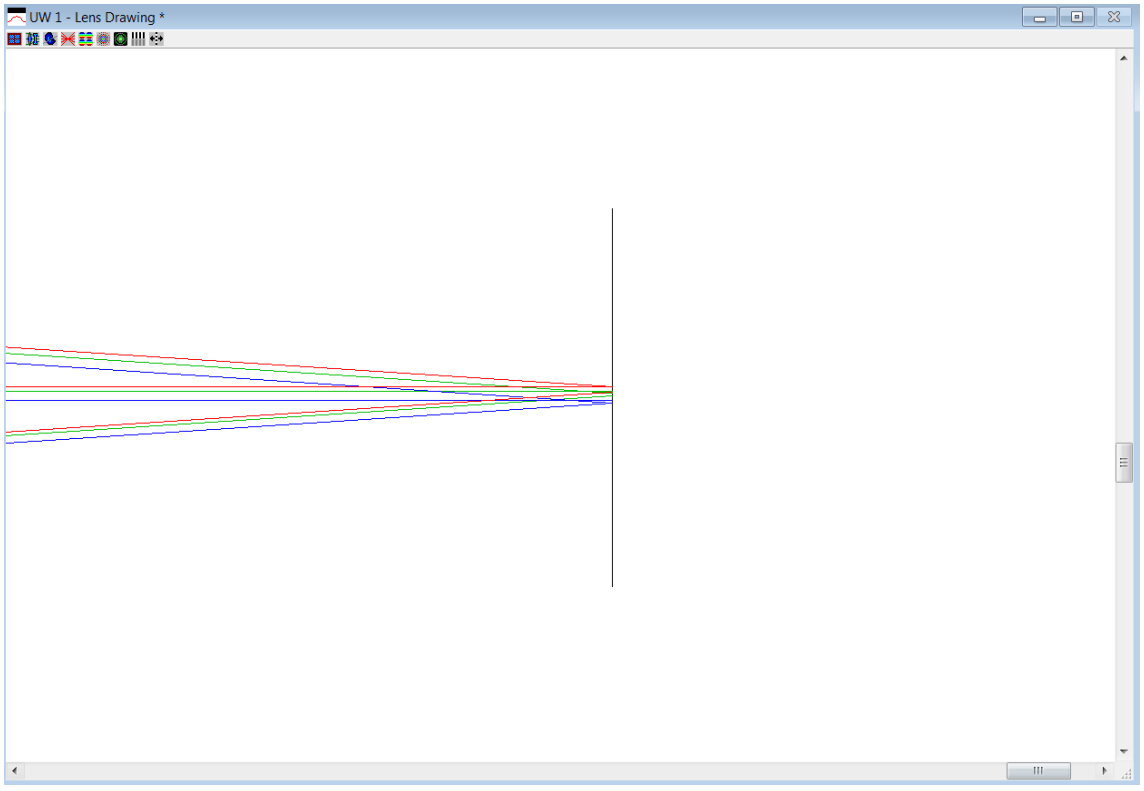

Figure 3.36: The zoomed-in ray diagram at detector of the DP-CASSI.

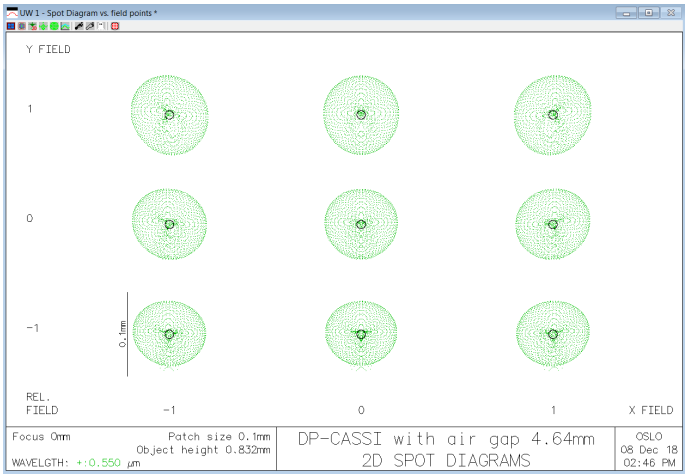

(a) Primary wavelength 550 nm

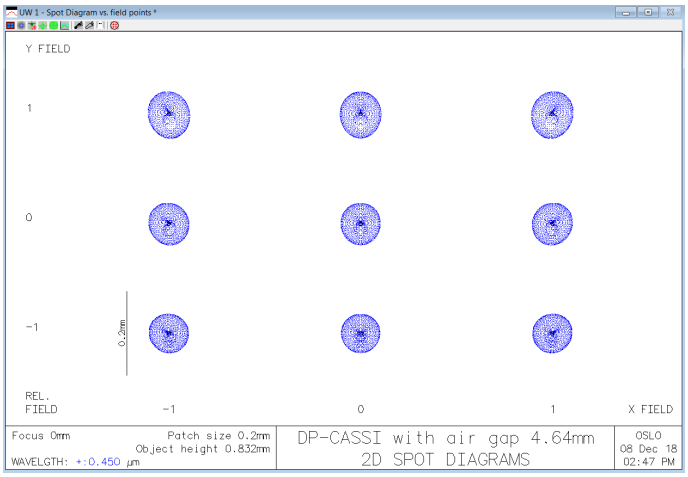

(b) Second wavelength 450 nm

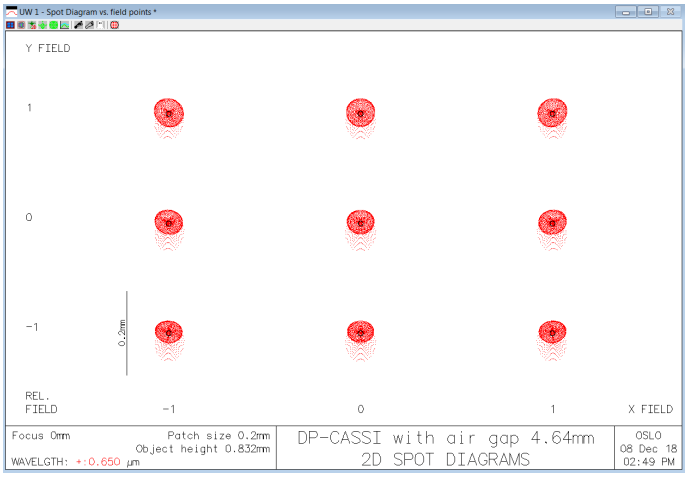

(c) Third wavelength 650 nm

Figure 3.37: Spot diagrams of DP-CASSI.

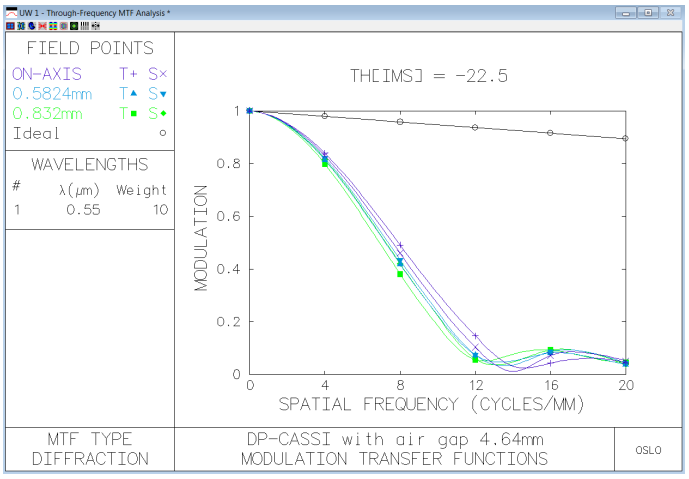

(a) Primary wavelength 550 nm

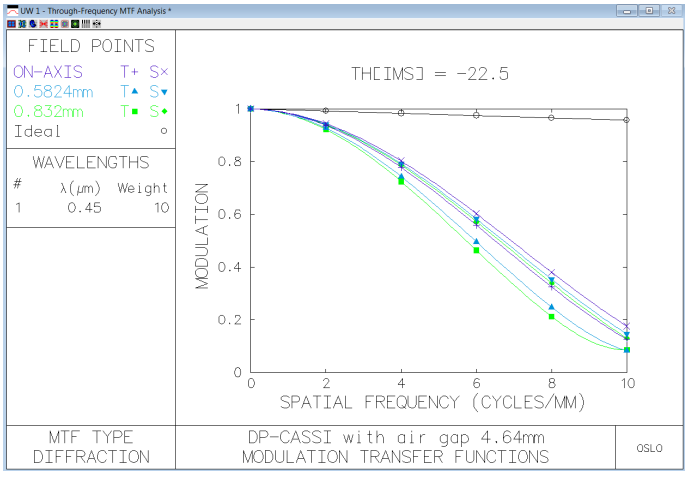

(b) Second wavelength 450 nm

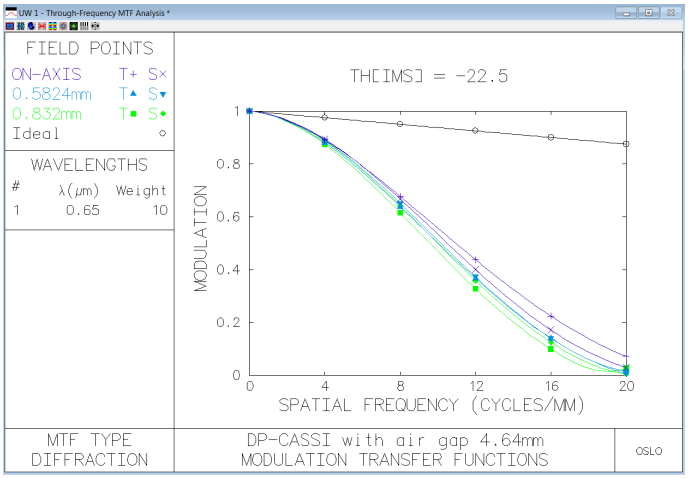

(c) Third wavelength 650 nm

Figure 3.38: Monochromatic MTF diagrams of DP-CASSI.

Chapter 4

SYSTEM SIMULATIONS

Following system design and analysis in the previous chapter, three systems, SP-CASSI, UV-CASSI and DP-CASSI, will be 3D modelled in ray tracing software TracePro to validate the performance of the optimised SP-CASSI and the proposed DP-CASSI, plus the published UV-CASSI as a comparative study. Like other illumination software LightTools, CODE V and ASAP, TracePro conducts any interaction, including reflection, refraction, absorption and scatter, between objects and virtual rays that can be custom defined from several importance samplings up to a very large scale of grid rays. The reason to conduct ray tracing simulation for optical systems is that simulated results are able to help researchers or designers to intuitively predict how the system would behave in a real scenario without practical implementation in the first place, which could lead to ascertaining any potential errors from the design and avoiding further system failure in manufacturing. Because of that, setting up a synthetic environment with artificial targets for the CASSI framework is able to provide us with a further understanding of the CASSI framework and allow researchers in the field to repeat, modify or validate the simulated results in the future. Apart from the aforementioned advantages of using optical software, the shortcomings of the simulation should be aware and addressed as well: the simulated system is an extreme and ideal case of a physical system which would be affected by various factors, such as manufacturing, mechanical control and cost.

4.1 TracePro Environment

TracePro has a user-friendly interface especially convenient for beginners. Rather than using any command lines to communicate with the software, TracePro narrows down the program to only two points for users to be familiar with, *Object* and *Light Source*. All the ideas coming from users will eventually be projected onto those two and TracePro will operate relevant actions at the background.

Object, also called Solid Model in TracePro, is commonly designed in 5 primitive solids, *Block*, *Cylinder/Cone*, *Torus*, *Sphere* and *Thin Sheet*, to support basic elements modelling at the beginning of a new project, wherein *Thin Sheet* is a 2D structure and others are 3D. The feature of the 2D structure of Thin Sheet could be the convenience to extend any 2D geometry into 3D geometry especially in the design of some irregular structure. It is much easier if one starts with transverse projection of target and then "sweep" the surface by increasing its thickness, which is exactly the means to build rotation-unsymmetrical prisms. Besides, the computational speed of the software depends on the number of interactions between rays and objects/surfaces. 2D structure would tremendously contribute to reduce the computational resources used for simulation

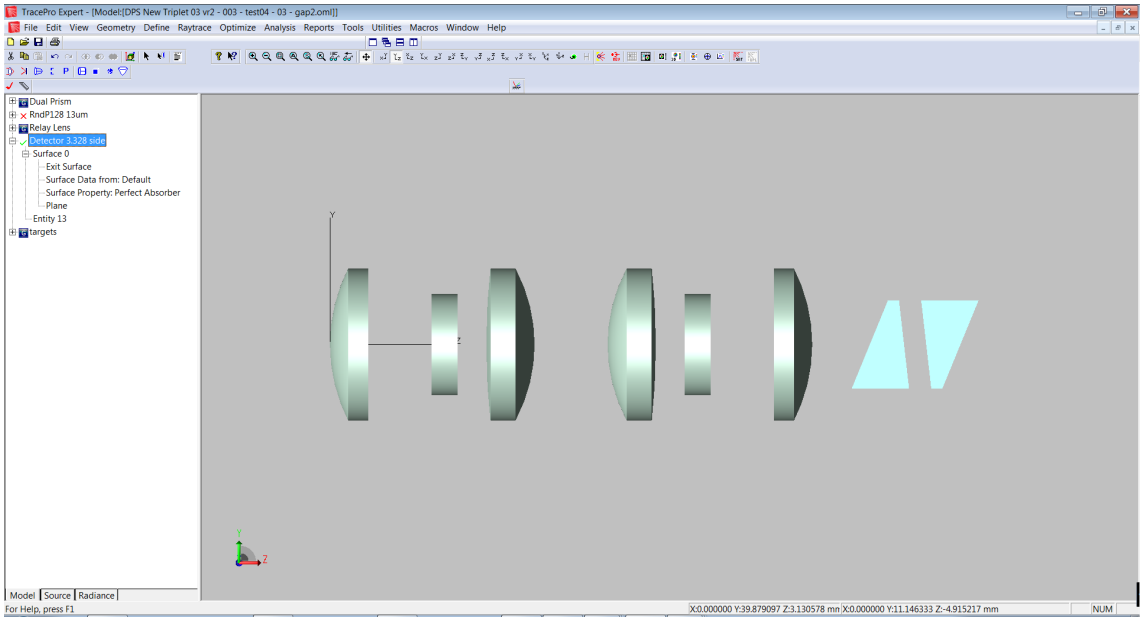

Figure 4.1: Overview of TracePro interface.

to further shorten processing time. This advantage was realised during the time translating coded aperture mask in 3D block to 2D thin sheet. In addition, the role of the coded aperture mask is to block light or not, spatially representing “1” and “0” and inner part is not considered as long as the light would be totally absorbed by the surface of the mask. As for lens elements, the point is to have the light refraction happen inside the lens, which is apparently not an option to apply thin sheet model.

Any one of interactions such as reflection, refraction, absorption and scattering involves the surface of object or inside body of object. Surface property defines all the actions dealing with the surface only. It is crucial to the coded aperture mask and artificial targets, which are the only two elements to be considered with the reflection during the entire simulation. That will be detailed in the following section. Material property, comparatively easy to understand, defines transmissive behaviour of rays during the propagation through object, which is only lens to be considered in our case. Moreoever, TracePro provides a large variety of glass materials from main glass manufacturers, e.g. SCHOTT, OHARA and Corning, sufficient for users to choose.

Illuminating rays have three formations defined in TracePro: Grid Source, Surface Source and File Source. Grid source defines a grid pattern bounded in a grid boundary. The grid pattern emits all the rays sampled within the grid boundary (either in rectangular or annular area), as collimating, converging or diverging at an orientation as a whole. Surface source is more used as simulating illuminating light source with limited sampling number of broad bands from a surface while lack the flexibility in adjusting wavelengths required for simulation. File source is a free form for building custom light source. By creating coordinates of emitting points and end points, normal vector, up vector and flux as an array of ray parameters, light source could be processed dramatically efficient than the built-in source. Our simulations are mainly based on file source to create synthetic scenario.

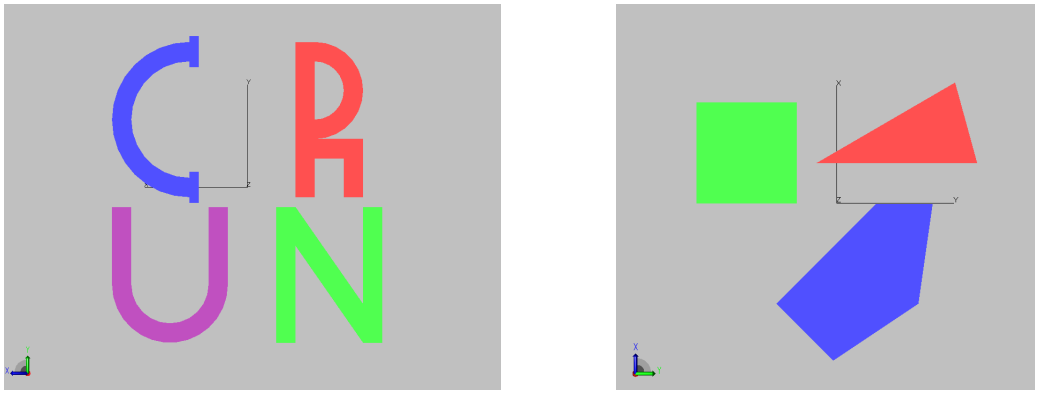

(a) Front view of four targets, “C”, “R”, “U” and “N”

(b) Front view of three targets, Square, Pentagon and Triangle

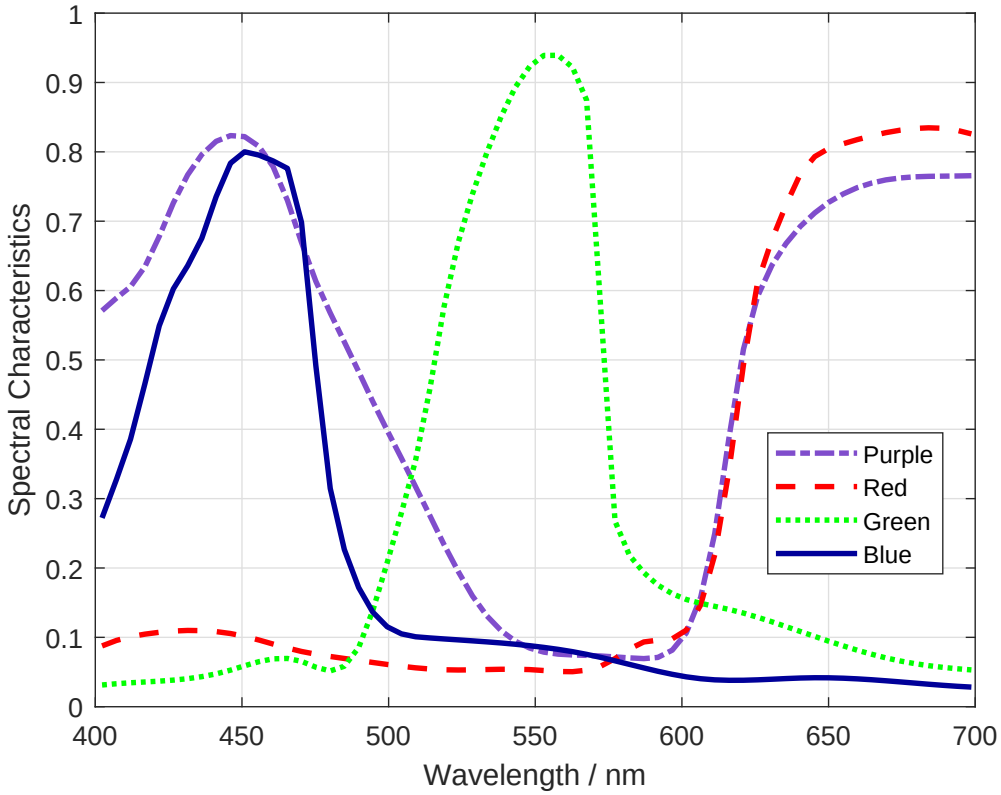

(c) Spectral characteristics for artificial targets illustrate green targets in (a) and (b) applied with Green property, blue targets in (a) and (b) applied with Blue property, red targets in (a) and (b) applied with Red property and purple targets applied with Purple property.

Figure 4.2: Artificial targets were created by TracePro in 3D mode for the detection of the SP-CASSI, UV-CASSI, DP-CASSI with custom spectral characteristics applied.

4.2 Components Modelling

4.2.1 Artificial Targets

Two groups of Artificial Targets were used in our simulations. A set of four characters "C", "R", "U" and "N" shown in Fig. 4.2a was defined with four distinguishable optical characteristics in Fig. 4.2c representing blue, red, purple and green colours, which was used in the simulation of the SP-CASSI and UV-CASSI. The other set of geometrical shapes Triangle, Pentagon and Square shown in Fig. 4.2b adopted Red, Blue and Green property from the curves of optical characteristics, which was used in the simulation of the DP-CASSI. All the targets are limited in an area of 1.664 mm $\times$ 1.664 mm to accommodate the size of the coded aperture. Meanwhile, the reason of setting the mask size to 1.664 mm is that would reduce the number of tracing rays in the simulation to save the computer processing time. Note that the optical characteristics were custom created in Matlab and imported in TracePro as Surface property, sampled in Matlab and later interpolated by the program to respond those wavelengths beyond sampling wavelengths.

4.2.2 Coded Aperture

The code word of *Random Pattern* was generated by randomly shuffling the indices of a core pattern for certain times, e.g. $\begin{bmatrix} 0 & 1 & 0 & 1 \\ 1 & 1 & 0 & 1 \\ 0 & 1 & 0 & 0 \\ 1 & 0 & 1 & 0 \end{bmatrix}$ which set the weight of openings in one pattern, with 1 for the opening and 0 for the closing. The shuffling was achieved in Matlab by the built-in function *randperm* The resulting partition of the core pattern is able to control the area of consecutive zeros in the pattern not being too large to reconstruct image. The pattern used in our simulation shuffled and stacked up the core pattern for 32 times to form a complete pattern of 128 $\times$ 128 and can be further extended to a larger scale for the needs of an application, as a visual example shown in Fig.4.3. In the simulation, physical size of coded aperture was adjusted depending on the requirement of dispersion of system accordingly.

The pattern is defined as a Row-Column with matrix index in Matlab while a 3D

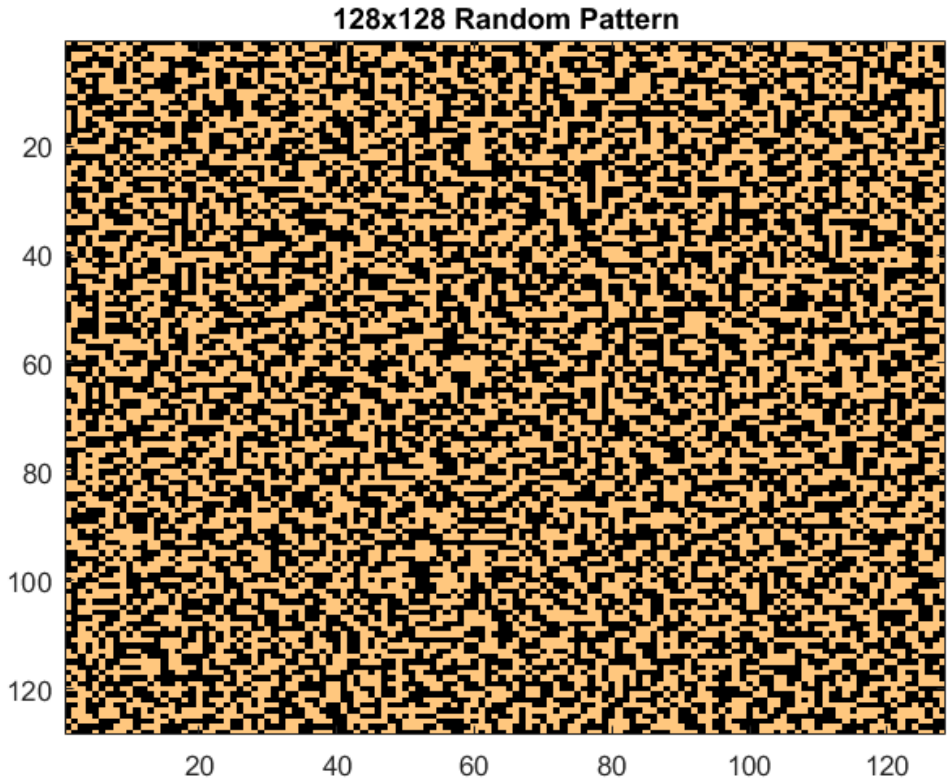

Figure 4.3: An example of 128×128 Random Pattern.

geometrical object as the entity of pattern in simulation is required to be translated. The process of the translation from Matlab to TracePro includes that, set matrix indices of element *zero*, which indicates the opaque area, as central position in the minimum unit element with its side length equal to smallest feature of coded aperture. The initial mask was modelled in 3D structure and it was figure out that it was the reason causing an extremely long time for simulation. Later on the mask was generated in thin sheet model via macro program in *Scheme Language* to reduce redundant surfaces and processing time has dropped from a week to several hours.

4.3 Single-Prism CASSI

4.3.1 Layout of SP-CASSI

Following the prescription of Single-Prism CASSI designed in Sec. 3.4.1 by OSLO, the individual components in such sequence, i.e. an objective lens, a coded aperture mask, front imaging lens, equilateral prism, back imaging lens and plane detector, were placed in TracePro as depicted in Fig. 4.4.

The vertex of the front surface of the front imaging lens was placed at origin of TracePro coordinate system as a system start point at which positive Y direction represents the direction of upper vector of the system and positive Z direction represents the direction of ray propagation. In other words, light rays go from the left to the right in Fig. 4.4. Despite that the design in OSLO did not present the objective lens, any objective lens that is able to provide a focused image at the coded aperture plane with image N.A. of 0.125 and not much contribution to aberration could serve for the main body of SP-CASSI. Note that no matter how fast F-number of objective lens can achieve or how large image N.A. can be, the system performance is limited to the coded aperture as an aperture stop. Since the patent as the base of the front imaging lens satisfies those conditions very well, a replica of the front imaging lens was reversing placed at double distance of where coded aperture

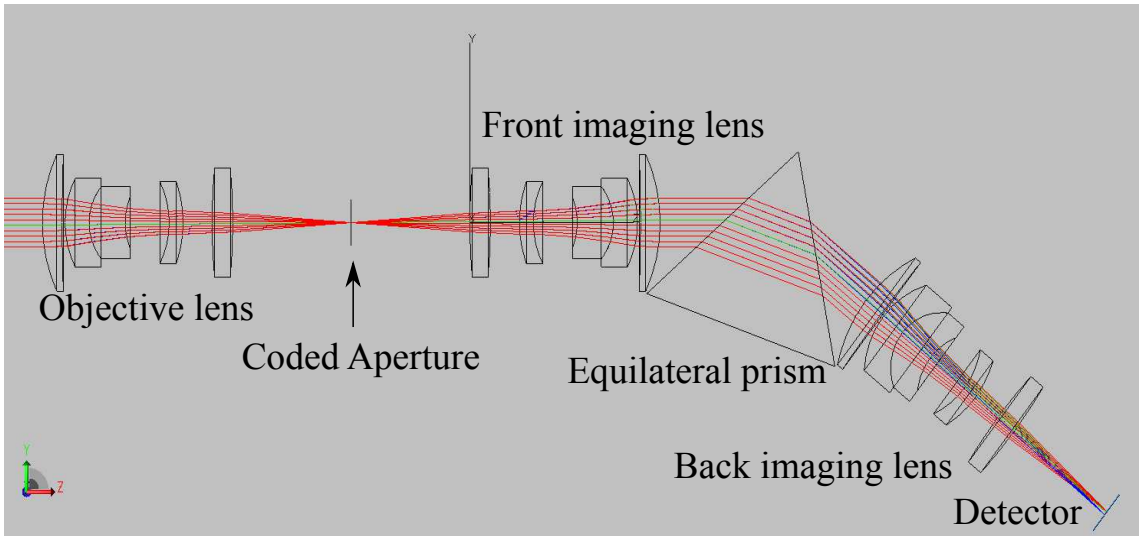

Figure 4.4: Overview of Single-Prism CASSI modelled in silhouettes mode in TracePro.

is, in other words, coded aperture lies on the plane where image plane of the objective lens and the object plane of the front imaging lens are intersected.

4.3.2 Synthetic Scenario

A synthetic scenario is required to be built up for collecting the results of interaction between the designed system and illuminating rays. The basic idea of ray tracing simulation is that imaging system acquires the reflected rays from a target, under certain amount of illumination across the spectrum of interest. While in most experimental conditions, the objective lens plays a great role in forming a focused image through collimated rays emitted from a target at long distance (compared to focal length of imaging system) or even at infinity. The collimated rays converge to the entrance of imaging system with a certain range of FoV to composite a 2D image instead of a single point. Every single one of the image pixels is actually corresponding to an object source at a specific azimuth angle in object space. A 128×128 image, therefore, could correspond to 128×128 azimuth angles in the object space. Due to the property of grid source in TracePro that it can only shoot parallel/convergent/divergent rays at one direction per grid source. To such a number of azimuth angles, it is unachievable that tracing those rays within one

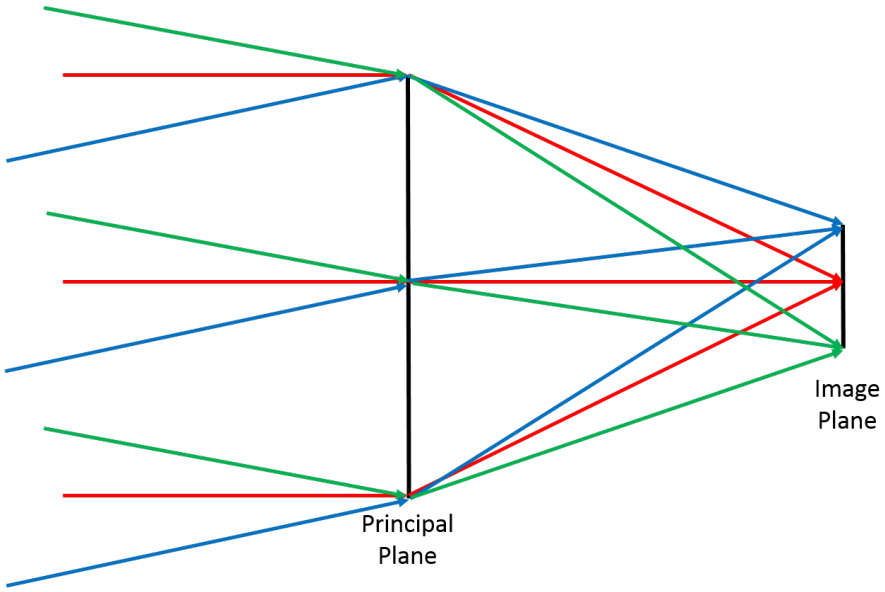

Figure 4.5: Conventional ray propagation should bend at principal plane.

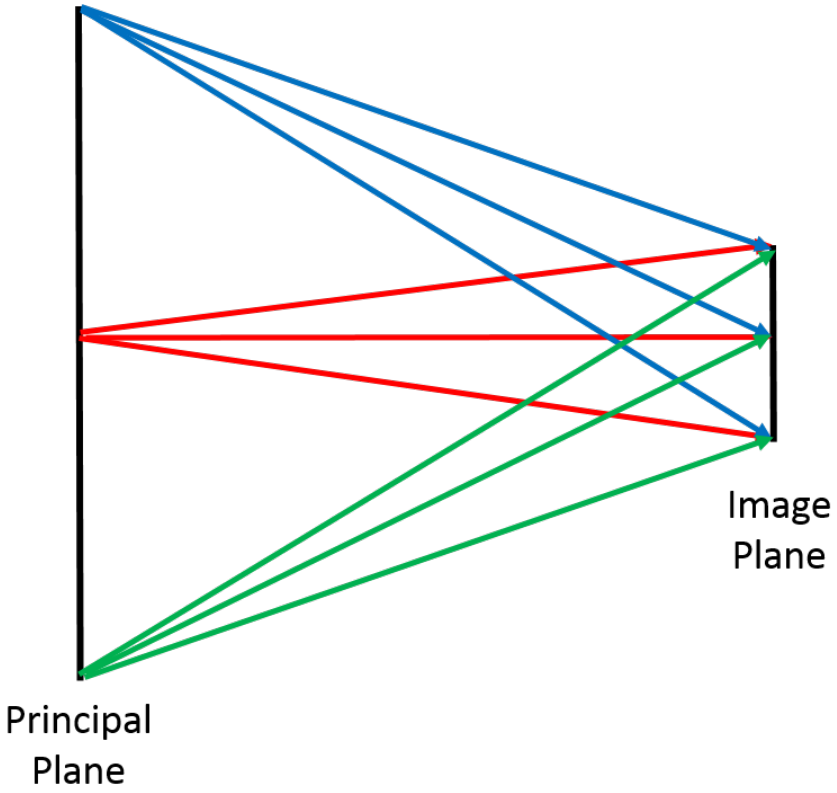

Figure 4.6: New ray tracing strategy to simplify the objective lens by emitting directly from the principal plane.

single grid source. Instead, it has to consume a large amount of computer source to generate 128×128 number of grid sources. Consequently, setting 128×128 number of grid sources could crash the software during the processing. In order to successfully realise the ray tracing from a target, an alternative was acted due to the fact that in paraxial approximation one thin lens can be simplified to a principal plane through which all collimated rays from same azimuth angle would propagate to focus to a corresponding point at image plane, in other words, a focused point at image corresponds to many points at principal plane. Meanwhile, if we stand in image space and look towards object space, emitting rays from all the points on the image could converge to a single point at principal plane under homogeneous condition. Applying this concept to a thick lens or even a complicated optical system, two principal planes are introduced by the oncoming direction of collimated rays from the right side and the left side due to the thickness of system. The rear principal plane is more often used for studying a lens system as it is defined by the

incident rays from the left side following the conventional direction. The distance from this plane towards image plane is defined as Effective Focal Length. As mentioned above, when we do reverse-ray tracing (from right side to left side), emitting single ray from all image points at image plane, e.g. 128×128 points, that would converge to a point at second principal plane. Setting a divergent point source at second principal plane in the right ray tracing direction (from left side to right right), therefore, manages to obtain the 128×128 image. To be summarised, this method replaced the conventional way that trace the rays forming a point at image plane one by one, with tracing the rays forming multiple points at image plane but reverse-converging to a point at principal plane once and for all.

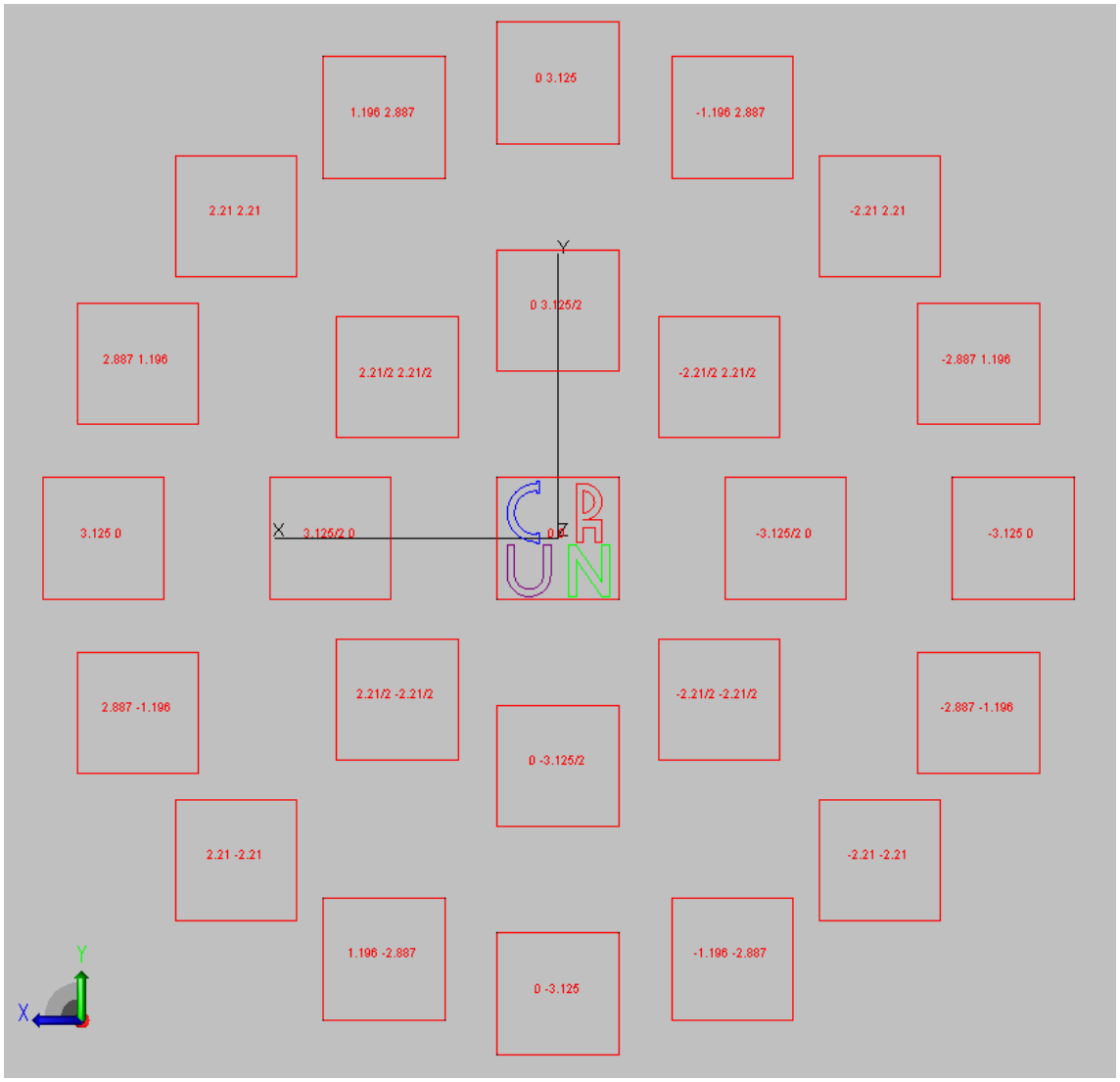

Figure 4.7: 25 sampling target sources for SP-CASSI simulation.

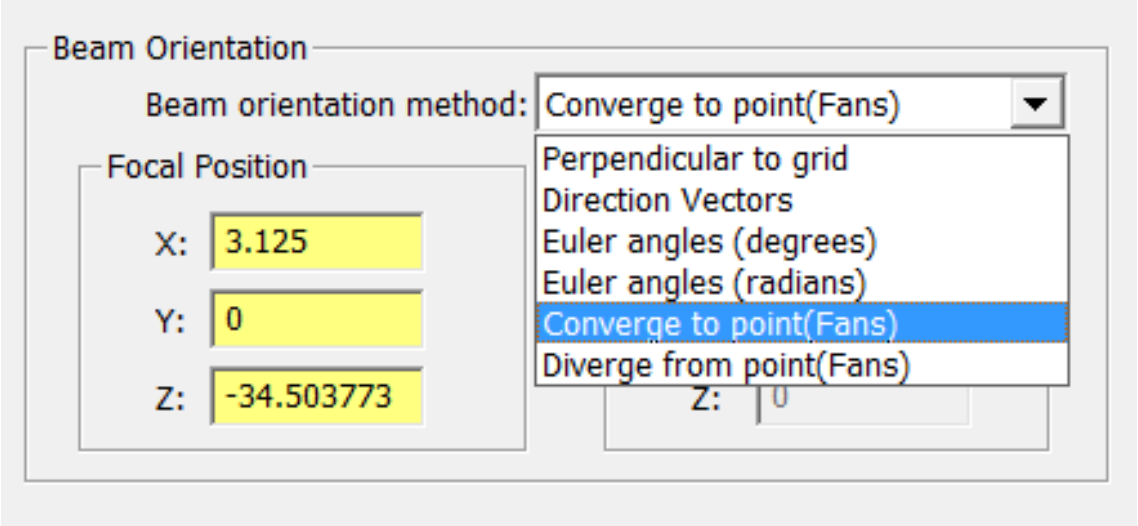

Figure 4.8: Beam orientation settings in TracePro.

It should also be noticed that the drawback of this method missed the fact that the realistic principal plane is a spheric surface instead of a plane. The simulated image, therefore, after the principal plane becomes an ideal image free from such aberrations as Spherical Aberration, Distortion and Astigmatism. Considering that this work mainly focuses on the performance of the main body of CASSI (imaging/relay lens plus dispersive prism), we could accept a perfect objective lens in synthetic environment. However, the effect of how good an objective lens affects on the entire system when at the stage of prototyping cannot be negligible. In the previous example of 128×128 image simulation, every single point at image plane receives only one ray, which could just basically achieve "one image" in computer simulation. To be more realistic, increasing the number of the divergent point source at second principal plane is of great essence to contribute to the diversity of angles of oncoming rays in a single point. For the settings of the simulation of SP-CASSI, 25 sampling points have been chosen at the second principal plane of the objective lens used for SP-CASSI, as shown in Fig. 4.7. This plane is limited to the aperture size of entrance pupil as a radius of 3.125 mm and locates at 25 mm away from image plane. As discussed in previous section, note that the aperture diameter of system determined by the entrance pupil is set to 6.25 mm for the sake of F/4 system. To those 25 sampling points, we uniformly selected $\omega = k \cdot \pi/8, k = 0, 1, \ldots, 15$ circular angles at principal plane where

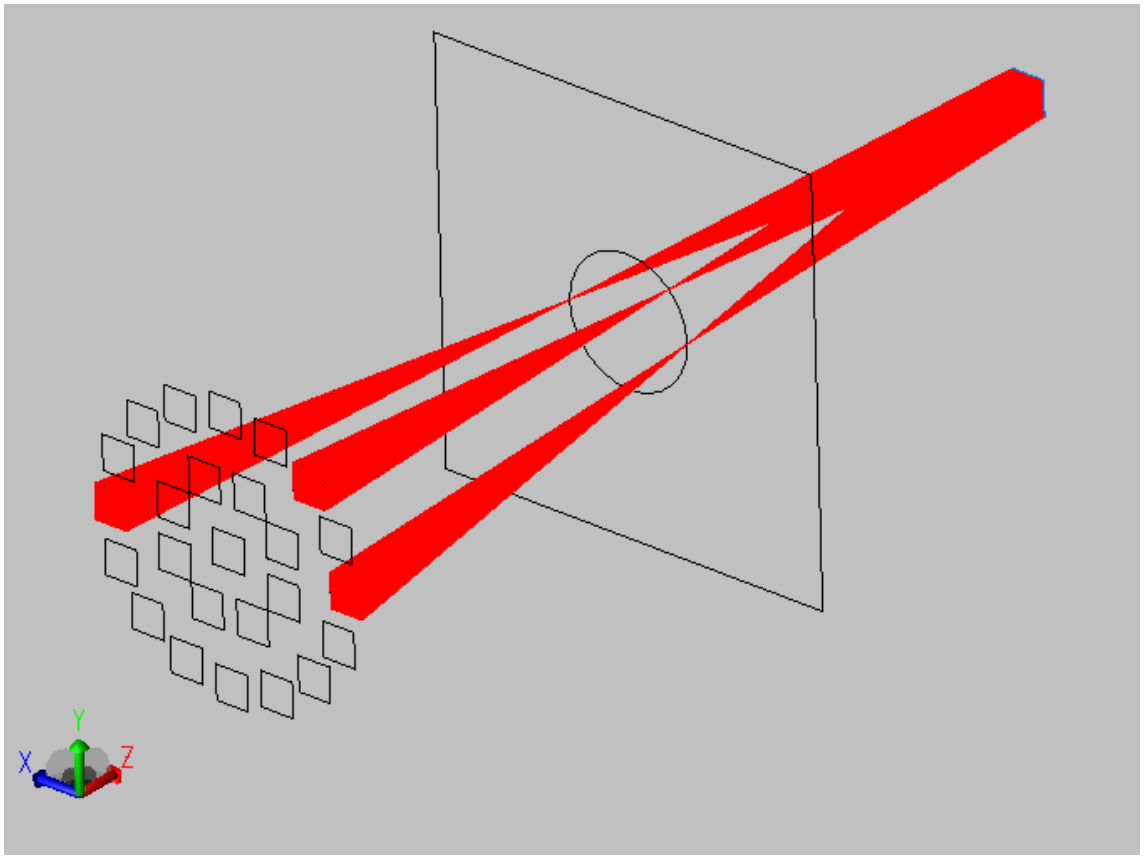

Figure 4.9: Simulate sampling point source. Note that the Fans in settings means the grid source emit or converge as a fan area instead of a single point or parallel rays.

two sampling points (maximum length and half length) were chosen at even angles and one sampling point (maximum length) was chosen at odd angles, plus a central sampling point. The point source is created using the basic built-in function called “Grid Source”. The default beam orientation “Perpendicular to grid” in the settings of “Beam Setup” can be changed to “Converge to point(Fans)” as shown in Fig. 4.8. The focal position is set to the location of those 25 sampling points. By doing this, a convergent ray fan would go through the sampling point and diverge from that point to spread in the space. However, due to that principal plane is just a virtual plane for locating sampling points, the geometry rays could not bend without any lens between the principal plane and image plane. Therefore, in order to achieve a 128×128 image at image plane, the grid source for generating sampling point source locates at which mirror-symmetrically rotate the image as the principal plane. Set the grid source to the same size as the required size of image and

increase the grid sampling rate to 256×256 to ensure the quality of image. The resulting source in Fig. 4.9 shows 3 out of 25 sampling point sources emitting from -25 mm to the principal plane and striking the image plane at 25 mm to the principal plane. Those 3 grid sources converge to the point $(3.125, 0)$, $(-3.125, 0)$ and $(-2.21, 2.21)$ at the principal plane.

4.3.2.1 Artificial Targets

After solving the problem of building up source rays for imaging, the system still requires the rays from target with specific physical geometry and distinguishable spectral characteristics to truly verify the capability of compressive snapshot imaging. Four synthetic

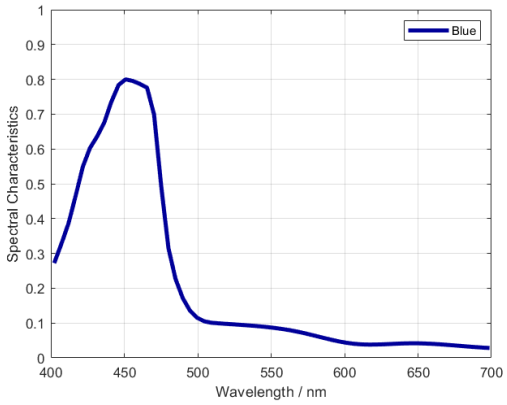

(a) Custom spectral characteristic - Blue

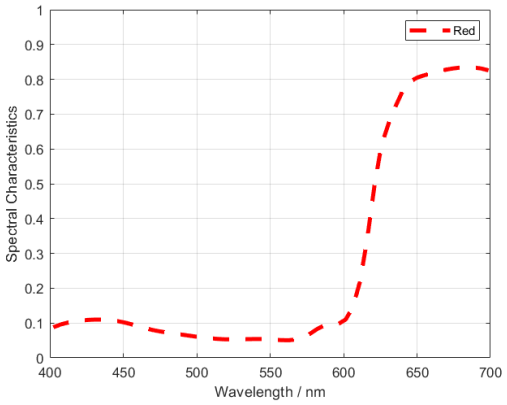

(b) Custom spectral characteristic - Red

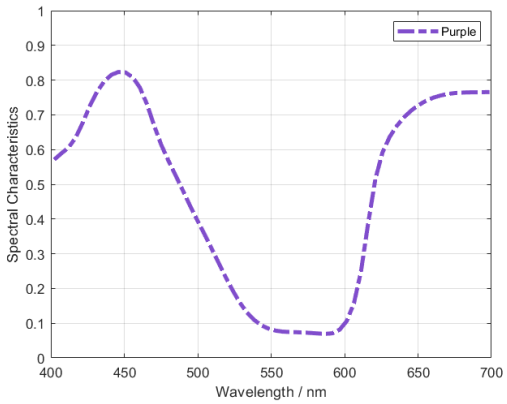

(c) Custom spectral characteristic - Purple

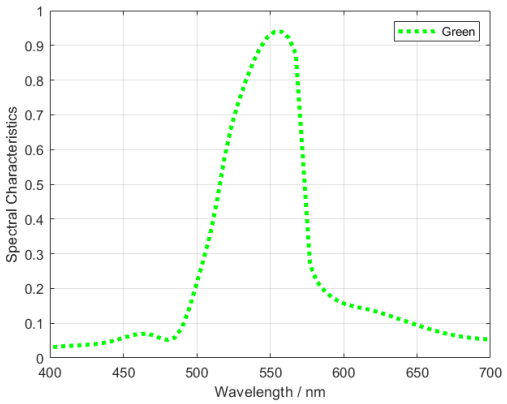

(d) Custom spectral characteristic - Green

Figure 4.10: Custom spectral characteristics for synthetic targets, “C” (upper left), “R” (upper right), “U” (lower left) and “N” (lower right).

targets, therefore, were designed in character-shape pattern, “C”, “R”, “U” and “N”, using “Thin Sheet”, one of 5 built-in “Primitive solid” types in Fig. 4.2a, which offers no thickness but remains the surface property for reflection and absorption. The spectral characteristics applied for each one of synthetic targets were custom created in Matlab with their own spectral peaks distinguishable from each other. Concretely, the spectral curve Blue for the target “C” has a range from 430 nm to 470 nm with high reflectance above 50% and 500 nm afterwards with 10%, corresponding to the blue colour in spectrum. The spectral curve Red for the target “R” stays at low reflectance around 10% from 400 nm until at 600 nm dramatically rises up to 80%, corresponding to the red colour in spectrum. The spectral curve Purple for the target “U” contains uniquely two peaks around 80% in 450 nm and 650 nm afterwards while stays below 50% in the most of spectrum (500 nm to 630 nm), corresponding to the purple colour in spectrum. The spectral curve Green for the target “N” has the reflectance above 60% across 520 nm to 560 nm and remains below 40% apart from that, corresponding to the green colour in spectrum. Apart from managing to achieve multispectral synthetic targets required by the system, there is also a system requirement in space domain that image of synthetic targets formed by the objective lens could highly match the coded aperture pattern to realise the “punch”. Using the method discussed above is able to realise the matching between image of target and coded aperture pattern while the problem is how to collect the reflected information from the synthetic targets since the source rays virtually emit from the principal plane. The solution is a “Twice Reflection” method using built-in function “Exit surface”. Briefly, this function allows users collecting rays at an intermediate surface during the propagation and continuing the ray tracing by importing the collected ray data on another surface. The surface designated to collect rays is set to “Exit surface” and exports rays either in propagating direction or in reverse propagating direction. By applying this method, the targets are modelled within the scale of the coded aperture (1.664 mm $\times$ 1.664 mm) as the anticipated image focused onto the coded aperture and set to “Exit surface” for collecting those rays that come from 25 sampling point sources and would reflect from the targets

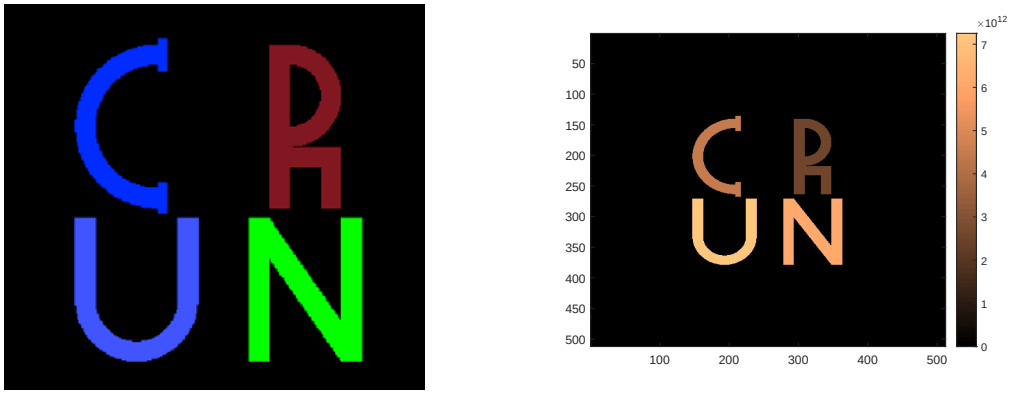

(a) Target source shown in "RGB color" mode (b) Target source shown in Matlab

Figure 4.11: Custom target sources used to project onto coded aperture, containing 32 spectral bands in 256×256 pixels.

in reverse propagating direction, since we need to know how many rays reflect, which is called *First Reflection*. Then emit the collected ray data at which coded aperture is and collect those rays at the location where 25 sampling point sources emit, applying "Exit surface" on 25 surfaces as 25 sampling point sources lead to 25 azimuth angles, which is called *Second Reflection*. To be more realistic for the simulation, 32 spectral bands from 450 nm to 650 nm were used to uniformly illuminate the targets. After applying the aforementioned process and collecting the ray data, Fig. 4.11 shows the final image of the target source to be further projected onto the coded aperture, wherein $25 \times 256 \times 256 \times 32$ total rays with 1 flux per ray were filter out at some point by the targets.

4.3.3 SP-CASSI Simulation Results

For the TwIST algorithm used to reconstruct images, there are two inputs to be collected in the simulation: the measurement and the calibration data. The measurement is detected by system detector as a multiplex dataset in 2D spatial dimension. The calibration data is collected using monochromatic light source to illuminate the coded aperture directly and the resulting projections onto the system detector. The details to realise those two steps will be explained as follows.

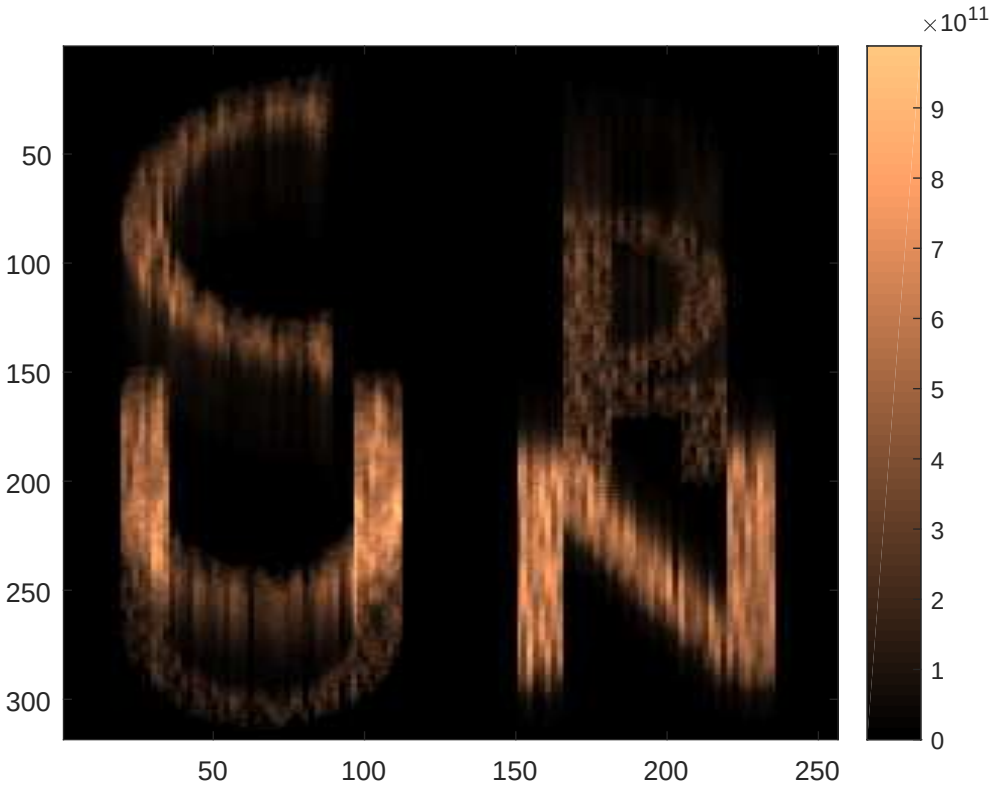

Figure 4.12: Detector measurement collected from TracePro were cropped to an image of 256×318 pixels displayed in Matlab. The raw measurement were pixelated by a 512×512 detector with 6.5 µm pitch.

4.3.3.1 Measurement Acquisition

The measurement is the result by directly projecting target source onto the coded aperture, following the description in last section. Since the dispersion capability of single prism was designed for 32 coded aperture pixel shift in spatial domain with 1 coded aperture pixel equal to 2 detector pixels, the resulting measurement was detected as a 256×318 pixel image, wherein $256 + (32 - 1) \times 2 = 318$, by a 512×512-pixel detector with smallest feature 6.5 µm. Figure 4.12 shows the overall dispersion area of the measurement cropped from 512×512 raw data, the region of which is *Row* 123 to 440 and *Column* 129 to 384. From Fig. 4.13, it is more clear to see that a shaded area of each character was shifted along the vertical direction by the effect of dispersion, where the raw image was upside down for a better visualisation, resulting in short wavelength at top and long

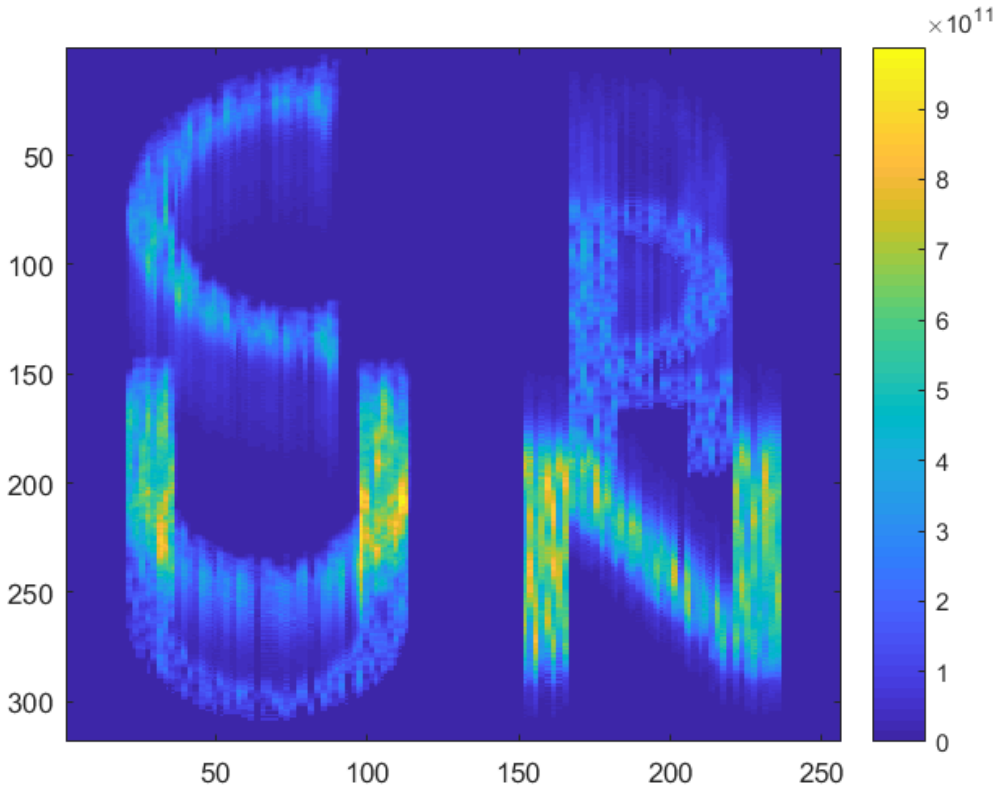

Figure 4.13: Detector measurement shown in intensity.

wavelength at bottom. Moreover, compared to the reference of their own spectral characteristics, both character “C” and character “R” have their own peak spectral response at either short wavelength or long wavelength and thus their intensity changes gradually. Compared to “C” and “R”, character “U” and “N” have significant brightness due to the fact that for “U” its two peaks at short wavelength and long wavelength overlapped each other and that for “N” higher spectral response are more centralised in middle wavelengths. Moreover, it can be noticed that the partial overlapping exists between too close characters, i.e. long wavelength in “C” with short wavelength in “U” and long wavelength in “R” with almost middle wavelength in “N”. That is due to large dispersion displacement.

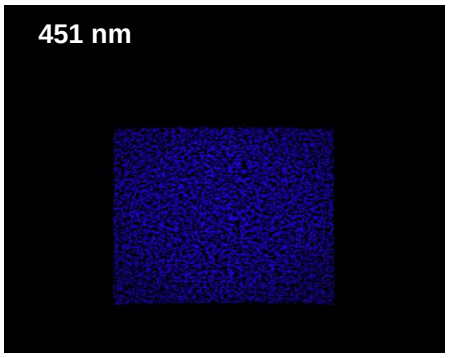

(a) calibration 451 nm

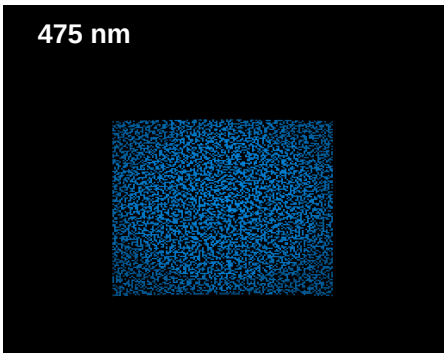

(b) calibration 475 nm

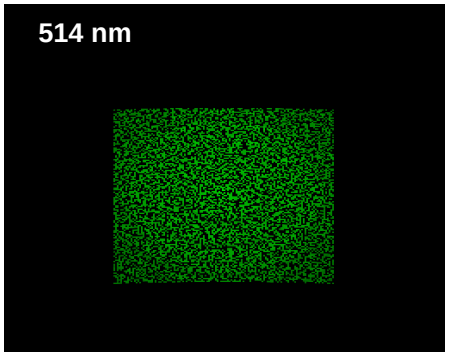

(c) calibration 514 nm

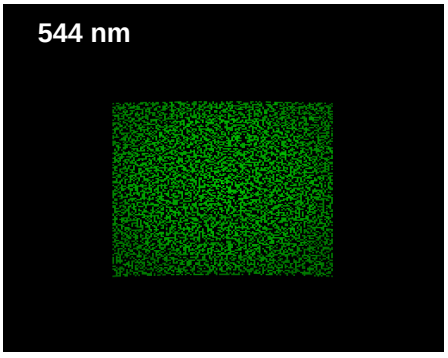

(d) calibration 544 nm

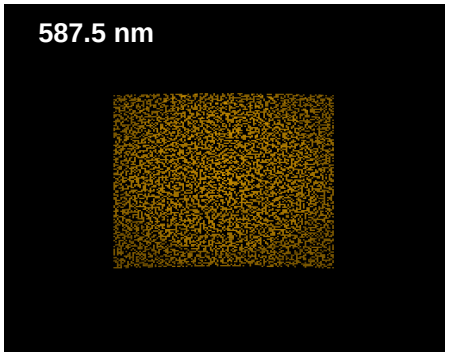

(e) calibration 587.5 nm

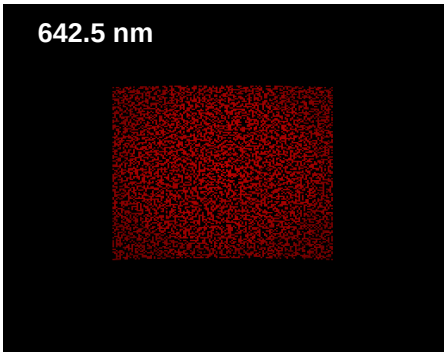

(f) calibration 642.5 nm

Figure 4.14: 6 monochromatic frames selected from 32 calibration channels demonstrate the calibration data.

4.3.3.2 Calibration Acquisition

Calibration data correspond to the measurement matrix **H** in Eq. (2.26) which has been discussed in the introduction. The measurement matrix authentically reflects the sys-

tem response to incoming signal, including aberration, magnification, dispersive displacement etc. In our case, the acquisition of the calibration data involve the location of each monochromatic frames at detector and by knowing that the reconstruction can be carried out. However, in practical experiments, due to the requirement of monochromatic light source, the calibration data could not be acquired by just one single shot. What was worse, it took long time to tune narrow bands across the spectra of interest in order to locate the calibrated wavelengths serving linear displacement. Taking advantage of ray trace software, the calibration can be achieved at one single shot by using one light source with all the bands of interest. The calibrated bands, which became prior knowledge when the system was designed, can be separately saved as text file for further processing.

Concretely speaking, the step to conduct the calibration procedure for SP-CASSI sim-

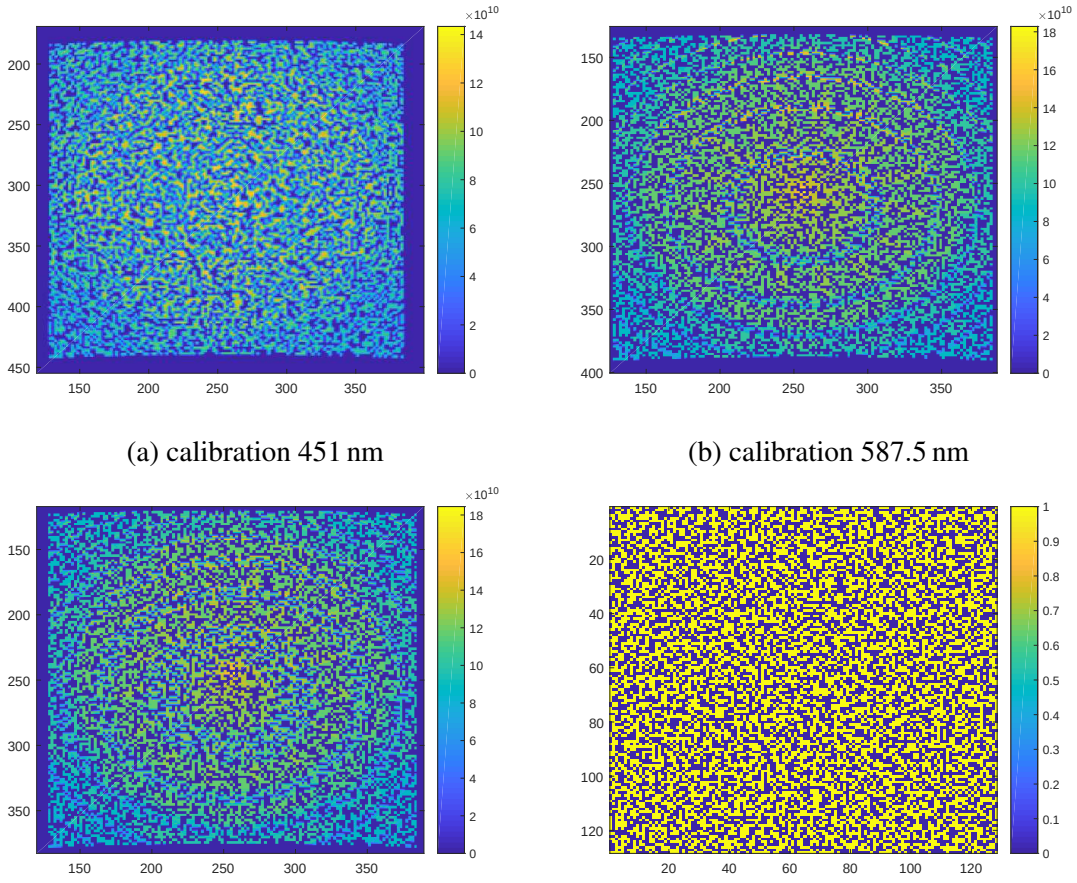

(a) calibration 451 nm

(b) calibration 587.5 nm

(c) calibration 642.5 nm

(d) Coded Aperture

Figure 4.15: 3 monochromatic calibration frames in comparison with the reference of coded aperture.

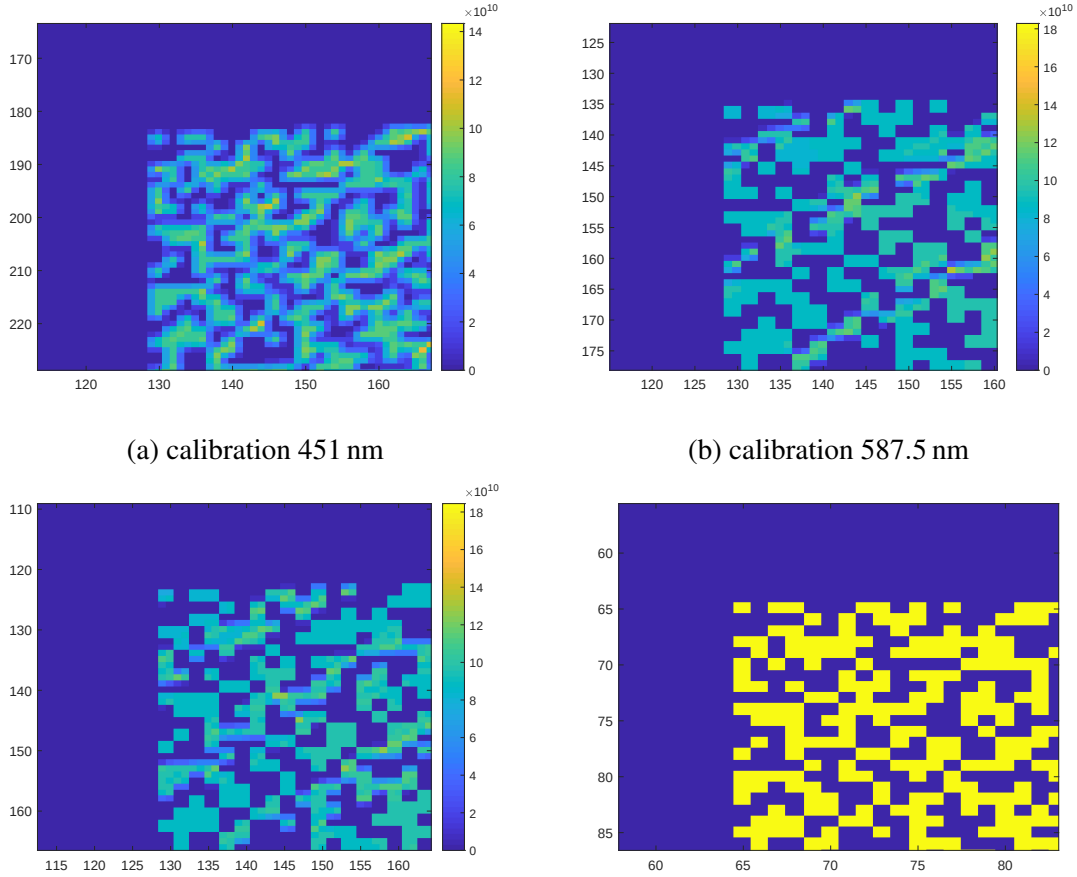

(a) calibration 451 nm

(b) calibration 587.5 nm

(c) calibration 642.5 nm

(d) Coded Aperture

Figure 4.16: Zoomed-in 3 monochromatic calibration frames in comparison with the reference of coded aperture.

ulation is to create 32-band uniform light source from 450 nm to 650 nm to illuminate the coded aperture at once, using the aforementioned method of building up 25 sampling point sources. Figure 4.14 shows 6 out of 32 monochromatic frames selected from uncropped $512 \times 512 \times 32$ calibration datacube, which are 451 nm and 475 nm from short wavelength zone, 514 nm, 544 nm and 587.5 nm from middle wavelength zone and 642.5 nm from long wavelength zone, presenting in the CIE 1964 colour scheme with 1 nm resolution. In the figure, it can be seen that the location of monochromatic frame moves upwards with the wavelength increasing, which complies the distribution of single pixel dispersion at the design stage. Particularly comparing three main frames 451 nm, 587.5 nm and 642.5 nm displayed in intensity by Matlab, it can be noticed that the effect of central bright spot surrounded by bright rings exists in each frame in Fig. 4.15, which is because the

system aberration caused non-uniform results. The pattern shape in calibration 451 nm was distorted more severely than in other two bands. The zoomed-in part in Fig. 4.16 shows calibration 451 nm was less focused than other two wavelengths, demonstrating the system aberration mainly exists in short wavelength.

4.3.3.3 Reconstruction Results

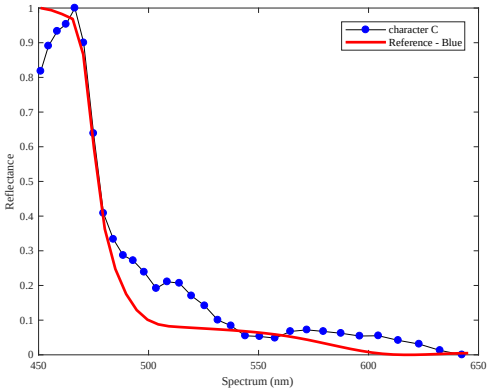

(a) Reconstructed spectral characteristics of "C"

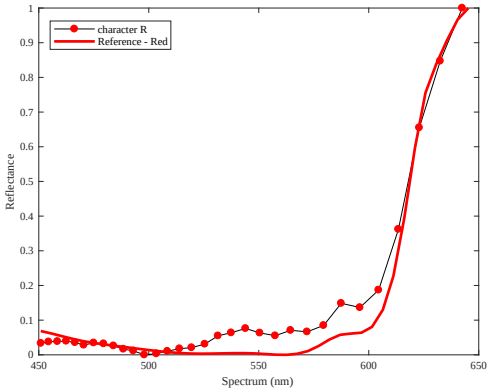

(b) Reconstructed spectral characteristics of "R"

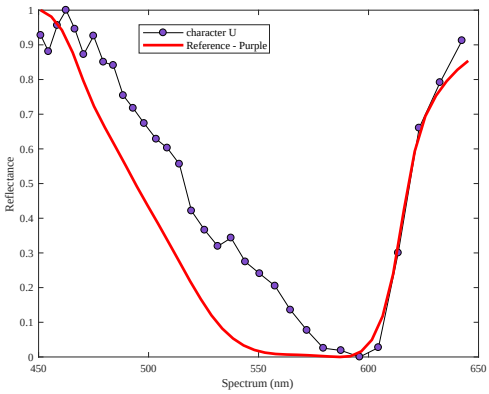

(c) Reconstructed spectral characteristics of "U"

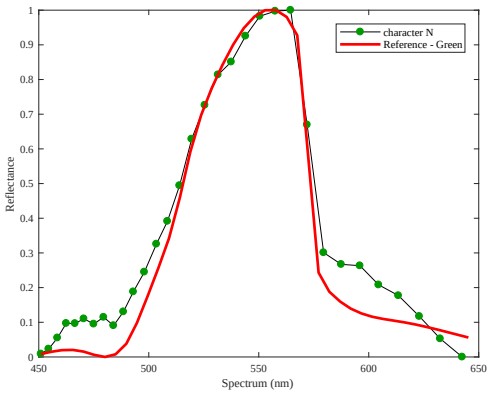

(d) Reconstructed spectral characteristics of "N"

Figure 4.17: Reconstruction results of spectral characteristics of four targets "C", "R", "U" and "N". The abscissa represents the spectrum in nm and the ordinate represents the unit-less normalised reflectance.

Spectral estimate is one of main results in the simulation. The estimate of spectral characteristics in Fig. 4.17 shows the meane value of 10×10 selected area on the reconstructed targets. The highlight area as an example in Fig. 4.18 was the region of interest with upper left corner at (225, 274) on the target "N" at frame 21, 550 nm. The reason

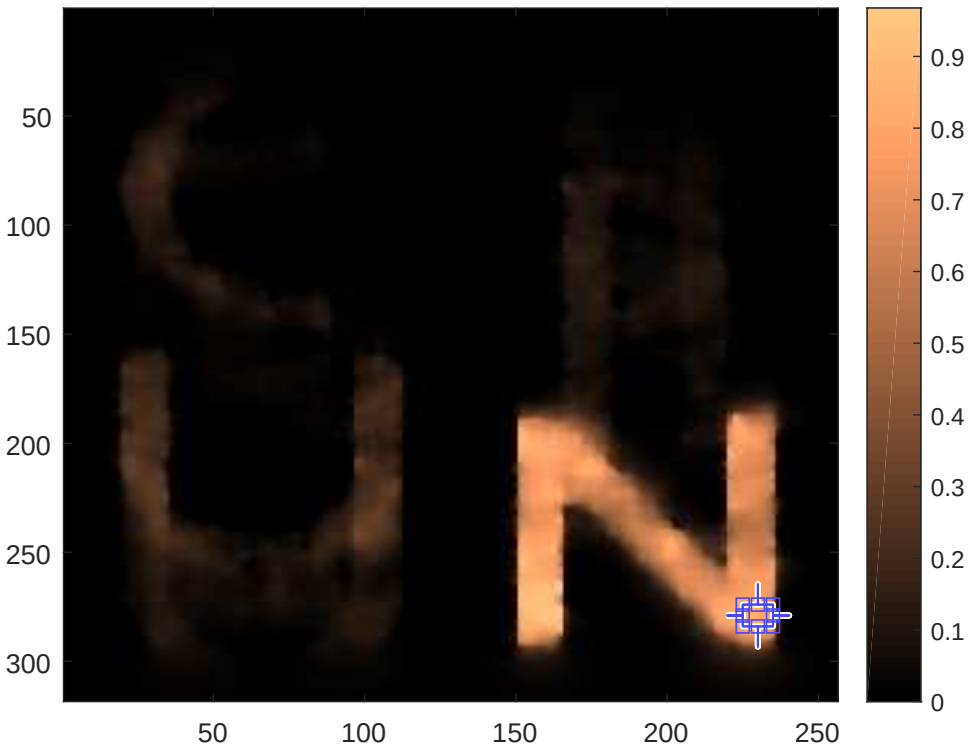

Figure 4.18: A 10×10 area was selected on the reconstructed target "N" in frame 21

why choose such ROI is that ROI can cover the main spatial area of target, not cross the size of reconstructed targets. For the same spectral characteristics curve is made up of 32 sampling ROI and later normalised along the wavelength as the normalisation method described,

$$X_{norm} = \frac{X_{local} - X_{min}}{X_{max} - X_{min}}, \tag{4.1}$$

where X denotes the mean value of the selected ROI at same location of targets across all the calibration wavelengths. X_{max} denotes the maximum value and X_{min} denotes the minimum value among 32 chosen area. For the figure, it can be read that overall trend of recovered curves for all the targets are mostly matched with the reference, while there exist 20.45% error in character "C",11.05% error in character "R", 25.19% error in character "U" and 10.54% error in character "N", where the error was the area difference between the reconstructed curve and the reference divided by the total area of the reference, cal-

culated by using built-in Matlab function *trapz* which calculates the integration area via the trapezoidal method. Please refer to the Matlab online help for further information. The large error that over 25% on "U" could be linked to the inaccurate calibration data corrupted by system aberration which results in the non-uniform error in monochromatic calibration frames. This misalignment due to system aberration can be solved by further optimising optics. Spatial reconstruction present in Fig. 4.19 with 1964 CIE colour

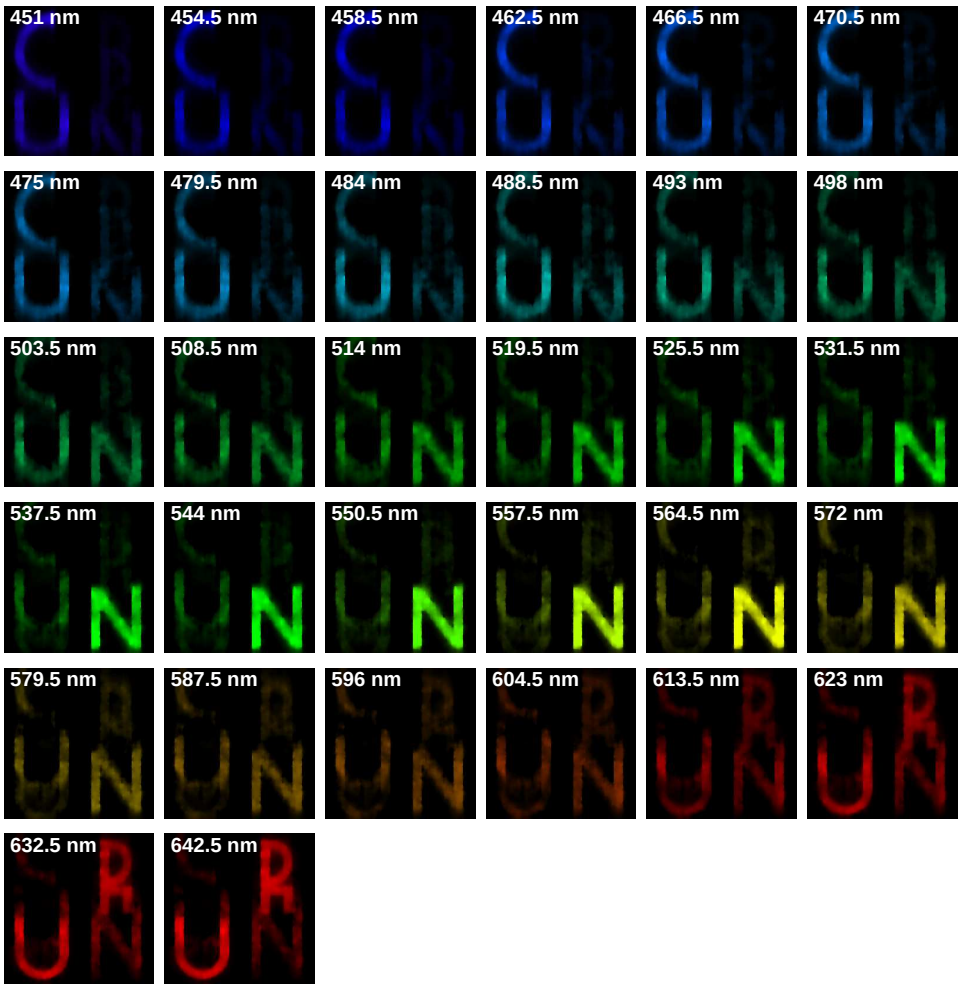

Figure 4.19: Reconstruction of SP-CASSI measurement shows 32 monochromatic calibration channels, displayed in 2D spatial dimension with 1964 CIE colour scheme applied for visualisation. Note that the colour scheme used here does not appear the targets' spectral characteristics but just for visualisation.

scheme serving visualisation purpose. The reconstruction is clear enough to identify the shape of the characters while it can be seen that the spatial reconstruction of "U" appears in most of calibrated frame, especially incorrectly enhanced at 503.5 nm to 531.5 nm, which matches the estimate of spectral characteristic.

4.4 Ultraviolet-Visible CASSI

4.4.1 Layout of UV-CASSI

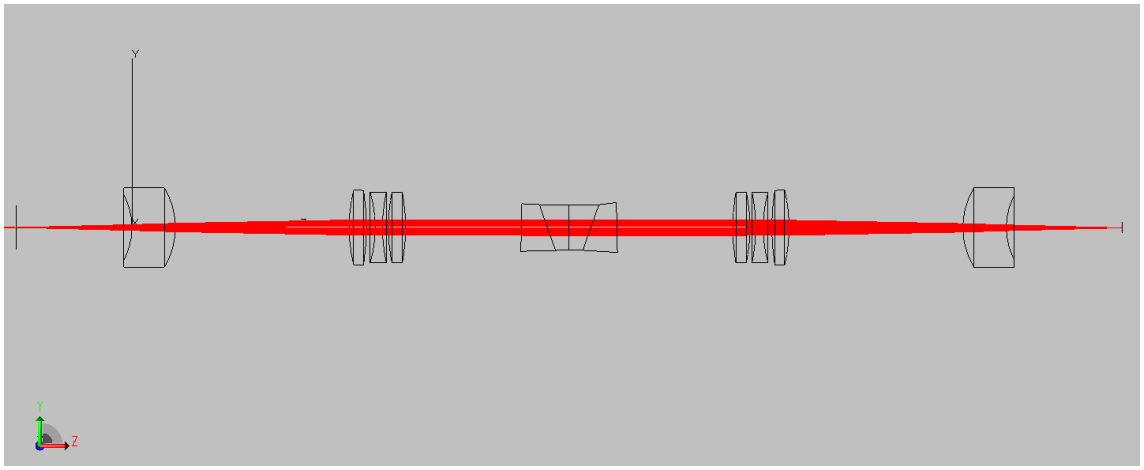

Figure 4.20: 3D system model of Ultra-Violet CASSI in TracePro under the ray propagation of 650 nm.

Following in specifications described in [98], the UV-CASSI was modelled in TracePro as shown in Fig. 4.20. The vertex of the first surface of the UV-CASSI is placed at origin of coordinate system, followed by the relay optics and a total track of 33 mm double amici prism. The detector is designed in a thin-sheet solid model, resulting in no thickness, placed at 342 mm to the origin. The entire system faces towards the negative Z direction, therefore, the coded aperture stays at -40 mm away from the vertex of the first surface of the UV-CASSI.

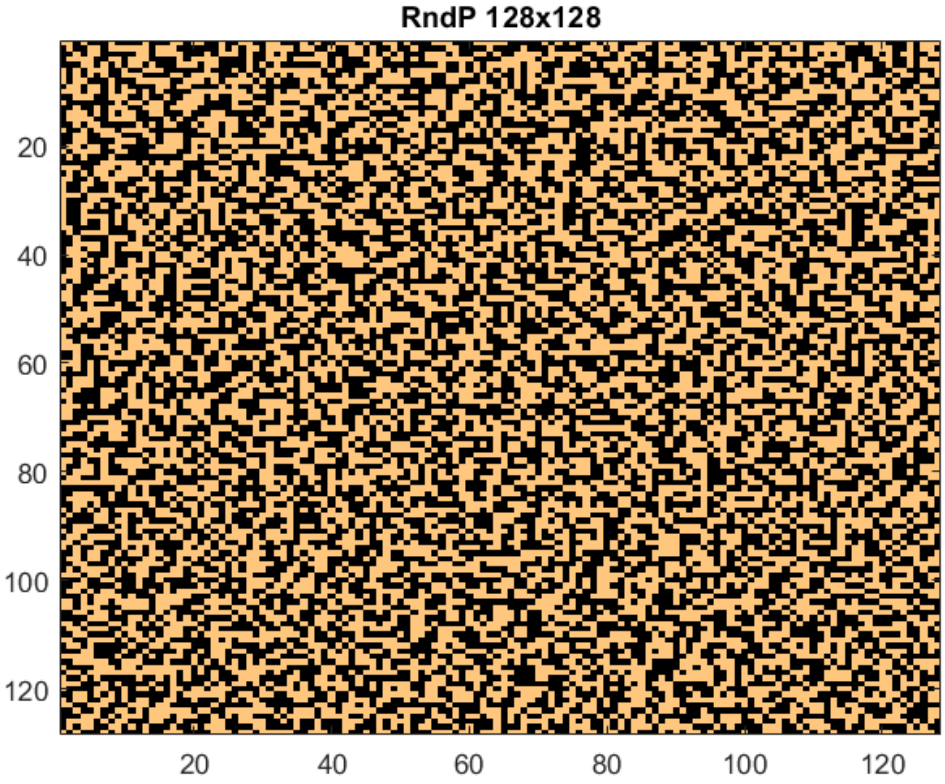

Figure 4.21: 128×128 random pattern for UV-CASSI.

4.4.2 Ray Tracing Strategy

Ray tracing strategy was the same as described in the simulation of SP-CASSI while there is a slight modification to match the F-number of the relay optics, the target sources were set to accommodate the objective lens which has a focal length of 50 mm with image numerical aperture 0.0625. The file source for emitting an uniform illumination onto coded aperture was reduced to 14 bands due to the resolution raised to 14.8 mm on detector, the illuminating area thus increasing to $1.8944\,\text{mm} \times 1.8944\,\text{mm}$ of a $128\,\text{p} \times 128$ pattern as shown in Fig. 4.21. The increase of smallest feature of coded aperture to $2\times$ detector pixel is due to the experimental conclusion that the adjacent pixels could be highly corrupted by unexpected factors, e.g. system aberration caused by manufacturing errors. In such case, our simulation adopts double detector pixel to be 14.8 mm.

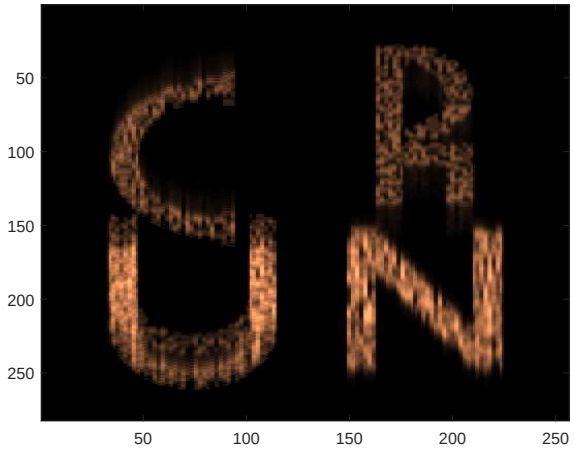

Figure 4.22: Detector measurement collected from TracePro were cropped to an image of 256×282 pixels displayed in Matlab. The raw measurement were pixelated by a 512×512 detector with 7.4 µm pitch.

4.4.3 UV-CASSI Simulation Result

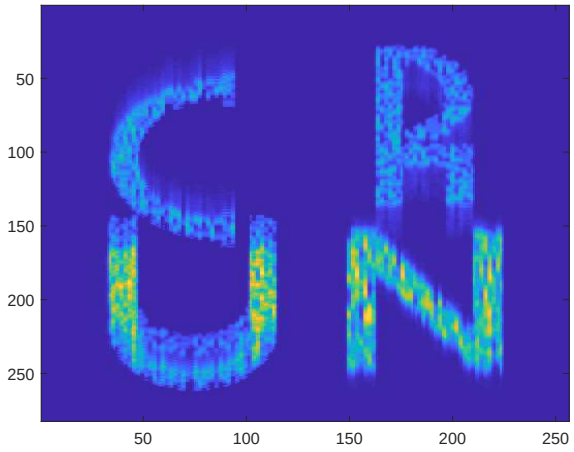

Figure 4.23: Detector measurement shown in intensity. The light area represents high intensity and the the dark (blue) area represents low intensity.

As we can see from Fig. 4.22, the measurement taken from a 512×512 detector in simulation was cropped to an image of 256×282 pixels. 14 band dispersion displacement results in a total of $2 \times (14-1)\ CA\ pixels = 26\ detector\ pixles$. It should be noticed that the actual dispersion direction from short wavelength to long wavelength is from the top to the bottom, just like the shifting direction of CA pattern in Fig. 4.24a, Fig. 4.24b

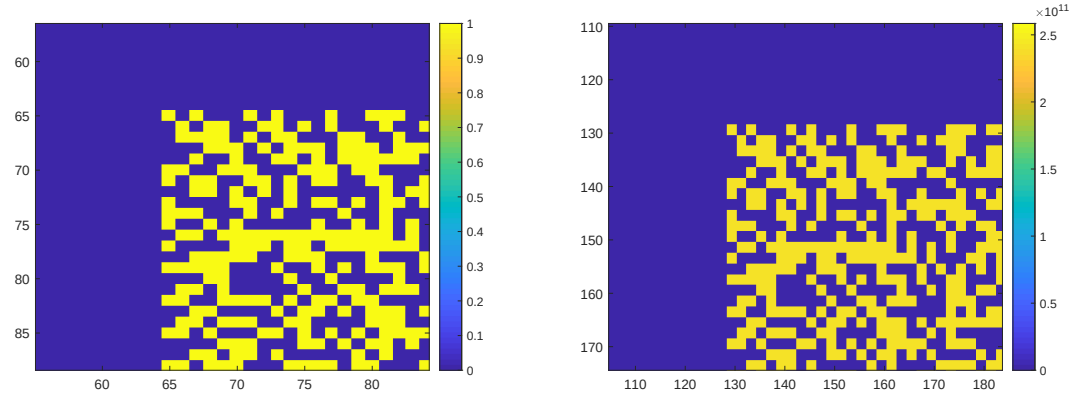

(a) calibration 456.7 nm

(b) calibration 499.7 nm

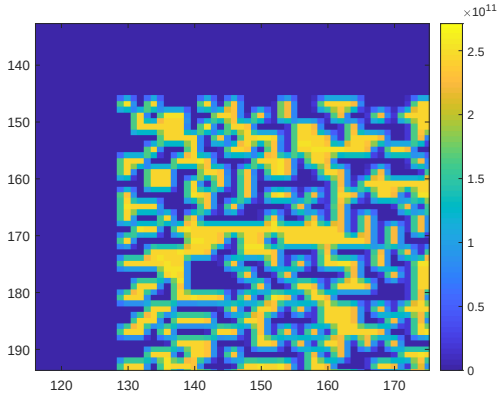

(c) calibration 650.4 nm

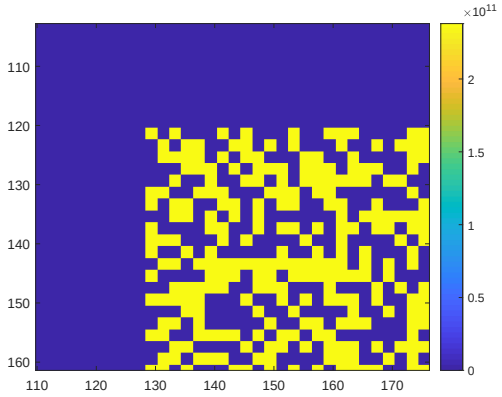

(d) Coded Aperture

Figure 4.24: Partial 3 monochromatic calibration frames in comparison with the reference of coded aperture. The calibration 456.7 nm and 499.7 nm have a clear pattern while calibration 650.4 nm is blur.

and Fig. 4.24c, while both Fig. 4.22 and Fig. 4.23 are turned upside down to demonstrate the image more naturally, which results in a position relationship between character "C" and "R" differed from Fig. 4.12, despite the fact that they are the same targets in both simulations. Besides, it can be noticed that character "R" and "N" did not overlap with each other after multiple bands shifted. In Fig. 4.24, the monochromatic calibration frames present uniform intensity within the frame, average intensity of individual frames changing as a function of wavelength. It is quite clear to notice no obvious aberration exists among three main frames compared to the ideal coded aperture pattern, which could be due to a small numerical aperture that make the system close to a paraxial approximated condition to the illuminating rays and then much ease the system aberration.

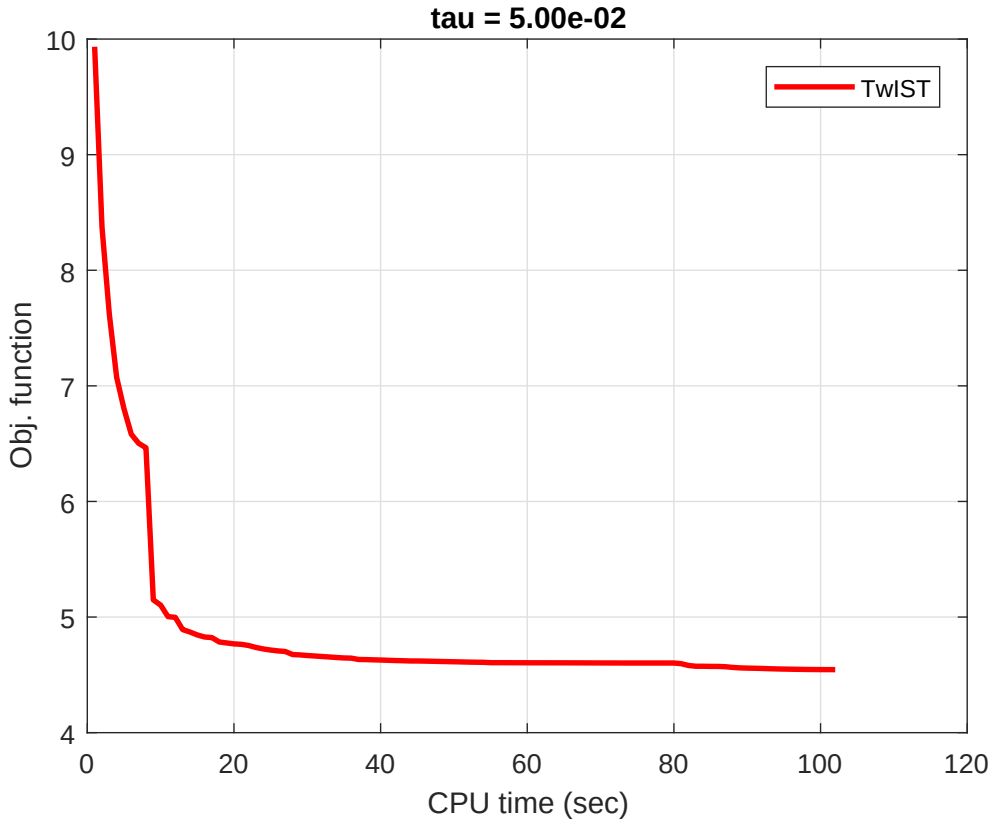

Figure 4.25: Convergent rate of the TwIST algorithm running UV-CASSI results.

As the calibration data was quite close to the ideal pattern and nearly free of aberration, the reconstruction results of spectral estimate in Fig. 4.26. The error between the reconstructed curves and the reference one has 20.88% in character "C", 1.32% in character "R", 7.58% in character "U" and 8.72% error in character "N". Spatial reconstruction in Fig. 4.27 can be expected to be satisfactory under TwIST tuning parameter $\tau = 0.05$ and 100 iterations. With the number of calibrated wavelengths reduced from 32 bands to 15 bands, the estimate quality of individual targets in a single frame have been improved compared to Fig. 4.27 and SP-CASSI results in Fig. 4.19.

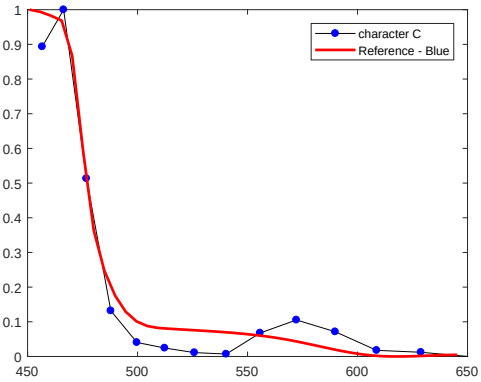

(a) Reconstructed spectral characteristics of “C”

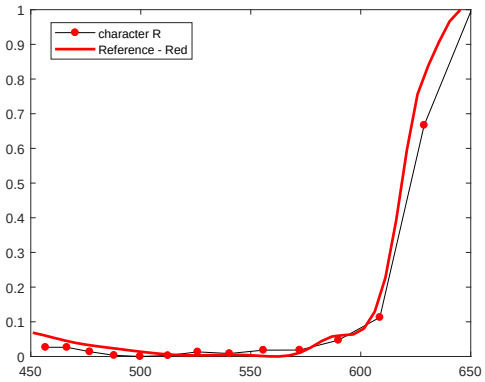

(b) Reconstructed spectral characteristics of “R”

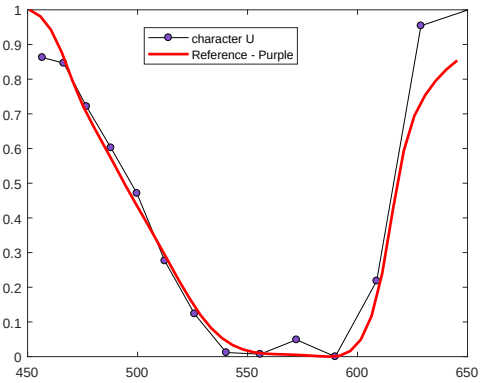

(c) Reconstructed spectral characteristics of “U”

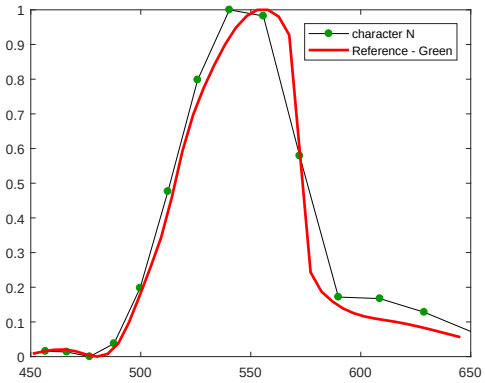

(d) Reconstructed spectral characteristics of “N”

Figure 4.26: Reconstruction results of spectral characteristics of four targets “C”, “R”, “U” and “N”. The abscissa represents the spectrum in nm and the ordinate represents the unit-less normalised reflectance.

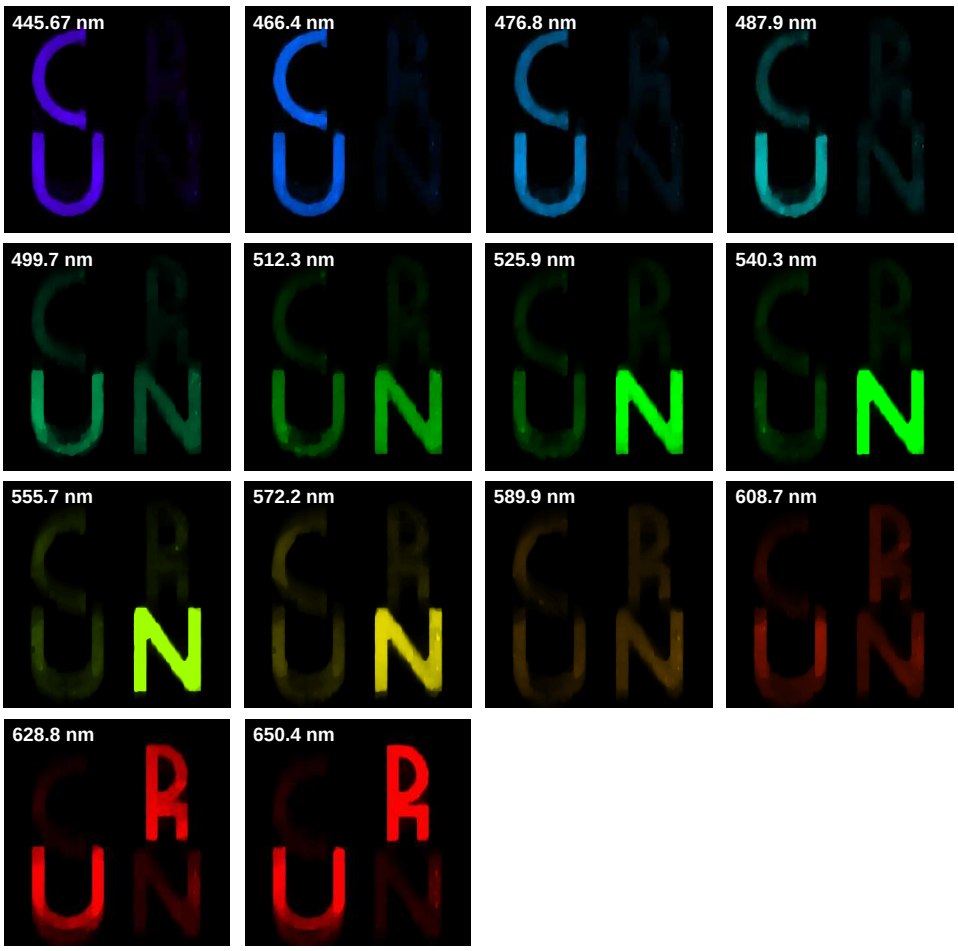

Figure 4.27: Reconstruction of UV-CASSI measurement shows 14 monochromatic calibration channels, displayed in 2D spatial dimension with 1964 CIE colour scheme applied for visualisation.

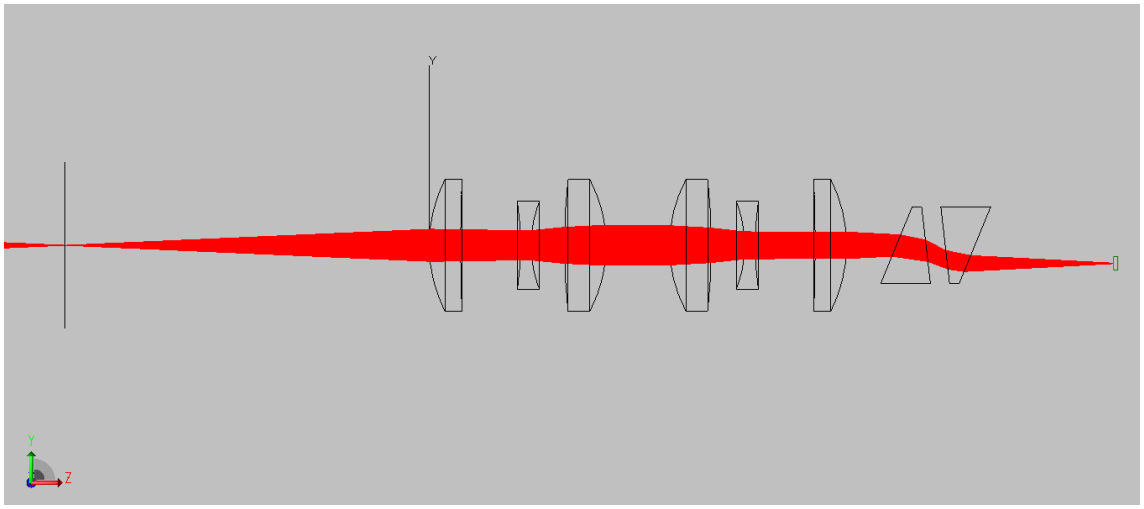

Figure 4.28: Ray propagation in the DP-CASSI at air gap of 4.64 mm.

4.5 Dual-Prism CASSI

As a wavelength-tuneable dispersive system, 5 simulations by varying the distance of air gap from 3.44 mm to 5.04 mm have been conducted to demonstrate the capability of tuning calibrated wavelengths without replacing any optics.

4.5.1 Layout of DP-CASSI

The structure of DP-CASSI was optimised at air gap of 4.64 mm and final version is displayed in a ray propagation diagram in Fig. 4.28. Due to unique feature that optical axis after the prism would generate a spatial offset in sagittal plane, the detector had to be moved to a new location where the central wavelength 550 nm could always stay focused at the central point on the detector. The resulting location of detector at current air gap is -4.485 mm, which indicates the shift of detector is below the original optical axis. By doing that for another 4 sets of air gap, the resulting locations are -3.874 mm at 3.44 mm, -4.047 mm at 3.84 mm, -4.221 mm at 4.24 mm and -4.485 mm at 5.04 mm. The above relocation of the detector was pre-calculated by building a custom function in OSLO using its feature macro language, *Compile Command Language*, which save the inconvenience to adjust this change. As the overview of the DP-CASSI shown above, the vertex of the first surface of relay lens was placed at the origin of the coordinate system,

facing towards negative Z direction. Coded aperture mask was placed at -87.7 mm away from the origin. A total track of 18.97 mm dual-prism was placed after the relay lens about 12 mm and last surface to image plane is 33.6 mm.

4.5.2 Ray Tracing Strategy

Different from previous ray tracing strategy in SP-CASSI or UV-CASSI, the DP-CASSI after optimisation has been adjusted to an object numerical aperture of 0.05 and magnification of -0.8, in order to balance aberration. Since this numerical aperture is quite small, ray tracing strategy was simplified as in praxial condition using collimating rays by the built-in grid source, instead of constructing a series of file sources at high expense of processing time. The incoming target rays to the coded aperture were directly illuminated by the uniform grid source set with 256×256 sampling rays, doubly sampling the target as the coded aperture used in this case is 128×128. The number of wavelengths was adjusted in accordance with the requirement. The acquisition of calibration data was according to this strategy while collimating rays directly illuminated the coded aperture under uniform irradiance.

4.5.3 DP-CASSI Simulation Results

Like all other CASSI, the DP-CASSI also requires a spectral calibration to identify the spectral characteristic of the system. Meanwhile unlike all other CASSI, calibrated wavelengths need to be recalibrated and collected again whenever the air gap of the DP-CASSI changes due to its main feature of wavelength shifting. The corresponding location of the detector is adjusted as well to align the location of central wavelength to the central point of the detector. This step was calculated in OSLO to automatically align the detector and directly translate into TracePro.

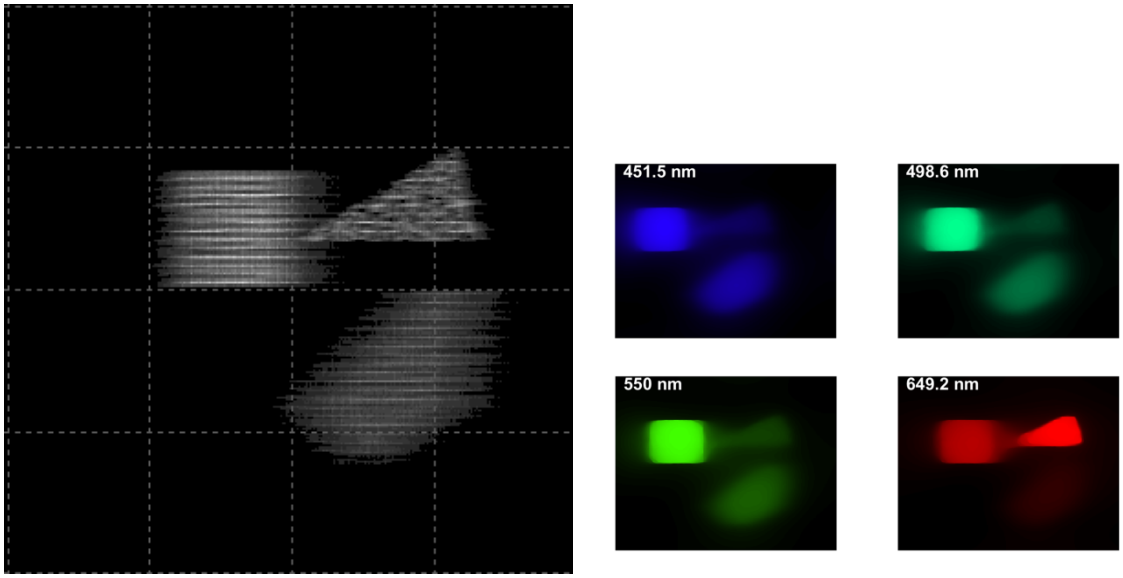

(a) Spatial-spectral multiplexed raw grey scale image of 3 targets

(b) Colour images of 4 reconstructed frames

Figure 4.29: Results of the DP-CASSI at air gap of 4.24 mm with a spatial-spectral multiplexed raw image in grey scale and 4 reconstructed frames reconstructed by TwIST with the regularizer tuning parameter $\tau = 0.5$.

4.5.3.1 Initial DP-CASSI Simulation

At our first simulation of the DP-CASSI, a wide spectral range of about 50 bands across 400 nm to 700 nm was required as calibration wavelengths in order to achieve a better dispersive displacement compared to the previous CASSIs. By applying this idea, a smallest feature of 6.5 µm was considered as minimum distance between adjacent calibration wavelengths. Simulation of the DP-CASSI under this consideration was conduced with three same objects in Fig. 4.2b by applying three different air gaps of the dual prism at 4.24 mm, 4.64 mm and 5.04 mm accordingly. One of the multiplexed results in Fig. 4.29a together with the TwIST algorithm applied for reconstruction in Fig. 4.29b, were obtained using regularizer tuning parameter $\tau = 0.5$. The quality of the images shown in Fig. 4.29b is seen to be fair and it exibits certiain degree of blurring while smoothly, which could be tuned by changing the regualrizer tuning parameter.

The regularization tuning parameter τ in Eq. (2.26) balances the optimisation between the spatial resolution and the spectral accuracy of the multiplex image decompression. It

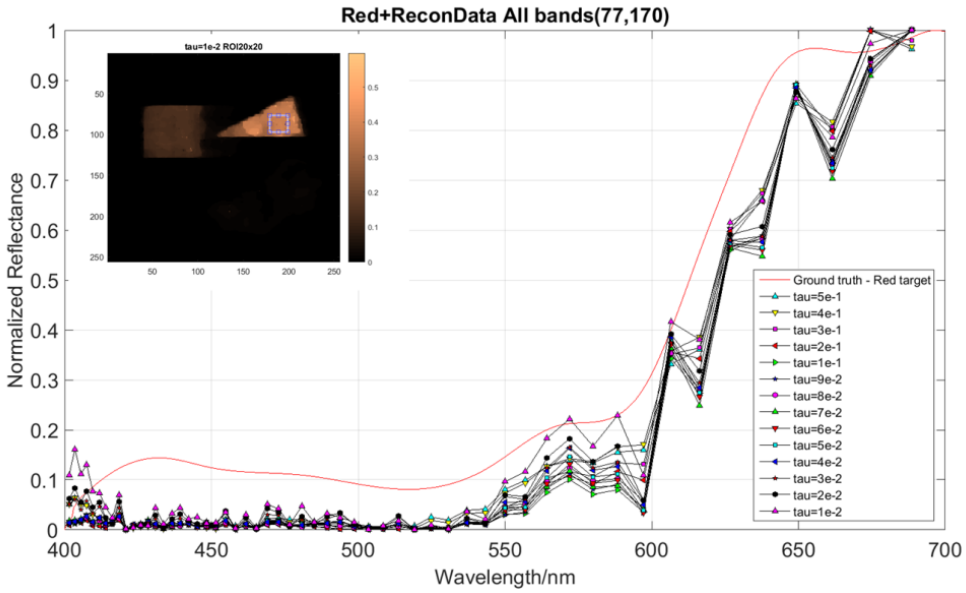

Figure 4.30: The effect of the reconstructions for the red triangle target by using a range of regularizer tuning parameters τ from 0.01 to 0.5 was shown. It is seen that the smaller the τ (e.g. 0.02 and 0.01) the better is the spectral reconstruction accuracy.

is seen that the larger value of τ (e.g. $\tau = 0.5$) gives more spectral errors in Fig. 4.30 while at the same time it exhibit higher degree of spatial smoothness in Fig. 4.31. The correct regularization parameter could be optmised in principle under certain constraints; however, this could be developed in the future due to the work in the thesis mainly focusing on optical design and the reconstructed results of the red target, Triangle, in Fig. 4.30 were not matched with the ground truth very well by varying the parameter τ from 0.01 to 0.5, wherein the best choice of τ is 0.01 among current options.

By fixing the parameter τ to 0.01, Figure 4.32 plots a few normalised reflectance of an averaged 20×20 pixels for three air gap simulations in three different colour objects. The error bars shown in the figure are the standard deviation over the 400 pixels in the selected ROI. Note that from the recovered spectra it can be found the spectral reconstructions have a very large deviation to the reference curves with 31.84% error in Red, 25.05% in Blue and 10.39% in Green. This is believed partly due to the optical aberration and partly to the large calibration wavelengths to affect the accuracy of spectral reconstruction. Therefore, in the next simulation, this will be improved by reducing the spectral range from 400 nm

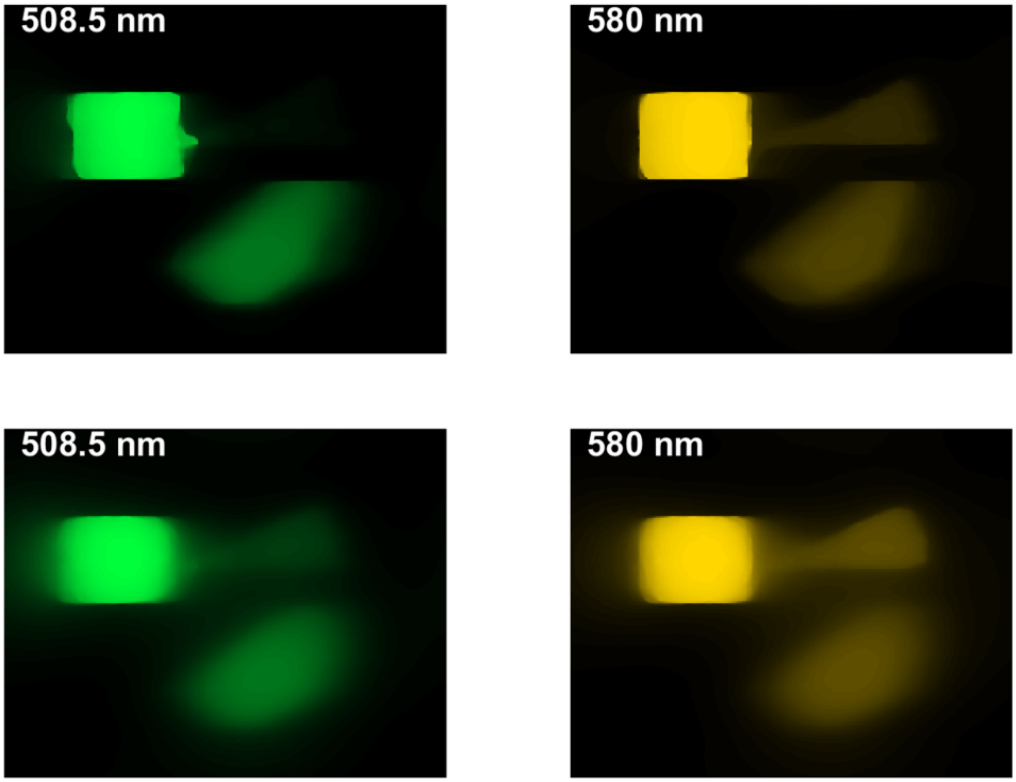

Figure 4.31: Highlight the effects of the tuning parameter τ in the TwIST algorithm for two wavelengths at 508.5 nm and 580 nm: upper panel $\tau = 0.1$ and lower panel $\tau = 0.5$. It is seen that the reconstructed image blur is stronger for larger τ.

to 700 nm to 450 nm to 650 nm and raising the current smallest feature 6.5 µm, which results in a significantly drop in the number of wavelength from 50 bands to 15 bands. The details of the investigation in the number of calibration wavelengths associated with image recovery quality will be included in a to-be-submitted paper.

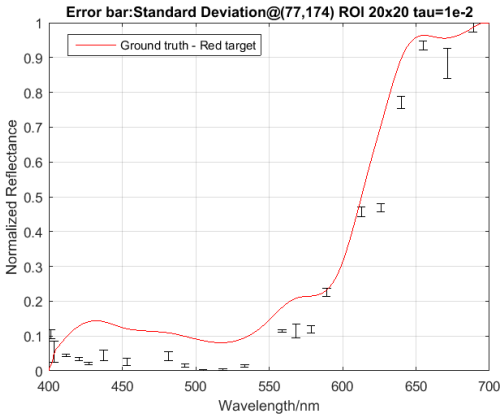

(a) Estimate of spectral characteristic of Red Triangle

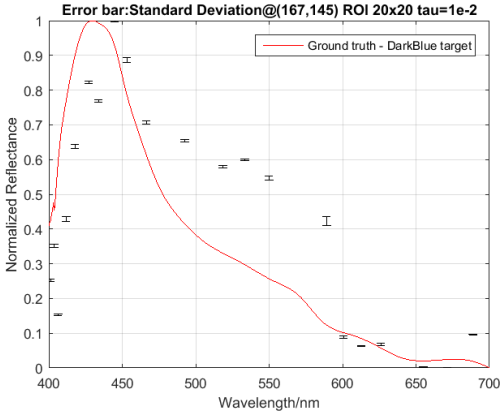

(b) Estimate of spectral characteristic of Blue Pentagon

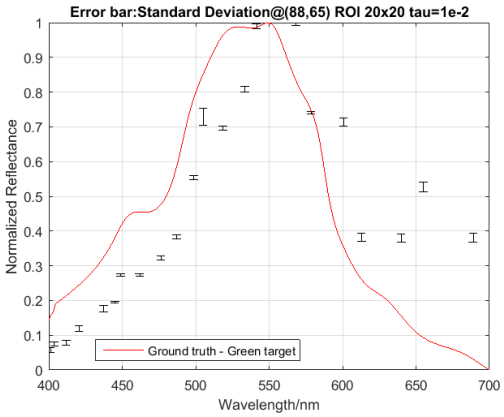

(c) Estimate of spectral characteristic of Green Square

Figure 4.32: The estimate of spectral characteristics for 3 targets using combined results of 3 different air gaps are shown. In all cases the reconstruction data is represented by the mean of 20×20 pixel ROI with standard deviation as error bars and to compare with that of the ground truth shown in solid line.

4.5.3.2 Second DP-CASSI Simulation

Following the results of the initial DP-CASSI simulation, the calibration wavelengths using in this case were sampled with smallest feature 13 nm doubly increased and narrowed down with 449.7 nm to 651.8 nm as demonstrated in Table 3.3. The air gap was expanded from initial 3 air gaps to 5 sets: 3.44 mm, 3.84 mm, 4.24 mm, 4.64 mm and 5.04 mm, with respect to 13, 14, 15, 16 and 16 bands. Based on the confirmation of system aligned to central wavelength, the main feature that wavelength tuning as the air gap changes can be tracked in Fig. 4.34, showing the prior channel to the central wavelength was indeed shifted from 533.4 nm to 536.9 nm with the proof that intensity and geometry shape changed within two marked areas of [28:32, 21:26] and [26:31, 47:52] due to system response to different wavelengths.

Calibration data was captured as the example frame 550 nm at air gap of 3.44 mm in Fig. 4.33a. The calibration frame of the central wavelength 550 nm is critical to be aligned at the centre of image plane for locating all the calibration wavelengths. To confirm the alignment of the central wavelength frame, Fig .4.33f demonstrates a zoomed-in area of 67×42 from all the central wavelength frames at all 5 air gaps. It is seen that the sampling point [21 38] remain the same spot across 5 frames. The pattern images generally remain the same at Gap1, Gap2 and Gap3 while the pixel intensity at Gap1 is dropped by a factor of 2 compared to Gap2 and Gap3 due to the aberration error. Slight expanding of pixels at upper panel can be found at Gap4 and Gap5. It is believed that systems under such 5 air gaps have been fully aligned.

As the key feature, the wavelength shift was confirmed in Fig. 4.34, showing the condition of two selected areas [28:32, 21:26] and [26:31, 47:52] on the channel of -1 pixel shift to the central channel at all 5 air gaps. The patterns in both marked areas in the figure stay same while the wavelengths present differently, which indicates the wavelength shifting.

Main reconstruction results of those 5 setups have been demonstrated as follows,

- Gap1 - 3.44 mm: Fig. 4.35 shows the reconstruction of 13 channels in spatial

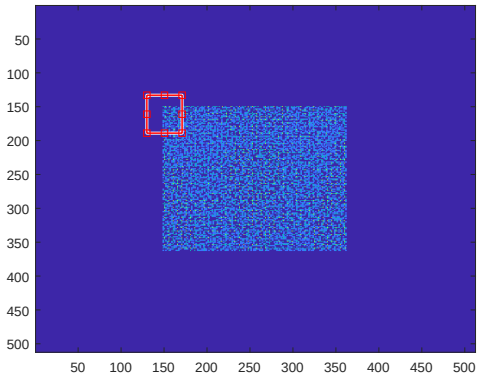

(a) An area of 67×42 in 550 nm calibration frame at air gap of 3.44 mm was selected to zoomed-in for further comparison

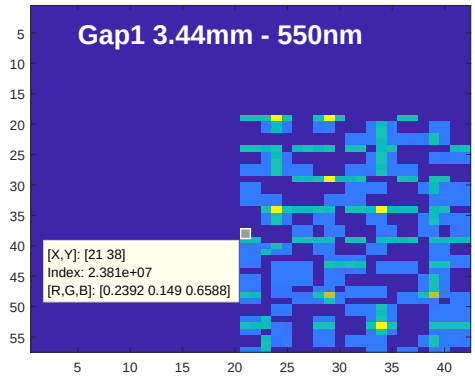

(b) Zoomed-in region at air gap of 3.44 mm

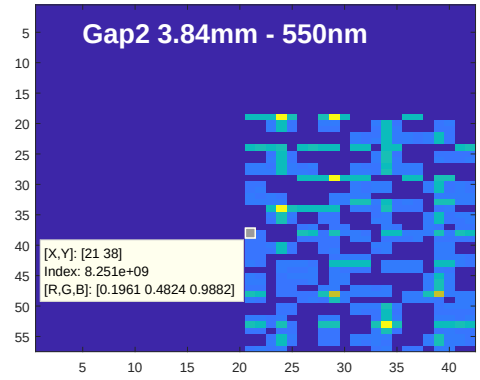

(c) Zoomed-in region at air gap of 3.84 mm

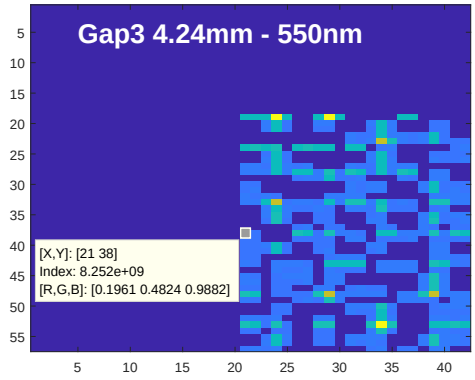

(d) Zoomed-in region at air gap of 4.24 mm

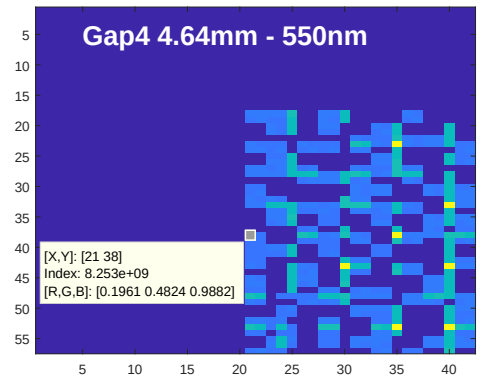

(e) Zoomed-in region at air gap of 4.64 mm

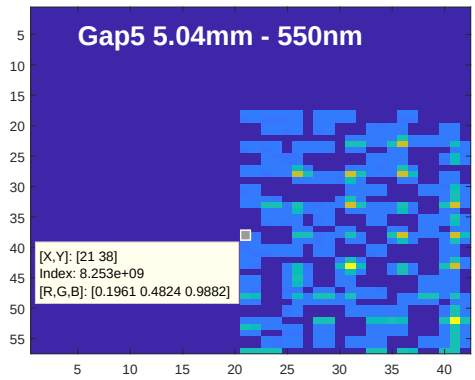

(f) Zoomed-in region at air gap of 5.04 mm

Figure 4.33: Zoom in the same area at each air gap, as marked in red rectangular region of 67×42 pixels at 550 nm calibration frame to compare the central frame under different air gaps. A point [21 38] as a reference mark was point out in all the frames to align the location of the pattern at each air gap, wherein the intensity at that point at Gap2 to Gap5 have same value while the intensity at Gap1 dropped from 8.52×10^9 to 2.38×10^7.

domain. Fig. 4.40 shows the spectral estimate of three objects.

- Gap2 - 3.84 mm: Fig. 4.36 shows the reconstruction of 14 channels in spatial

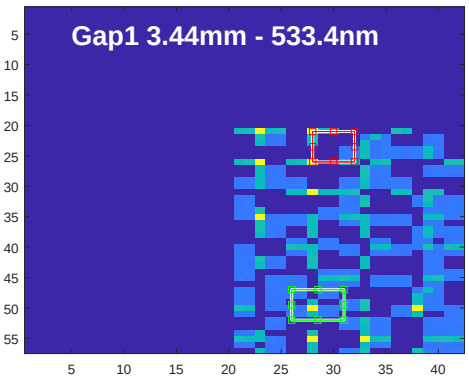

(a) Tracking areas at 533.4 nm

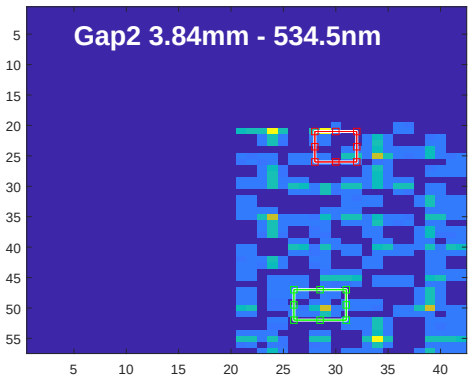

(b) Tracking areas at at 534.5 nm

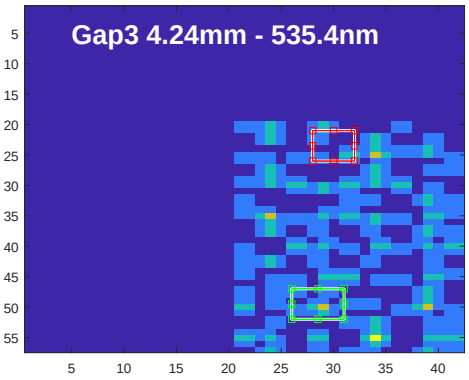

(c) Tracking areas at at 535.4 nm

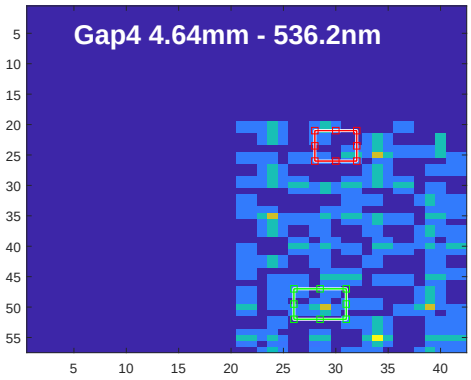

(d) Tracking areas at 536.2 nm

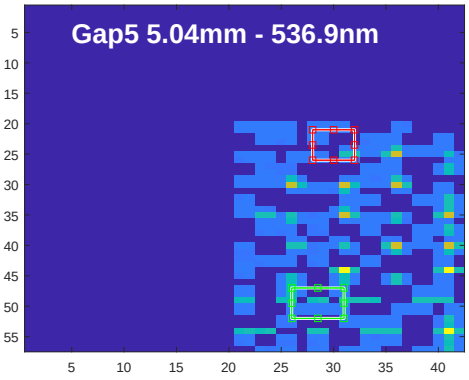

(e) Tracking areas at 536.9 nm

Figure 4.34: Two areas:[28:32, 21:26] and [26:31, 47:52] are marked in one channel prior to the channel where central wavelength is at five air gaps. By moving one channel with step 13 µm forwards at detector, the spectral shifts from 533.4 nm to 536.9 nm.

domain. Fig. 4.41 shows the spectral estimate of three objects.

- Gap3 - 4.24 mm: Fig. 4.37 shows the reconstruction of 15 channels in spatial domain. Fig. 4.42 shows the spectral estimate of three objects.

- Gap4 - 4.64 mm: Fig. 4.38 shows the reconstruction of 16 channels in spatial domain. Fig. 4.43 shows the spectral estimate of three objects.

- Gap5 - 5.04 mm: Fig. 4.39 shows the reconstruction of 16 channels in spatial domain. Fig. 4.44 shows the spectral estimate of three objects.

From the figures, it can be seen that those spatial reconstructions are sharp and clear enough to identify the types of targets and especially be able to tell the edge with a high accuracy, compared to the existence of image blurring in Fig. 4.29b. Likewise, the estimates of spectral characteristics at all 5 air gaps are highly matched with the ground truth. The simulation of the DP-CASSI by reduction of number of calibration wavelengths achieved the reconstruction results with higher quality in terms of both spatial and spectral domain.

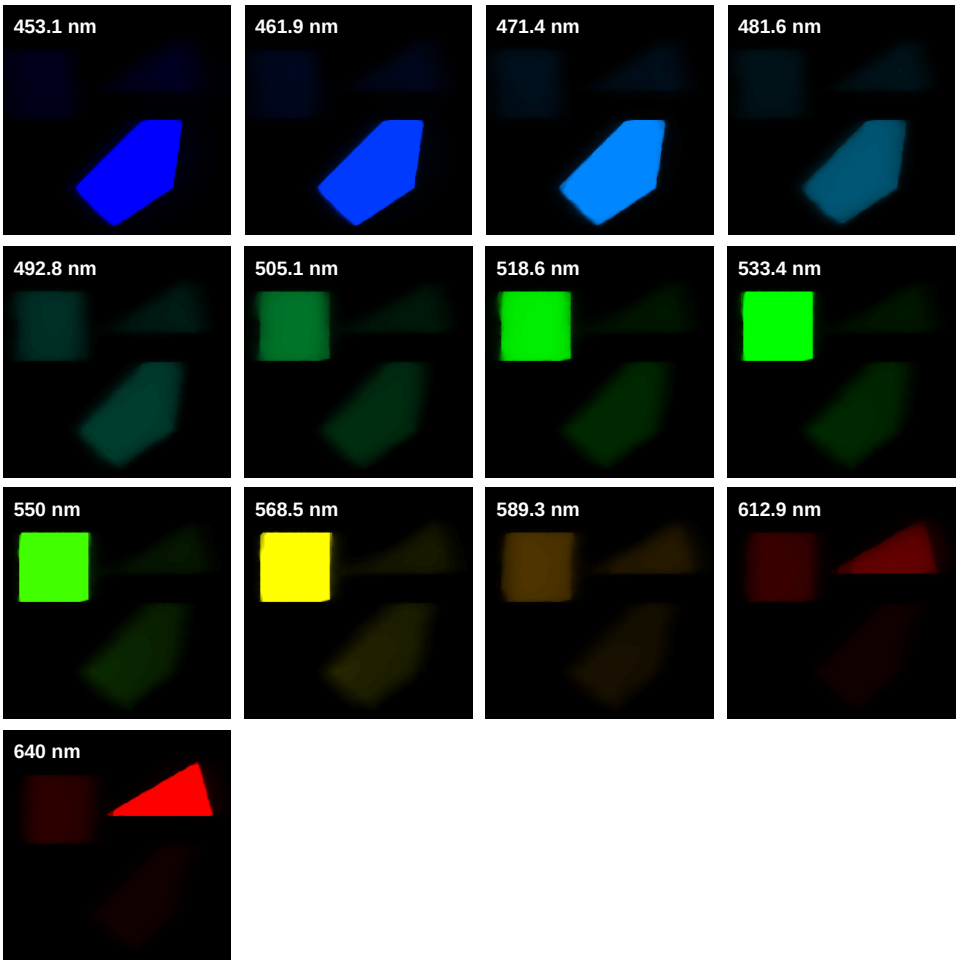

(a) Reconstruction of 13 channels by TwIST algorithm with tuning parameter $\tau = 0.05$

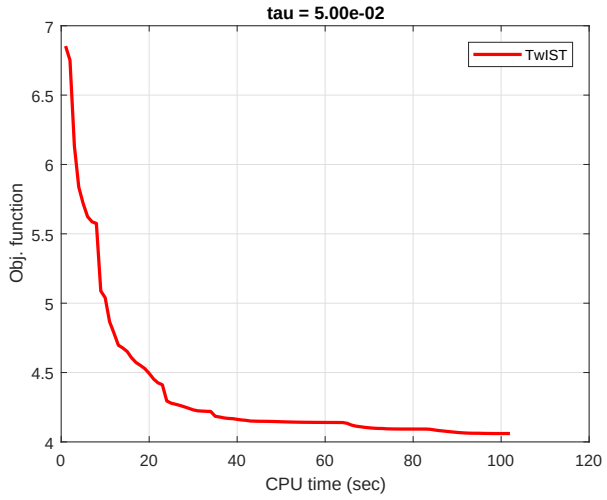

(b) Convergent rate curve of TwIST algorithm running estimate for the data of air gap of 3.44 mm

Figure 4.35: Reconstruction data for the measurement captured by the DP-CASSI with air gap of 3.44 mm.

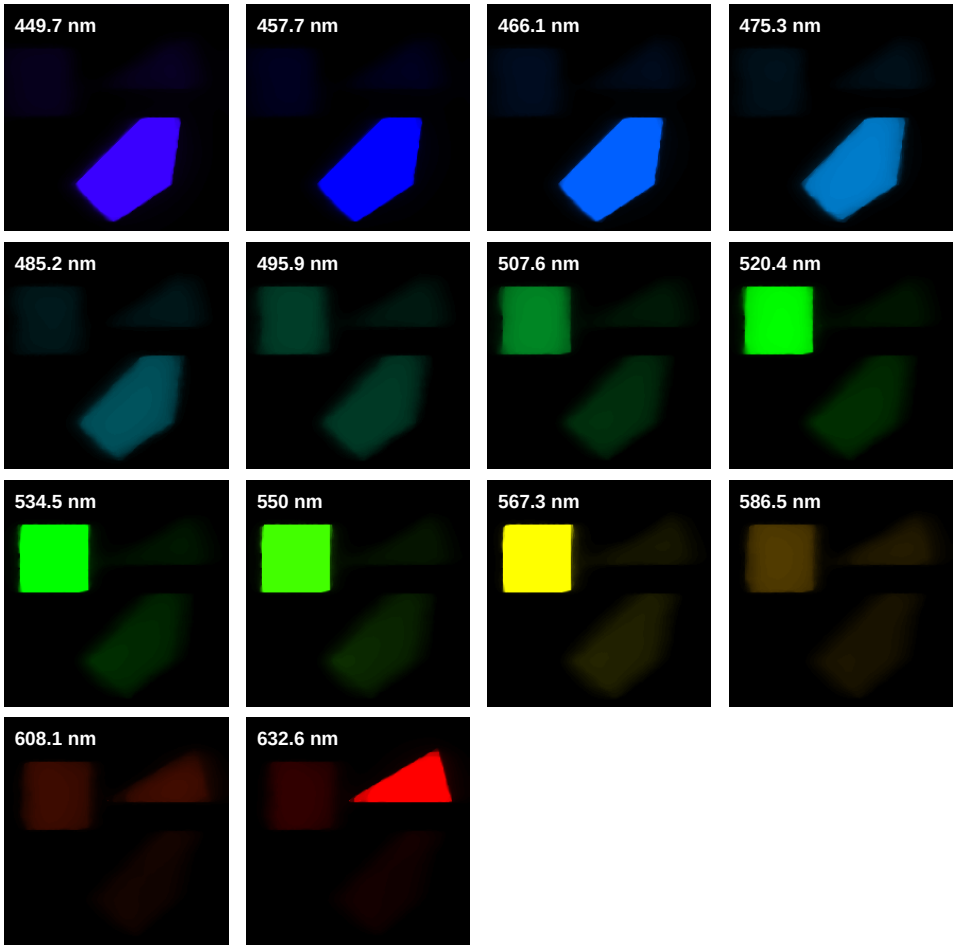

(a) Reconstruction of 14 channels by TwIST algorithm with tuning parameter $\tau = 0.05$

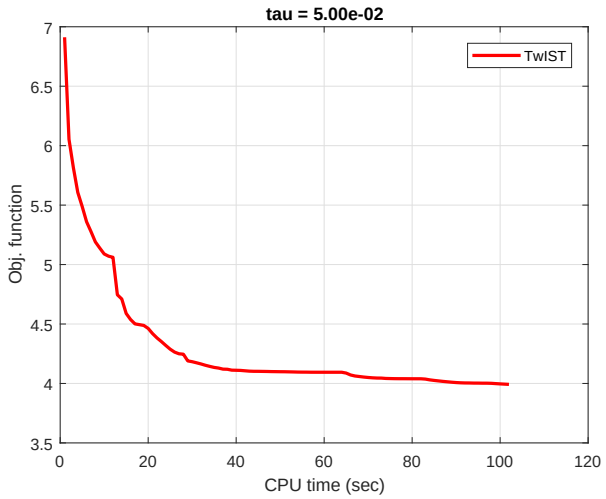

(b) Convergent rate curve of TwIST algorithm running estimate for the data of air gap of 3.84 mm

Figure 4.36: Reconstruction data for the measurement captured by the DP-CASSI with air gap of 3.84 mm.

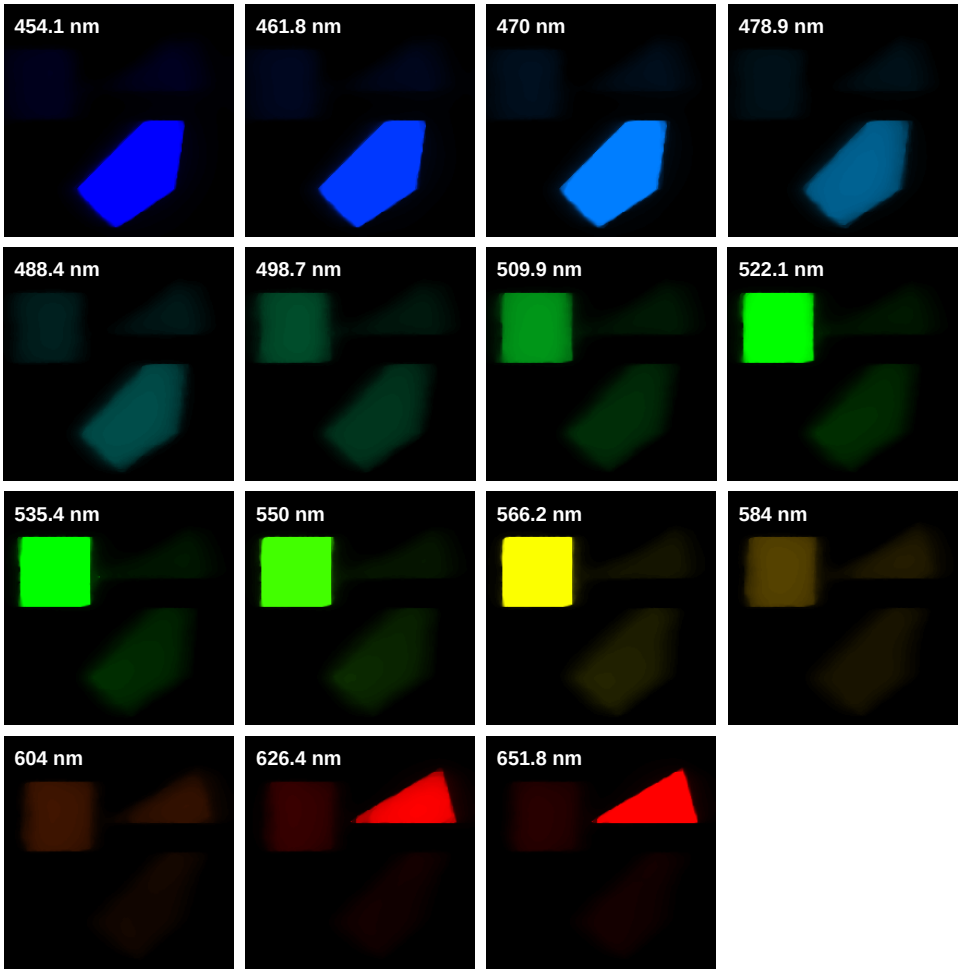

(a) Reconstruction of 15 channels by TwIST algorithm with tuning parameter $\tau = 0.05$

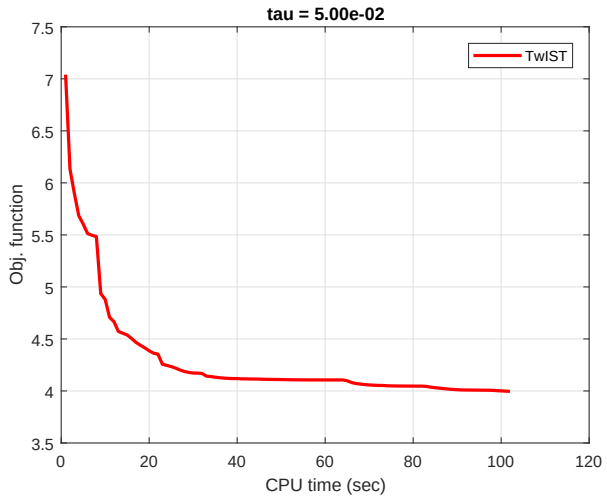

(b) Convergent rate curve of TwIST algorithm running estimate for the data of air gap of 4.24 mm

Figure 4.37: Reconstruction data for the measurement captured by the DP-CASSI with air gap of 4.24 mm.

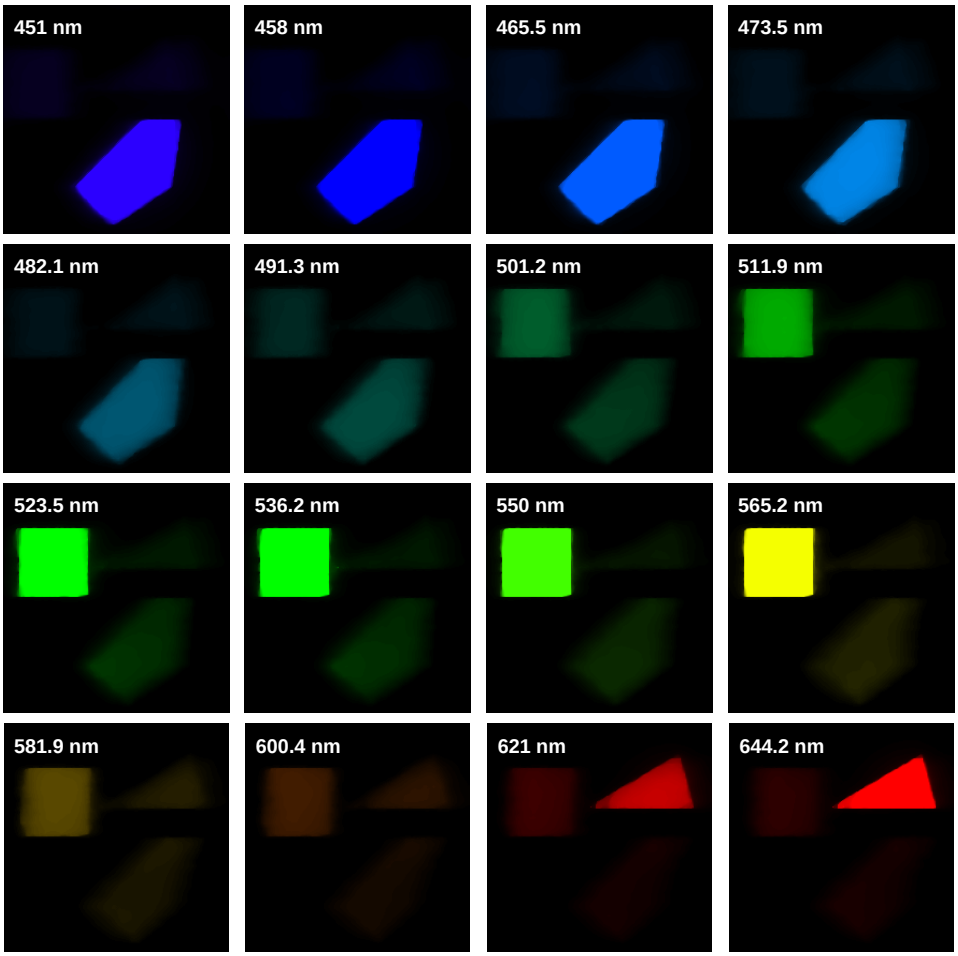

(a) Reconstruction of 16 channels by TwIST algorithm with tuning parameter $\tau = 0.05$

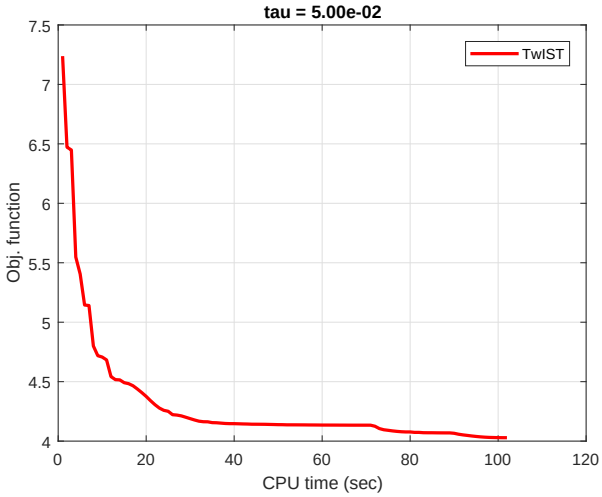

(b) Convergent rate curve of TwIST algorithm running estimate for the data of air gap of 4.64 mm

Figure 4.38: Reconstruction data for the measurement captured by the DP-CASSI with air gap of 4.64 mm.

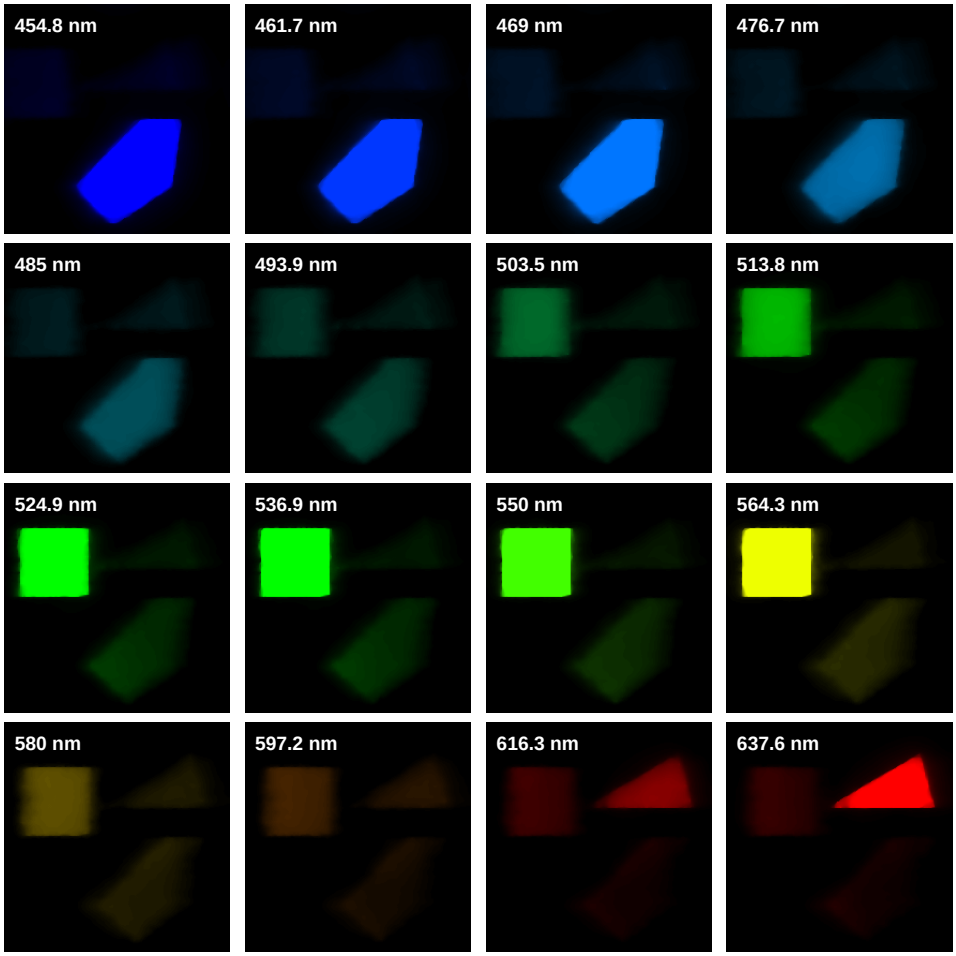

(a) Reconstruction of 16 channels by TwIST algorithm with tuning parameter $\tau = 0.05$

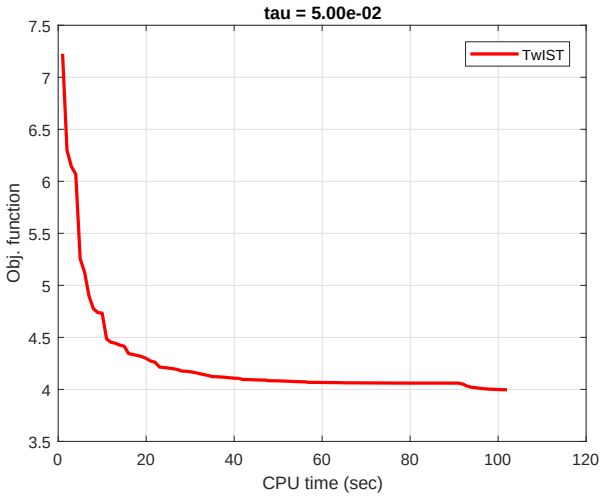

(b) Convergent rate curve of TwIST algorithm running estimate for the data of air gap of 5.04 mm

Figure 4.39: Reconstruction data for the measurement captured by the DP-CASSI with air gap of 5.04 mm.

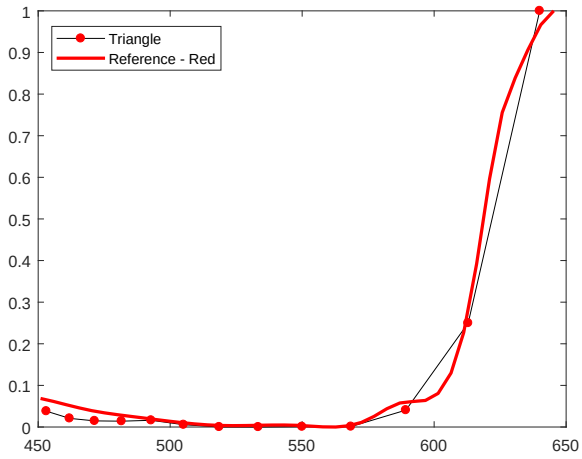

(a) Spectral estimate of Triangle object

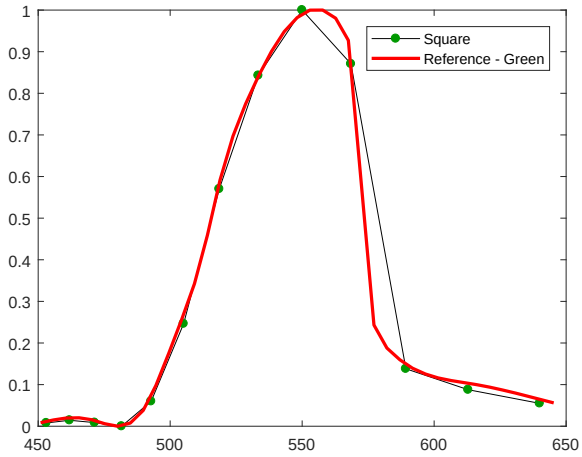

(b) Spectral estimate of Square object

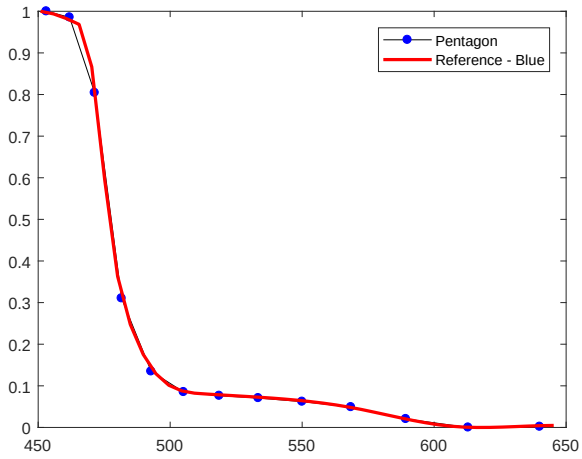

(c) Spectral estimate of Pentagon object

Figure 4.40: Estimate of spectral characteristics of three targets at air gap of 3.44 mm.

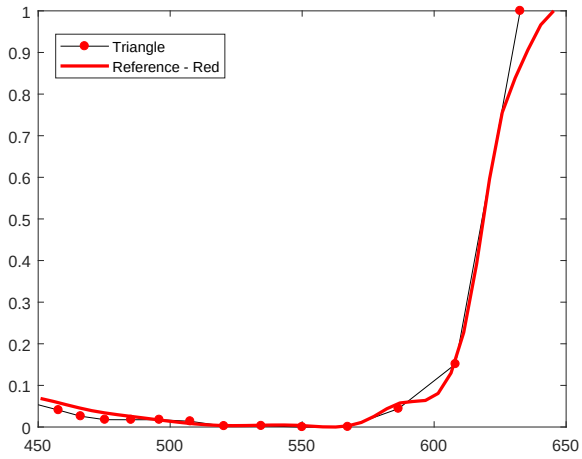

(a) Spectral estimate of Triangle object

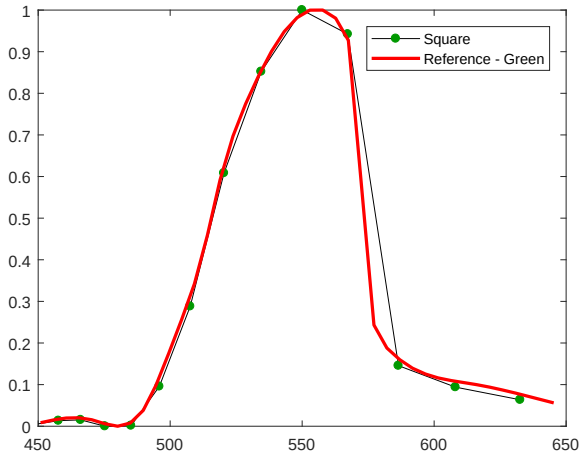

(b) Spectral estimate of Square object

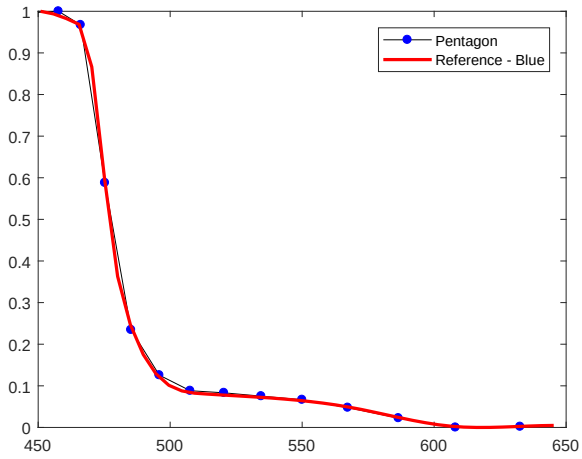

(c) Spectral estimate of Pentagon object

Figure 4.41: Estimate of spectral characteristics of three targets at air gap of 3.84 mm.

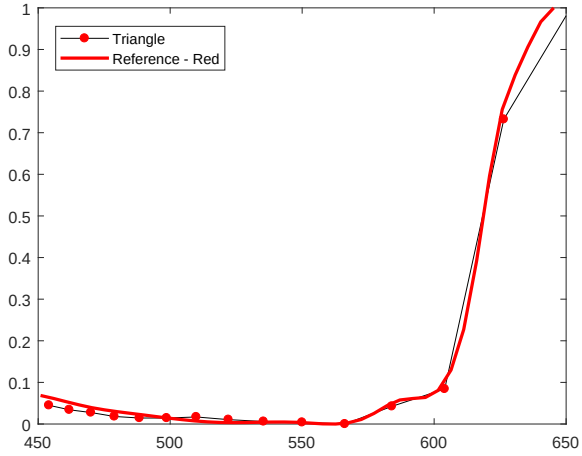

(a) Spectral estimate of Triangle object

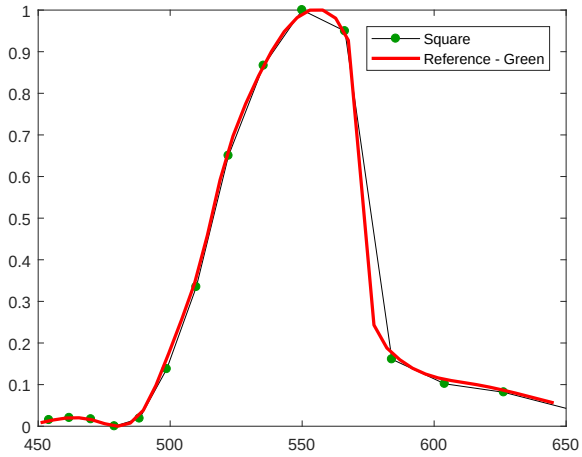

(b) Spectral estimate of Square object

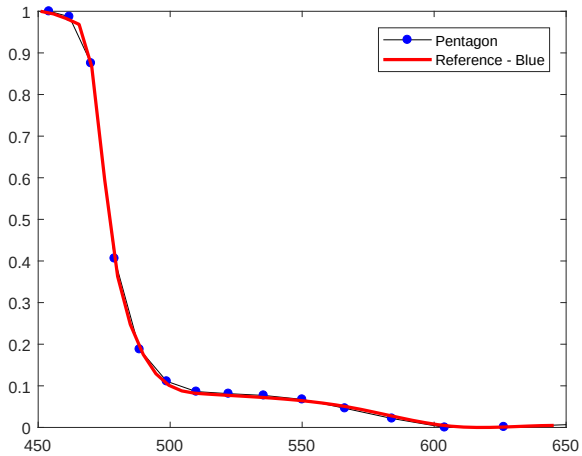

(c) Spectral estimate of Pentagon object

Figure 4.42: Estimate of spectral characteristics of three targets at air gap of 4.24 mm.

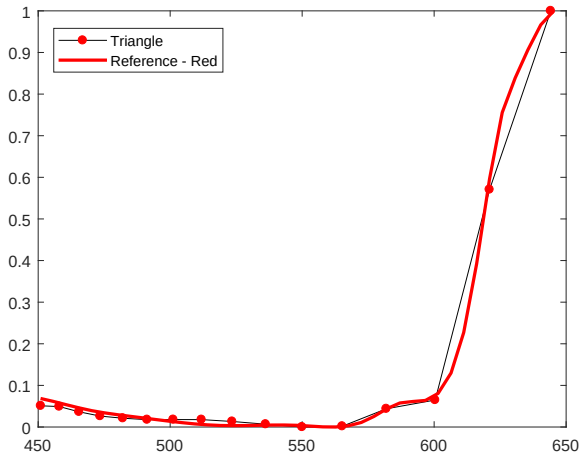

(a) Spectral estimate of Triangle object

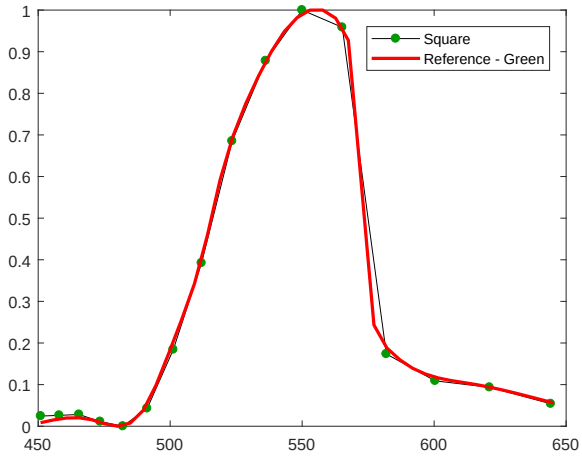

(b) Spectral estimate of Square object

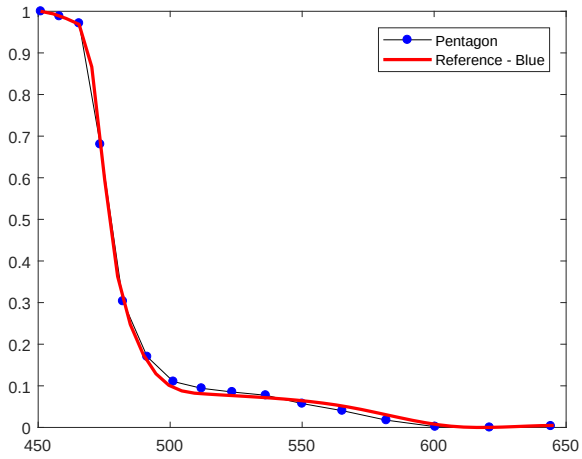

(c) Spectral estimate of Pentagon object

Figure 4.43: Estimate of spectral characteristics of three targets at air gap of 4.64 mm.

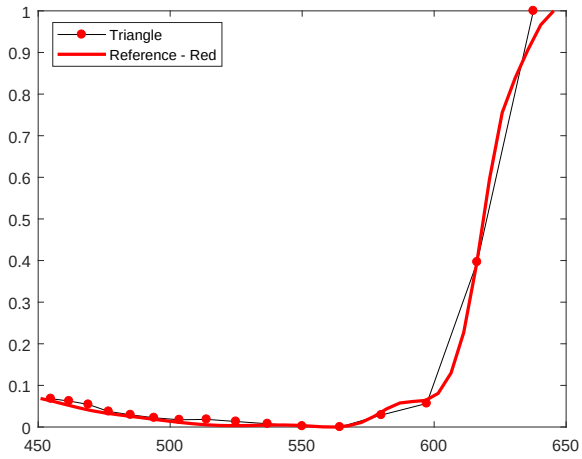

(a) Spectral estimate of Triangle object

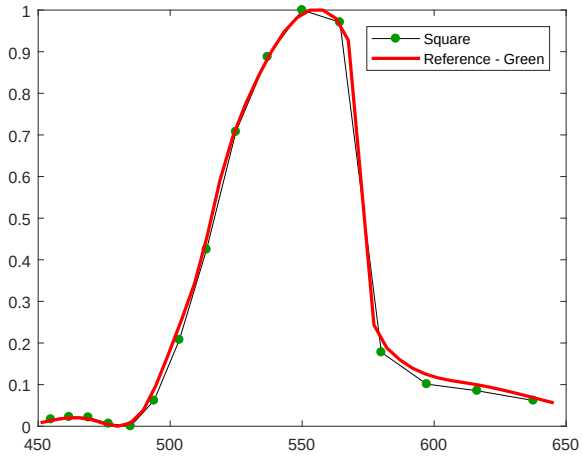

(b) Spectral estimate of Square object

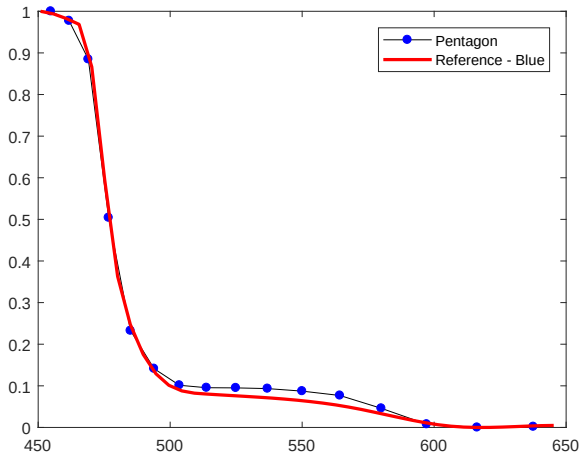

(c) Spectral estimate of Pentagon object

Figure 4.44: Estimate of spectral characteristics of three targets at air gap of 5.04 mm.

4.5.4 DP-CASSI Tolerance Analysis

The tolerance analysis of the DP-CASSI is to investigate the minimum distance of air gap yielding the wavelength shift for a better understanding of tuning wavelength. In our case, the shortest wavelength among calibration spectral bands in the second simulation of the DP-CASSI is 449.7 nm which yields maximum dispersion displacement due to Snell's law. Through Eq. (3.40) to Eq. (3.44), wavelength 449.7 nm has a displacement of -117.9397 µm relative to the central wavelength at air gap of 3.84 mm. The location of frame 449.7 nm can be found out to be [150:363, 168:381] at image plane through monochromatic illumination. The corresponding dispersion pixel sampled by pixel pitch 13 µm is -9. Therefore, to the tolerance of one pixel, which means control the location variation within [-9.5 -8.5], the corresponding range of air gap is [4.16 3.50]. The location of frame 449.7 nm at air gap of 4.16 mm and 3.50 mm is [150:363, 170:382] and [150:363, 167:380], which is controlled within the tolerance as the pixel pitch of monochromatic image is 6.5 µm which is $2\times$ sampling rate to dispersion pixel pitch, resulting in 2 pixels. Since the image used in reconstruction was sampled by pixel pitch of 6.5 µm, the range of air gap [4.16 3.50] would not represent the wavelength frame unshifted. Therefore, we further restricted the tolerance of air gap to control the wavelength totally unshifted. The resulting images in Fig. 4.45 shows the maximum air gap for unshifted pattern is between 3.76 mm and 3.88 mm, compared to the air gap 3.84 mm yielding calibration spectral band 449.7 nm. Calculating the Mean-Square-Error of cropped normalised frames as shown in Fig. 4.46, following

$$MSE = \frac{1}{N}\sum_{i=1}^{N}(I_i - J_i)^2, \tag{4.2}$$

where N is the total number of pixels. I denotes the pixel in the reference frame and J denotes the pixel in the comparison frame. The MSE between frame at 3.84 mm and 3.76 mm is 0.0197 and The MSE between frame at 3.88 mm and 3.76 mm is 0.0154. The tolerance in this case is -0.08 mm and 0.04 mm.

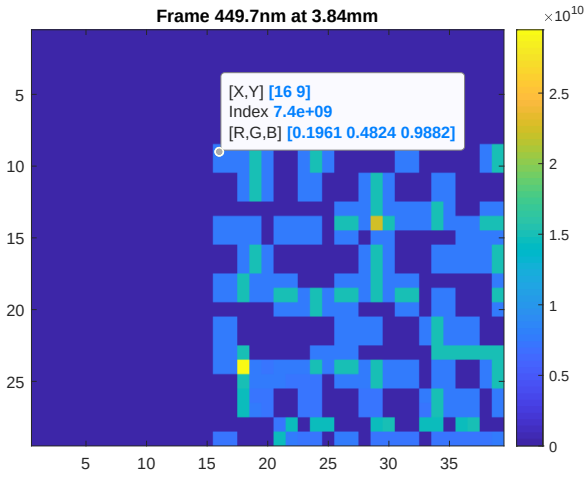

(a) Frame 449.7 nm at 3.84 mm

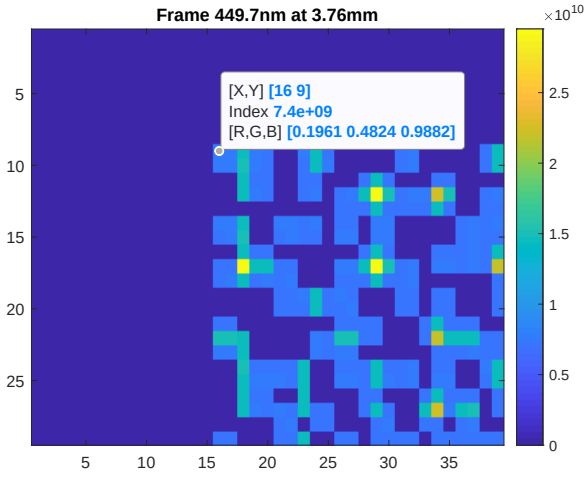

(b) Frame 449.7 nm at 3.76 mm

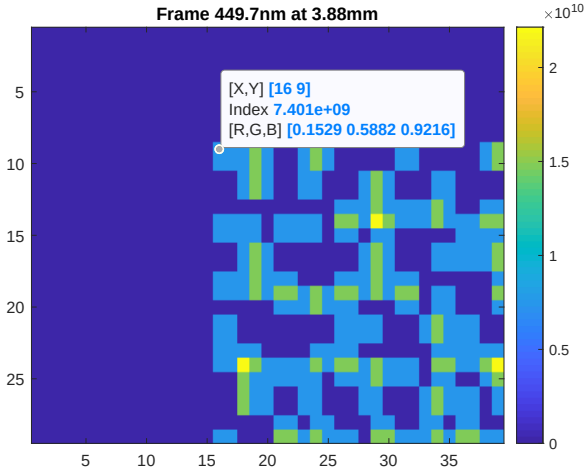

(c) Frame 449.7 nm at 3.88 mm

Figure 4.45: The air gap 3.76 mm and 3.88 mm are the minimum distance to keep wavelength 449.7 nm unshifted.

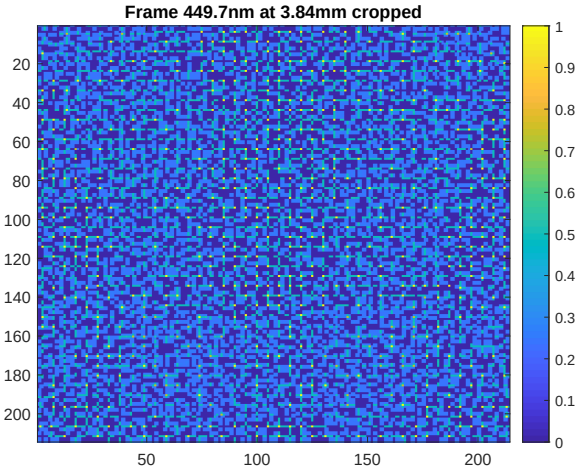

(a) Frame 449.7 nm at 3.84 mm

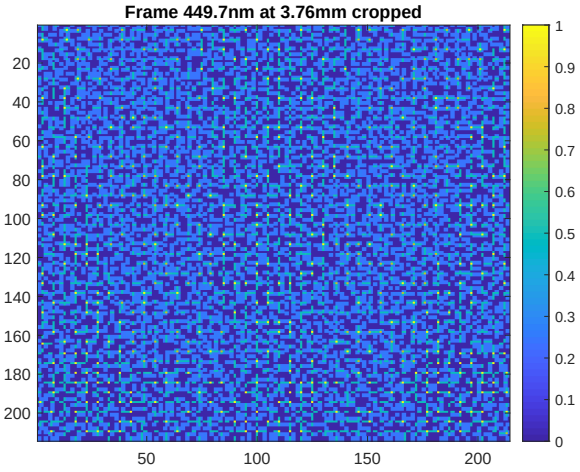

(b) Frame 449.7 nm at 3.76 mm

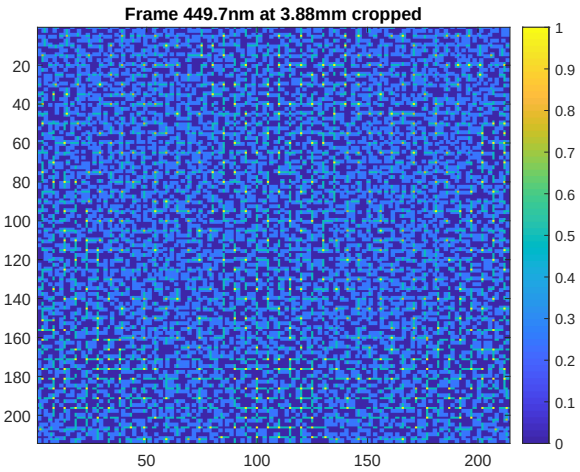

(c) Frame 449.7 nm at 3.88 mm

Figure 4.46: Cropped frame 449.7 nm at three air gaps: 3.84 mm, 3.76 mm and 3.88 mm.

Chapter 5

CONCLUSIONS

This PhD study concerns with Snapshot Spectral Imaging (SSI) technology specifically the enhancement of the Coded Aperture Snapshot Imaging (CASSI) system for future practical applications. The work including the structure improvement of SD-CASSI and the design of DP-CASSI has been done through the optical design software OSLO and the simulation software TracePro. CASSI fundamental properties with respect to the CS theory and optical design idea have been thoroughly understood by comparatively studing previous CASSI prototypes and improving one of them in terms of optical performance by simulation, which has built up a solid foundation. Based upon that, the DP-CASS has been proposed and achieved a novel snapshot spectral imager with dynamic wavelength tuneability in simulation. Lack of experimental verification needs to be accomplished in the future.

The detailed content of the thesis can be summarised as follows:

- Fundamental properties of CASSI system

    1. Optimisation of the Single-Disperser CASSI:

       Details of the design and optimisation of the Single-Prism CASSI (SP-CASSI) and the simulation of the Ultraviolet-Visible CASSI (UV-CASSI) using OSLO and ray tracing software TracePro have been given in this thesis. The optimisation was conducted with a mirror sets of two imaging optics which exhibits

small aberration even for relatively small focal length (25 mm) of the objective lens utilised in this study. Note that a virtual objective lens has been deployed in these CASSI systems for simulation and asymmetric distortions still exist with around 0.9% at 450 nm and 0.6% at 650 nm, due mainly to the aberrations intrinsic to the single prism. This aberration is seen to reduce somewhat when the single prism is replaced by the Double Amici prism which adopts a direct-view structure leading to a more symmetrical dispersion. As a comparison, the UV-CASSI configuration exhibits smaller aberration than that of the Double-Amici CASSI (DA-CASSI) when the dispersive element is placed in the collimating space of the relay lens (see below for more information).

2. Optical analysis of the DA-CASSI:

   The aberrations of the DA-CASSI for combinations of 5 groups of lens materials have been critically assessed in the thesis. The study concerns the effect of aberrations for various optics configurations of the DA-CASSI. The analysis revealed that the aberration was substantially increased when the Double Amici prism was placed at the system's focal range. This aberration was seen to reduce somewhat when the relative distances between the relay lens/double amici prism/detector were adjusted.

- Proposed spectral tuneable SSI in a Dual-Prism configuration (DP-CASSI)

1. Design and optimisation for the DP-CASSI:

   Details of the optical design and the performance of the spectral tuning assessed by ray tracing have been given. This may present a first study for using such simple optical components (pair of prisms) to achieve spectral tuning in the SSI system. The present work highlights the capability of the system and draws the attentions to areas where the system can be further developed for real application. The performance of the proposed DP-CASSI is validated by comparing the spectral characteristics of targets in the scene recovered from

the multiplex data and the ground truth spectra. Preliminary result has shown a 10 nm shift at 650 nm wavelength have been achieved in the present design when the air gap of the dual prism is changed from 3.44 mm to 5.04 mm. For the 13 µm pitch of the Focal Plane Array (FPA) detector utilised in this work, simulation experiments have shown that the air gap displacement tolerance at 450 mm region is around 0.08 mm.

2. Spectral accuracy assessment of DP-CASSI:

   The spectral accuracy of the de-compressed images have been examined by reducing the extent of multiplexing through a reduction of recovering bands from 50 to 15 bands.

   Table 5.1 gives a list of SSI systems studied during the course of this PhD research. Due to the lack of information about how the SSI systems are designed and optimised in the literature, this thesis is designed in such a way to provide a detailed step-to-step guide for new researchers in the field to explore the subject further.

Table 5.1: Main Optical Parameters in Four CASSI-based Snapshot Spectral Imagers.

Name	**F/#** No.	**Central Wavelength** nm	**Dispersion** No.	**Resolution** µm	**Prism** materials
SP-CASSI	F/4	587.56	32	13	BK7
DA-CASSI	F/8	550	33	9.9	NSK2/SF4
UV-CASSI	F/8	500	14	14.8	CaF2/FS
DP-CASSI	F/7.5	550	13-15	13	NSF11

5.1 Future Work

This PhD presents a first step of research to realise spectral tuning in the snapshot imaging (SSI) system. Due to the strong commercial potential of the topic, a lot of information regarding to the design and optimisation of the SSI is heavily lacking in the open domain. This research involves not only substantial literature search, but also a lot of trial and error

learning to unveil the reason why the system reported in the open domain has been proposed in such particular configuration. As a result, the project adopts very simple optics to test out the concept and there are observations which should be further investigated in order to take the tuneable SSI research into the next level:

- Issues of the dual prism location:

  The location of the dispersive element (dual-prism) critically affects the aberration of the system. The aberration will increase when the dispersive element is in the focal range of the last optical element of the system. Possible solutions may be the utilisation of a "negative" aberration of the dispersive element to counter or balance the aberration. Alternatively, a non-parallel dual-prism in the collimating space of the relay lens may reduce aberration. Furthermore, rotation of the second prism about its optical axis in the dual-prism structure would give another two more degrees of freedom (rotation angle and second prism's relative position) which could help optimisation further.

- Utilisation of zoom lens:

  Zoom lens will improve the adaptability of the SSI system but it may also increase the complexity for the adjustment of dispersion displacement and the balance of aberration.

- Reflective optics for aberration reduction:

  The utilisation of reflective optics instead of the transmission ones that presented in this work, may formulate a more promising next stage of research to realise a linear dispersion and negligible aberration in the future tuneable SSI system.

Appendix A

Academic Contributions

- **M. Ding**, P. WT Yuen, J. Piper, P. Godfree, A. Chatterjee, U. Zahidi M. Gunes, S. Selvagumar, D. James and M. Richardson, "Design of a tunable snapshot multispectral imaging system through ray tracing simulation", Jour. of Imag., 5(1), 9, 2019. doi.org/10.3390/jimaging5010009

- **M. Ding**, P. WT Yuen and M. Richardson, "Design of single prism coded aperture snapshot spectral imager using ray tracing simulation", IEEE British and Irish Conf. on Opt. and Pho., pp. 1-4, 2018. doi.org/10.1109/BICOP.2018.8658356

- J. Piper, P. WT Yuen, P. Godfree, **M. Ding**, U. Soori, S. Selvagumar and D. James, "Comparative noise performance of a coded aperture snapshot spectral imager", SPIE Defence + Security, 2016. doi.org/10.1117/12.2240926

- **M. Ding**, P. WT Yuen, U. Soori, S. Selvagumar, M. Gunes and U. Zahidi, "Enhanced CASSI snapshot imager using dual prism dispersion", Poster paper, Hyperspectral Imaging & Applications Conference, 2016.

- **M. Ding**, P. WT Yuen, J. Piper, P. Godfree, A. Chatterjee, U. Zahidi, Senthurran Selvagumar, D. James and M. Richardson, "Tuneable snapshot multispectral imaging system using a dual prism as dispersive element". *Submitted* to Optical Engineering, 2018 (review in progressing).

Appendix B

Simulation System Specifications

Single-Prism Coded Aperture Snapshot Spectral Imager Specifications.

*LENS DATA
SP-CASSI

SRF	RADIUS	THICKNESS	APERTURE RADIUS	GLASS	SPE	NOTE
OBJ	--	9.501817	0.832000	AIR		
1	38.523000	1.674000	4.010000 K	O_LAF2-O	C	
2	-38.523000	2.319000	4.010000 K	AIR		
3	8.404000	1.116000	3.010000 K	J-LAF3	C	
4	6.393000	2.935000	3.010000 K	AIR		
AST	--	0.586000	1.800000 AK	AIR		
6	-4.777000	2.902000	1.887819 K	BCDC20-60	C	
7	-4.107000	1.931000	2.657786 K	N-SF6	C	
8	-6.926000	0.260000	3.245591 K	AIR		
9	-95.674000	1.563000	5.010000 K	ULT20	C	
10	-11.399000	5.000000	5.010000 K	AIR		
11	--	13.856000	8.000000 X	BK7	C	*
12	--	--	8.000000 X	AIR		*
13	--	5.000000	10.000000	AIR		*
14	11.399000	1.563000	5.010000 K	ULT20	C	
15	95.674000	0.260000	5.010000 K	AIR		
16	6.926000	1.931000	4.000000 K	N-SF6	C	
17	4.107000	2.902000	3.500000 K	BCDC20-60	C	
18	4.777000	3.521000	2.480160 K	AIR		
19	-6.393000	1.116000	3.010000 K	J-LAF3	C	
20	-8.404000	2.319000	3.010000 K	AIR		
21	38.523000	1.674000	4.010000 K	O_LAF2-O	C	
22	-38.523000	9.501817	4.010000 K	AIR		
IMS	--	-0.040000	0.832000			*

Double-Amici Coded Aperture Snapshot Spectral Imager Specifications.

*LENS DATA
DA-CASSI

SRF	RADIUS		THICKNESS		APERTURE RADIUS		GLASS	SPE	NOTE
OBJ	--		39.300000		2.533400		AIR		
1	14.940000		2.400000		5.500000		H-ZLAF55A	C	
2	--		3.600004		5.000000		AIR		
3	-29.678000		2.400000		4.976000		H-ZF6	C	
4	14.760000		2.801000		3.992000		AIR		
5	205.600000		2.400000		4.000000		H-LAF10L	C	
6	-25.098000		0.749000		3.170000		AIR		
AST	--		0.749000		2.370000	A	AIR		
8	25.098000	P	2.400000	P	3.170000	P	H-LAF10L	P	
9	-205.600000	P	2.801000		4.000000	P	AIR		
10	-14.760000	P	2.400000	P	3.992000	P	H-ZF6	P	
11	29.678000	P	3.600000		4.976000	P	AIR		
12	--	P	2.400000	P	5.000000	P	H-ZLAF55A	P	
13	-14.940000	P	8.600000		5.500000	P	AIR		
14	--		4.000000		4.000000		N-SK2	C	*
15	--		4.000000		4.000000		SF4	C	*
16	--		4.000000		4.000000		N-SK2	C	*
17	--		23.200000		4.000000		AIR		*
IMS	--		--		2.523296	S			*

Ultraviolet-Visible Coded Aperture Snapshot Spectral Imager Specifications.

*LENS DATA
UV-CASSI

SRF	RADIUS	THICKNESS	APERTURE RADIUS	GLASS	SPE	NOTE
OBJ	--	40.000000	3.788800	AIR		
1	-23.730000	15.000000	11.190000	SILICA	C	
2	-26.360000	60.000000	13.730000	AIR		
3	54.550000	6.000000	12.880000	CAF2	C	
4	-78.550000	3.000000	12.610000	AIR		
5	-44.090000	2.500000	12.170000	N-BK7	C	
6	55.000000	2.000000	12.040000	AIR		
7	56.680000	6.000000	12.200000	CAF2	C	
8	-66.530000	40.000000	12.160000	AIR		
9	--	9.000000	8.220000 X	CAF2	C	*
10	--	--	8.390000 X	AIR		*
11	--	7.500000	8.390000 X	SILICA	C	*
AST	--	--	7.730000 AX	AIR		
13	--	7.500000 P	7.730000 X	SILICA	C	
14	--	--	8.340000 X	AIR		*
15	--	9.000000 P	8.340000 X	CAF2	C	*
16	--	40.000000 P	8.610000 X	AIR		*
17	66.530000 P	6.000000 P	12.640000	CAF2	C	
18	-56.680000 P	2.000000 P	12.670000	AIR		
19	-55.000000 P	2.500000 P	12.500000	N-BK7	C	
20	44.090000 P	3.000000 P	12.630000	AIR		
21	78.550000 P	6.000000 P	13.070000	CAF2	C	
22	-54.550000 P	60.000000 P	13.340000	AIR		
23	26.360000 P	15.000000 P	13.990000	SILICA	C	
24	23.730000 P	40.000000	11.450000	AIR		
IMS	--	--	3.799018 S			*

Air gap 3.44 mm Dual-Prism Coded Aperture Snapshot Spectral Imager Specifications.

*LENS DATA
DP-CASSI-3.44mm-air gap

SRF	RADIUS		THICKNESS		APERTURE RADIUS		GLASS	SPE	NOTE
OBJ	--		87.697656		0.832000		AIR		
1	35.013136	V	7.548419	V	15.891487		N-SK2	C	
2	294.154428	V	14.586192	V	15.891487		AIR		
3	-67.734240	V	2.513936	V	10.594325		N-SF2	C	
4	28.943338	V	8.083075	V	10.594325		AIR		
5	147.613195	V	10.104070	V	15.891487		N-SK2	C	
6	-33.689777	V	7.638574		15.891487		AIR		
AST	--		7.638574	P	10.594325	A	AIR		
8	33.689777	P	10.104070	P	15.891487	P	N-SK2	P	
9	-147.613195	P	8.083075	P	15.891487	P	AIR		
10	-28.943338	P	2.513936	P	10.594325	P	N-SF2	P	
11	67.734240	P	14.586192	P	10.594325	P	AIR		
12	-294.154428	P	7.548419	P	15.891487	P	N-SK2	P	
13	-35.013136	P	12.043007	V	15.891487	P	AIR		
14	--		7.165492	V	10.000000		N-SF11	C	*
15	--		3.443007	V	10.000000		AIR		*
16	--		7.165492	P	10.000000	P	N-SF11	P	*
17	--		56.104024	V	10.000000	P	AIR		*
IMS	--		-21.466391		5.297162				*

Air gap 3.84 mm Dual-Prism Coded Aperture Snapshot Spectral Imager Specifications.

*LENS DATA
DP-CASSI-3.84mm-air gap

SRF	RADIUS		THICKNESS		APERTURE RADIUS		GLASS	SPE	NOTE
OBJ	--		87.697656		0.832000		AIR		
1	35.013136	V	7.548419	V	15.891487		N-SK2	C	
2	294.154428	V	14.586192	V	15.891487		AIR		
3	-67.734240	V	2.513936	V	10.594325		N-SF2	C	
4	28.943338	V	8.083075	V	10.594325		AIR		
5	147.613195	V	10.104070	V	15.891487		N-SK2	C	
6	-33.689777	V	7.638574		15.891487		AIR		
AST	--		7.638574	P	10.594325	A	AIR		
8	33.689777	P	10.104070	P	15.891487	P	N-SK2	P	
9	-147.613195	P	8.083075	P	15.891487	P	AIR		
10	-28.943338	P	2.513936	P	10.594325	P	N-SF2	P	
11	67.734240	P	14.586192	P	10.594325	P	AIR		
12	-294.154428	P	7.548419	P	15.891487	P	N-SK2	P	
13	-35.013136	P	12.043007	V	15.891487	P	AIR		
14	--		7.165492	V	10.000000		N-SF11	C	*
15	--		3.843007	V	10.000000		AIR		*
16	--		7.165492	P	10.000000	P	N-SF11	P	*
17	--		56.104024	V	10.000000	P	AIR		*
IMS	--		-21.927942		5.297162				*

Air gap 4.24 mm Dual-Prism Coded Aperture Snapshot Spectral Imager Specifications.

*LENS DATA
DP-CASSI-4.24mm-air gap

SRF	RADIUS		THICKNESS		APERTURE RADIUS		GLASS	SPE	NOTE
OBJ	--		87.697656		0.832000		AIR		
1	35.013136	V	7.548419	V	15.891487		N-SK2	C	
2	294.154428	V	14.586192	V	15.891487		AIR		
3	-67.734240	V	2.513936	V	10.594325		N-SF2	C	
4	28.943338	V	8.083075	V	10.594325		AIR		
5	147.613195	V	10.104070	V	15.891487		N-SK2	C	
6	-33.689777	V	7.638574		15.891487		AIR		
AST	--		7.638574	P	10.594325	A	AIR		
8	33.689777	P	10.104070	P	15.891487	P	N-SK2	P	
9	-147.613195	P	8.083075	P	15.891487	P	AIR		
10	-28.943338	P	2.513936	P	10.594325	P	N-SF2	P	
11	67.734240	P	14.586192	P	10.594325	P	AIR		
12	-294.154428	P	7.548419	P	15.891487	P	N-SK2	P	
13	-35.013136	P	12.043007	V	15.891487	P	AIR		
14	--		7.165492	V	10.000000		N-SF11	C	*
15	--		4.243007		10.000000		AIR		*
16	--		7.165492	P	10.000000	P	N-SF11	P	*
17	--		56.104024		10.000000	P	AIR		*
IMS	--		-22.504322		5.297162				*

Air gap 4.64 mm Dual-Prism Coded Aperture Snapshot Spectral Imager Specifications.

*LENS DATA
DP-CASSI-4.64mm-air gap

SRF	RADIUS		THICKNESS		APERTURE RADIUS		GLASS	SPE	NOTE
OBJ	--		87.697656		0.832000		AIR		
1	35.013136	V	7.548419	V	15.891487		N-SK2	C	
2	294.154428	V	14.586192	V	15.891487		AIR		
3	-67.734240	V	2.513936	V	10.594325		N-SF2	C	
4	28.943338	V	8.083075	V	10.594325		AIR		
5	147.613195	V	10.104070	V	15.891487		N-SK2	C	
6	-33.689777	V	7.638574		15.891487		AIR		
AST	--		7.638574	P	10.594325	A	AIR		
8	33.689777	P	10.104070	P	15.891487	P	N-SK2	P	
9	-147.613195	P	8.083075	P	15.891487	P	AIR		
10	-28.943338	P	2.513936	P	10.594325	P	N-SF2	P	
11	67.734240	P	14.586192	P	10.594325	P	AIR		
12	-294.154428	P	7.548419	P	15.891487	P	N-SK2	P	
13	-35.013136	P	12.043007	V	15.891487	P	AIR		
14	--		7.165492	V	10.000000		N-SF11	C	*
15	--		4.643007	V	10.000000		AIR		*
16	--		7.165492	P	10.000000	P	N-SF11	P	*
17	--		56.104024	V	10.000000	P	AIR		*
IMS	--		-23.269040		5.297162				*

Air gap 5.04 mm Dual-Prism Coded Aperture Snapshot Spectral Imager Specifications.

*LENS DATA
DP-CASSI-5.04mm-air gap

SRF	RADIUS		THICKNESS		APERTURE RADIUS		GLASS	SPE	NOTE
OBJ	--		87.697656		0.832000		AIR		
1	35.013136	V	7.548419	V	15.891487		N-SK2	C	
2	294.154428	V	14.586192	V	15.891487		AIR		
3	-67.734240	V	2.513936	V	10.594325		N-SF2	C	
4	28.943338	V	8.083075	V	10.594325		AIR		
5	147.613195	V	10.104070	V	15.891487		N-SK2	C	
6	-33.689777	V	7.638574		15.891487		AIR		
AST	--		7.638574	P	10.594325	A	AIR		
8	33.689777	P	10.104070	P	15.891487	P	N-SK2	P	
9	-147.613195	P	8.083075	P	15.891487	P	AIR		
10	-28.943338	P	2.513936	P	10.594325	P	N-SF2	P	
11	67.734240	P	14.586192	P	10.594325	P	AIR		
12	-294.154428	P	7.548419	P	15.891487	P	N-SK2	P	
13	-35.013136	P	12.043007	V	15.891487	P	AIR		
14	--		7.165492	V	10.000000		N-SF11	C	*
15	--		5.043007	V	10.000000		AIR		*
16	--		7.165492	P	10.000000	P	N-SF11	P	*
17	--		56.104024	V	10.000000	P	AIR		*
IMS	--		-23.542253		5.297162				*

REFERENCES

[1] M. Descour and E. Dereniak. Computed-tomography imaging spectrometer: experimental calibration and reconstruction results. *Applied Optics*, 34(22):4817–4826, 1995.

[2] D. Ren and J. Allington-Smith. On the application of integral field unit design theory for imaging spectroscopy. *Publications of the Astronomical Society of the Pacific*, 114(798):866, Aug 2002.

[3] M. Aikio and V. T. Tutkimuskeskus. *Hyperspectral prism-grating-prism imaging spectrograph*. Technical Research Centre of Finland, 2001.

[4] W. J. Smith. *Modern optical engineering*. Tata McGraw-Hill Education, 1966.

[5] G. A. Shaw and H. K. Burke. Spectral imaging for remote sensing. *Lincoln laboratory journal*, 14(1):3–28, 2003.

[6] C. O. Davis *et al.* Ocean phills hyperspectral imager: design, characterization, and calibration. *Optics Express*, 10(4):210–221, 2002.

[7] M. A. Folkman, J. Pearlman, L. B. Liao, and P. J. Jarecke. Eo-1/hyperion hyperspectral imager design, development, characterization, and calibration. In *Hyperspectral Remote Sensing of the Land and Atmosphere*, volume 4151, pages 40–52. International Society for Optics and Photonics, 2001.

[8] N. Gat. Imaging spectroscopy using tunable filters: a review. In *Wavelet Applications VII*, volume 4056, pages 50–65. International Society for Optics and Photonics, April 2000.

[9] R. Lu. Multispectral imaging for predicting firmness and soluble solids content of apple fruit. *Postharvest Biology and Technology*, 31(2):147–157, 2004.

[10] Y. Bromberg, O. Katz, and Y. Silberberg. Ghost imaging with a single detector. *Physical Review A*, 79(5):053840, 2009.

[11] O. Katz, Y. Bromberg, and Y. Silberberg. Compressive ghost imaging. *Applied Physics Letters*, 95(13):131110, 2009.

[12] B. Sun, S. S. Welsh, M. P. Edgar, J. H. Shapiro, and M. J. Padgett. Normalized ghost imaging. *Optics Express*, 20(15):16892–16901, 2012.

[13] B. Zitova and J. Flusser. Image registration methods: a survey. *Image and vision computing*, 21(11):977–1000, 2003.

[14] R. Eckhorn, H. J Reitboeck, Mt Arndt, and P Dicke. Feature linking via synchronization among distributed assemblies: Simulations of results from cat visual cortex. *Neural computation*, 2(3):293–307, 1990.

[15] H. Chao *et al.* Band-reconfigurable multi-uav-based cooperative remote sensing for real-time water management and distributed irrigation control. *IFAC Proceedings Volumes*, 41(2):11744–11749, 2008.

[16] Y. Du, P. M Teillet, and J. Cihlar. Radiometric normalization of multitemporal high-resolution satellite images with quality control for land cover change detection. *Remote sensing of Environment*, 82(1):123–134, 2002.

[17] C. Chang. *Hyperspectral imaging: techniques for spectral detection and classification*, volume 1. Springer Science & Business Media, 2003.

[18] V. Pasqualini *et al.* Use of spot 5 for mapping seagrasses: An application to posidonia oceanica. *Remote Sensing of Environment*, 94(1):39–45, 2005.

[19] J. R. Jensen and D. C. Cowen. Remote sensing of urban/suburban infrastructure and socio-economic attributes. *Photogrammetric engineering and remote sensing*, 65:611–622, 1999.

[20] H. Fujisada. Design and performance of aster instrument. In *Advanced and next-generation satellites*, volume 2583, pages 16–26. International Society for Optics and Photonics, 1995.

[21] Iwasaki *et al.* A. Enhancement of spectral separation performance for aster/swir. In *Infrared spaceborne remote sensing IX*, volume 4486, pages 42–51. International Society for Optics and Photonics, 2002.

[22] L. J. Allison and E. A. Neil. Final report on the tiros 1 meteorological satellite system. *NASATech. Rep*, 1962.

[23] J. E. Conel *et al.* Airborne imaging spectrometer-2: Radiometric spectral characteristics and comparison of ways to compensate for the atmosphere. In *Imaging spectroscopy II*, volume 834, pages 140–158. International Society for Optics and Photonics, January 1987.

[24] D. A. Roberts, M. O. Smith, and J. B. Adams. Green vegetation, nonphotosynthetic vegetation, and soils in aviris data. *Remote Sensing of Environment*, 44(2-3):255–269, June 1993.

[25] A. Coradini *et al.* Ma_miss: Mars multispectral imager for subsurface studies. *Advances in Space Research*, 28(8):1203–1208, 2001.

[26] J. Bendig, A. Bolten, and G. Bareth. Introducing a low-cost mini-uav for thermal- and multispectral-imaging. *Int. Arch. Photogramm. Remote Sens. Spat. Inf. Sci*, 39:345–349, 2012.

[27] M. Watanabe *et al.* Msi: a visible multispectral imager for 1.6-m telescope of hokkaido university. In *Ground-based and Airborne Instrumentation for Astronomy IV*, volume 8446, page 84462O. International Society for Optics and Photonics, 2012.

[28] L. Kong *et al.* Developing handheld real time multispectral imager to clinically detect erythema in darkly pigmented skin. In *Multimodal Biomedical Imaging V*, volume 7557, page 75570G. International Society for Optics and Photonics, 2010.

[29] G. A. Maul and H. R. Gordon. On the Use of the Earth Resources Technology Satellite (LANDSAT-1) in Optical Oceanography. *Remote Sensing of Environment*, 4:95 – 128, 1975.

[30] R. W. Reich and R. Price. Detection and classification of forest damage caused by tomentosus root rot using an airborne multispectral imager (casi). In *Proceedings of the International forum on Automated interpretation of high spatial resolution digital imagery for forestry*, pages 179–185, 1998.

[31] M. S. Robinson, P. C. Thomas, J. Veverka, S. L. Murchie, and B. B. Wilcox. The geology of 433 eros. *Meteoritics & Planetary Science*, 37(12):1651–1684, 2002.

[32] A. Rachedi, N. Hadj-Sahraoui, and A. Brewer. Alsat-1: First results of multispectral imager. In *The XXth international Congress for Photogrammetric and remote sensing, Turkey*. Citeseer, 2004.

[33] R. M. Levenson and J. R. Mansfield. Multispectral imaging in biology and medicine: slices of life. *Cytometry A*, 69(8):748–758, August 2006.

[34] T. Borregaard, H. Nielsen, L. Nørgaard, and H. Have. Crop–weed Discrimination by Line Imaging Spectroscopy. *Journal of Agricultural Engineering Research*, 75(4):389 – 400, April 2000.

[35] N. Gupta, P. R. Ashe, and S. Tan. Miniature snapshot multispectral imager. *Optical Engineering*, 50(3):033203, 2011.

[36] H. Zeng *et al.* Miniature spectrometer and multispectral imager as a potential diagnostic aid in dermatology. In *Advances in Laser and Light Spectroscopy to Diagnose Cancer and Other Diseases II*, volume 2387, pages 57–62. International Society for Optics and Photonics, 1995.

[37] J. A. J. Berni *et al.* Remote sensing of vegetation from uav platforms using lightweight multispectral and thermal imaging sensors. *Int. Arch. Photogramm. Remote Sens. Spatial Inform. Sci*, 38(6), 2009.

[38] J. Veverka *et al.* An overview of the near multispectral imager-near-infrared spectrometer investigation. *Journal of Geophysical Research: Planets*, 102(E10):23709–23727, 1997.

[39] R. K. Rowe. Multispectral imaging biometrics, December 2 2008. US Patent 7,460,696.

[40] D. Yi *et al.* Real-time multispectral imager for home-based health care. *IEEE Transactions on Biomedical Engineering*, 58(3):736–740, 2011.

[41] J. Qin *et al.* Hyperspectral and multispectral imaging for evaluating food safety and quality. *Journal of Food Engineering*, 118(2):157–171, 2013.

[42] A. C. Goldberg, B. Stann, and N. Gupta. Multispectral, hyperspectral, and three-dimensional imaging research at the us army research laboratory. Technical report, ARMY RESEARCH LAB ADELPHI MD, 2003.

[43] B. Rafert *et al.* Hyperspectral imaging Fourier transform spectrometers for astronomical and remote sensing observations. In *Instrumentation in Astronomy VIII*, volume 2198, pages 338–350. International Society for Optics and Photonics, June 1994.

[44] E. K. Hege, D. O'Connell, W. Johnson, S. Basty, and E. L. Dereniak. Hyperspectral imaging for astronomy and space surviellance. In *Imaging Spectrometry IX*, volume 5159, pages 380–392. International Society for Optics and Photonics, 2004.

[45] A. A. Gowen, M. Taghizadeh, and C. P. O'Donnell. Identification of mushrooms subjected to freeze damage using hyperspectral imaging. *Journal of Food Engineering*, 93(1):7–12, 2009.

[46] D. Lorente *et al.* Recent Advances and Applications of Hyperspectral Imaging for Fruit and Vegetable Quality Assessment. *Food Bioprocess Technol*, 5(4):1121–1142, May 2012.

[47] B. S. Sorg, B. J. Moeller, O. Donovan, Y. Cao, and M. W. Dewhirst. Hyperspectral imaging of hemoglobin saturation in tumor microvasculature and tumor hypoxia development. *Journal of biomedical optics*, 10(4):044004, 2005.

[48] R. Schultz *et al.* Hyperspectral imaging: A novel approach for microscopic analysis. *Cytometry*, 43(4):239–247, April 2001.

[49] J. W. Uhr *et al.* Molecular profiling of individual tumor cells by hyperspectral microscopic imaging. *Translational Research*, 159(5):366 – 375, May 2012.

[50] P. WT Yuen and M. Richardson. An introduction to hyperspectral imaging and its application for security, surveillance and target acquisition. *The Imaging Science Journal*, 58(5):241–253, October 2010.

[51] M. J. Barnsley *et al.* The proba/chris mission: A low-cost smallsat for hyperspectral multiangle observations of the earth surface and atmosphere. *IEEE Transactions on Geoscience and Remote Sensing*, 42(7):1512–1520, 2004.

[52] N. Tack, A. Lambrechts, P. Soussan, and L. Haspeslagh. A compact, high-speed, and low-cost hyperspectral imager. In *Silicon Photonics VII*, volume 8266, page 82660Q. International Society for Optics and Photonics, 2012.

[53] T. Svensson *et al.* Design, calibration and characterization of a low-cost spatial fourier transform lwir hyperspectral imaging camera with spatial and temporal scanning modes. In *Algorithms and Technologies for Multispectral, Hyperspectral, and Ultraspectral Imagery XXIV*, volume 10644, page 106440X. International Society for Optics and Photonics, 2018.

[54] XIMEA - Hyperspectral cameras with USB3. https://www.ximea.com/en/usb3-vision-camera/hyperspectral-usb3-cameras-mini. Accessed 5 April 2019.

[55] RTK X8 Hyperspectral Mapping. https://cubert-gmbh.com/product/rtk-x8-hyperspectral-mapping/. Accessed 5 April 2019.

[56] HySpex Cameras. https://www.hyspex.no/products/. Accessed 5 April 2019.

[57] J. Jemec, F. Pernuš, B. Likar, and M. Bürmen. Deconvolution-based restoration of swir pushbroom imaging spectrometer images. *Opt. Express*, 24(21):24704–24718, October 2016.

[58] P. Mouroulis *et al.* Landsat-swath imaging spectrometer design. In *Current Developments in Lens Design and Optical Engineering XVI*, volume 9578, page 95780A. International Society for Optics and Photonics, January 2015.

[59] R. O. Green *et al.* Imaging spectroscopy and the airborne visible/infrared imaging spectrometer (aviris). *Remote Sensing of Environment*, 65(3):227 – 248, September 1998.

[60] A. Wagadarikar, R. John, R. Willett, and D. J. Brady. Single disperser design for coded aperture snapshot spectral imaging. *Applied optics*, 47(10):B44–B51, Apr 2008.

[61] L. Gao, R. T. Kester, and T. S. Tkaczyk. Compact image slicing spectrometer (iss) for hyperspectral fluorescence microscopy. *Optics express*, 17(15):12293–12308, Jul 2009.

[62] L. Gao, R. T. Kester, N. Hagen, and T. S. Tkaczyk. Snapshot image mapping spectrometer (ims) with high sampling density for hyperspectral microscopy. *Optics express*, 18(14):14330–14344, 2010.

[63] Y. Murakami, M. Yamaguchi, and N. Ohyama. Hybrid-resolution multispectral imaging using color filter array. *Optics express*, 20(7):7173–7183, 2012.

[64] X. Yuan *et al.* Compressive hyperspectral imaging with side information. *IEEE Journal of Selected Topics in Signal Processing*, 9(6):964–976, September 2015.

[65] N. A. Hagen, L. S. Gao, T. S. Tkaczyk, and R. T. Kester. Snapshot advantage: a review of the light collection improvement for parallel high-dimensional measurement systems. *Optical Engineering*, 51(11):111702, Jun 2012.

[66] K. C. Lawrence, B. Park, W. R. Windham, and C. Mao. Calibration of a pushbroom hyperspectral imaging system for agricultural inspection. *Transactions of the ASAE*, 46(2):513, mar 2003.

[67] H. Arguello, H. F. Rueda, and G. R. Arce. Spatial super-resolution in code aperture spectral imaging. In *Compressive Sensing*, volume 8365, page 83650A. International Society for Optics and Photonics, Jun 2012.

[68] N. Gupta. Hyperspectral imager development at army research laboratory. In *Infrared Technology and Applications XXXIV*, volume 6940, page 69401P. International Society for Optics and Photonics, April 2008.

[69] J. Antila *et al.* Spectral imaging device based on a tuneable mems fabry-perot interferometer. In *Next-Generation Spectroscopic Technologies V*, volume 8374, page 83740F. International Society for Optics and Photonics, May 2012.

[70] M. Ebermann *et al.* Tunable mems fabry-pérot filters for infrared microspectrometers: a review. In *MOEMS and Miniaturized Systems XV*, volume 9760, page 97600H. International Society for Optics and Photonics, Mar 2016.

[71] N. A. Hagen and M. W. Kudenov. Review of snapshot spectral imaging technologies. *Optical Engineering*, 52(9):090901, September 2013.

[72] X. Cao *et al.* Computational snapshot multispectral cameras: Toward dynamic capture of the spectral world. *IEEE Signal Processing Magazine*, 33(5):95–108, September 2016.

[73] M. R. Descour and E. L. Dereniak. Nonscanning no-moving-parts imaging spectrometer. In *Imaging Spectrometry*, volume 2480, pages 48–65. International Society for Optics and Photonics, June 1995.

[74] J. F. Scholl, E. K. Hege, D. G. O'Connell, and E. L. Dereniak. Hyperspectral datacube estimations of binary stars with the computed tomographic imaging spectrometer (ctis). In *Imaging Spectrometry XV*, volume 7812, page 78120I. International Society for Optics and Photonics, August 2010.

[75] M. R. Descour *et al.* Demonstration of a high-speed nonscanning imaging spectrometer. *Optics letters*, 22(16):1271–1273, Aug 1997.

[76] W. R. Johnson *et al.* Snapshot hyperspectral imaging in ophthalmology. *Journal of biomedical optics*, 12(1):014036, February 2007.

[77] H. H. Barrett and W. Swindell. Radiological imaging: The theory of image formation, detection, and processing academic. *New York*, 1, 1981.

[78] A. Gorman, D. W. Fletcher-Holmes, and A. R. Harvey. Generalization of the lyot filter and its application to snapshot spectral imaging. *Optics express*, 18(6):5602–5608, Mar 2010.

[79] A. R. Harvey, D. W. Fletcher-Holmes, S. S. Kudesia, and Ciaran. B. Imaging spectrometry at visible and infrared wavelengths using image replication. In *Electro-Optical and Infrared Systems: Technology and Applications*, volume 5612, pages 190–199. International Society for Optics and Photonics, Dec 2004.

[80] B. Lyot. Optical apparatus with wide field using interference of polarized light. *CR Acad. Sci.(Paris)*, 197(1593), 1933.

[81] C. Vanderriest. Integral field spectroscopy with optical fibres. *International Astronomical Union Colloquium*, 149:209–218, Apr 1995.

[82] S. C. Barden and R. A. Wade. Densepak and spectral imaging with fiber optics. In *Fiber optics in astronomy*, volume 3, pages 113–124, jan 1988.

[83] C. Chen, R. O. Reynolds, and A. Kost. Origin of spectral modal noise in fiber-coupled spectrographs. *Applied Optics*, 45(3):519–527, Jan 2006.

[84] G. R. Arce *et al.* Compressive coded aperture spectral imaging: An introduction. *IEEE Signal Processing Magazine*, 31(1):105–115, December 2014.

[85] Z. Xiong *et al.* Snapshot hyperspectral light field imaging. In *The IEEE Conference on Computer Vision and Pattern Recognition (CVPR)*, volume 2, jul 2017.

[86] H. Rueda, C. Fu, D. L. Lau, and G. R. Arce. Single aperture spectral+ tof compressive camera: Toward hyperspectral+ depth imagery. *IEEE Journal of Selected Topics in Signal Processing*, 11(7):992–1003, Aug 2017.

[87] X. Zhao *et al.* Optimization of compressive 4d-spatio-spectral snapshot imaging. In *AOPC 2017: 3D Measurement Technology for Intelligent Manufacturing*, volume 10458, page 1045815. International Society for Optics and Photonics, oct 2017.

[88] Y. Wu, I. O. Mirza, G. R. Arce, and D. W. Prather. Development of a digital-micromirror-device-based multishot snapshot spectral imaging system. *Optics letters*, 36(14):2692–2694, Jul 2011.

[89] C. V. Correa, H. Arguello, and G. R. Arce. Compressive spectral imaging with colored-patterned detectors. In *Acoustics, Speech and Signal Processing (ICASSP), 2014 IEEE International Conference on*, pages 7789–7793. IEEE, jul 2014.

[90] T. Tsai *et al.* Spectral-temporal compressive imaging. *Optics letters*, 40(17):4054–4057, July 2015.

[91] L. Wang, Z. Xiong, D. Gao, G. Shi, and F. Wu. Dual-camera design for coded aperture snapshot spectral imaging. *Applied optics*, 54(4):848–858, Feb 2015.

[92] D. L. Donoho. Compressed sensing. *IEEE Transactions on Information Theory*, 52(4):1289–1306, April 2006.

[93] E. J. Candes, J. Romberg, and T. Tao. Robust uncertainty principles: exact signal reconstruction from highly incomplete frequency information. *IEEE Transactions on Information Theory*, 52(2):489–509, February 2006.

[94] E. Candes and J. Romberg. Sparsity and incoherence in compressive sampling. *Inverse problems*, 23(3):969, April 2007.

[95] M. E. Gehm *et al.* Single-shot compressive spectral imaging with a dual-disperser architecture. *Optics express*, 15(21):14013–14027, Oct 2007.

[96] A. A. Wagadarikar, N. P. Pitsianis, X. Sun, and D. J. Brady. Spectral image estimation for coded aperture snapshot spectral imagers. In *Image Reconstruction from Incomplete Data V*, volume 7076, page 707602. International Society for Optics and Photonics, September 2008.

[97] D. Kittle, K. Choi, A. A. Wagadarikar, and D. J. Brady. Multiframe image estimation for coded aperture snapshot spectral imagers. *Applied optics*, 49(36):6824–6833, Dec 2010.

[98] D. S. Kittle, D. L. Marks, and D. J. Brady. Design and fabrication of an ultraviolet-visible coded aperture snapshot spectral imager. *Optical Engineering*, 51(7):071403, May 2012.

[99] M. H. Kim *et al.* 3d imaging spectroscopy for measuring hyperspectral patterns on solid objects. *ACM Transactions on Graphics (TOG)*, 31(4):38, 2012.

[100] John C Price. Spectral band selection for visible-near infrared remote sensing: spectral-spatial resolution tradeoffs. *IEEE Transactions on Geoscience and Remote Sensing*, 35(5):1277–1285, 1997.

[101] J. P. Kerekes and S. M. Hsu. Spectral quality metrics for vnir and swir hyperspectral imagery. In *Algorithms and Technologies for Multispectral, Hyperspectral, and Ultraspectral Imagery X*, volume 5425, pages 549–558. International Society for Optics and Photonics, 2004.

[102] H. Rueda, H. Arguello, and G. R. Arce. Dual-arm vis/nir compressive spectral imager. In *Image Processing (ICIP), 2015 IEEE International Conference on*, pages 2572–2576. IEEE, 2015.

[103] X. Xiao, B. Javidi, and A. Martinez-Corral, M.and Stern. Advances in three-dimensional integral imaging: sensing, display, and applications. *Applied optics*, 52(4):546–560, 2013.

[104] J. Jang and B. Javidi. Three-dimensional projection integral imaging using micro-convex-mirror arrays. *Optics Express*, 12(6):1077–1083, 2004.

[105] M. Lustig, D. Donoho, and J. M. Pauly. Sparse mri: The application of compressed sensing for rapid mr imaging. *Magnetic Resonance in Medicine: An Official Jour-*

nal of the International Society for Magnetic Resonance in Medicine, 58(6):1182–1195, 2007.

[106] Y. Yang, J. Sun, H. Li, and Z. Xu. Admm-net: A deep learning approach for compressive sensing mri. *arXiv preprint arXiv:1705.06869*, 2017.

[107] M. T. Alonso, P. López-Dekker, and J. J. Mallorquí. A novel strategy for radar imaging based on compressive sensing. *IEEE Transactions on Geoscience and Remote Sensing*, 48(12):4285–4295, 2010.

[108] J. H. G. Ender. On compressive sensing applied to radar. *Signal Processing*, 90(5):1402–1414, 2010.

[109] E. J. Candes and M. B. Wakin. An introduction to compressive sampling. *IEEE Signal Processing Magazine*, 25(2):21–30, March 2008.

[110] Y. Zhang *et al.* A review of compressive sensing in information security field. *IEEE access*, 4:2507–2519, 2016.

[111] G. Martín, J. M. Bioucas-Dias, and A. Plaza. Hyca: A new technique for hyperspectral compressive sensing. *IEEE Transactions on Geoscience and Remote Sensing*, 53(5):2819–2831, 2015.

[112] J. C. Emmanuel. The restricted isometry property and its implications for compressed sensing. *Comptes Rendus Mathematique*, 346(9):589 – 592, May 2008.

[113] S. Boyd and L. Vandenberghe. *Convex optimization*. Cambridge university press, 2004.

[114] H. C. Andrews. Digital image restoration: A survey. *Computer*, 7(5):36–45, May 1974.

[115] M. Bertero, T. A. Poggio, and V. Torre. Ill-posed problems in early vision. *Proceedings of the IEEE*, 76(8):869–889, August 1988.

[116] S. Qaisar, R. M. Bilal, W. Iqbal, M. Naureen, and S. Lee. Compressive sensing: From theory to applications, a survey. *Journal of Communications and networks*, 15(5):443–456, 2013.

[117] E. Candes, N. Braun, and M. Wakin. Sparse signal and image recovery from compressive samples. In *Biomedical Imaging: From Nano to Macro, 2007. ISBI 2007. 4th IEEE International Symposium on*, pages 976–979. IEEE, 2007.

[118] D. L. Donoho and X. Huo. Uncertainty principles and ideal atomic decomposition. *IEEE transactions on information theory*, 47(7):2845–2862, 2001.

[119] F. L. Santosa and W. W. Symes. Linear inversion of band-limited reflection seismograms. *SIAM Journal on Scientific and Statistical Computing*, 7(4):1307–1330, 1986.

[120] R. Baraniuk, M. Davenport, R. DeVore, and M. Wakin. A simple proof of the restricted isometry property for random matrices. *Constructive Approximation*, 28(3):253–263, 2008.

[121] J. A. Tropp and S. J. Wright. Computational methods for sparse solution of linear inverse problems. *Proceedings of the IEEE*, 98(6):948–958, apr 2010.

[122] R. G. Baraniuk. Compressive sensing [lecture notes]. *IEEE signal processing magazine*, 24(4):118–121, 2007.

[123] A. Y. Yang, S. S. Sastry, A. Ganesh, and Y. Ma. Fast l1-minimization algorithms and an application in robust face recognition: A review. In *Proc. IEEE Int. Conf. Image Processing*, pages 1849–1852, September 2010.

[124] M. AT Figueiredo, R. D. Nowak, and S. J. Wright. Gradient projection for sparse reconstruction: Application to compressed sensing and other inverse problems. *IEEE Journal of selected topics in signal processing*, 1(4):586–597, Dec 2007.

[125] S. Mallat. *A wavelet tour of signal processing*. Elsevier, 1999.

[126] J. Bioucas-Dias and M. AT Figueiredo. A new twist: two-step iterative shrinkage/thresholding algorithms for image restoration. *IEEE Transactions on Image processing*, 16(12):2992–3004, Dec 2007.

[127] A. Chambolle. An algorithm for total variation minimization and applications. *Journal of Mathematical imaging and vision*, 20(1-2):89–97, Jan 2004.

[128] Lambda Research Corp., Littleton, MA. *OSLO Optics Software for Layout and Optimization Optics Reference*, June 2001.

[129] Lambda Research Corp., Littleton, MA. *OLSO Optics Software for Layout and Optimization Program Reference*, January 2016.

[130] E. Hecht. *Optics*. Pearson Education, 2016.

[131] J. S. Accetta *et al. The infrared and electro-optical systems handbook*, volume 2. Infrared Information Analysis Center, 1993.

[132] J. Tesar and R. L. Thompson. Lens assembly and optical imaging using same, may 2006.

[133] A. L. Cavalieri *et al.* Intense 1.5-cycle near infrared laser waveforms and their use for the generation of ultra-broadband soft-x-ray harmonic continua. *New Journal of Physics*, 9(7):242, July 2007.